POLITECNICO DI MILANO

Facoltà di Ingegneria dei Processi Industriali

Dipartimento di Energia

Dipartimento di Chimica, Materiali e Ingegneria Chimica "Giulio Natta"

COMPUTATIONAL FLUID DYNAMICS OF GAS-SOLID CATALYTIC REACTORS BASED ON MICROKINETIC DESCRIPTION OF SURFACE CHEMISTRY

Relatori: **Prof. Alberto CUOCI**
Prof. Matteo MAESTRI

Tesi di Laurea in Ingegneria Chimica di:

Sandro GOISIS Matr. 749999

Alessandra OSIO Matr. 750676

Anno Accademico 2010–2011

Abstract

A deep understanding of the entire reacting process is a prerequisite for the development and optimization of industrial catalytic technologies. In this sense, the identification of the *dominant reaction mechanism* is crucial for a full comprehension of catalytic processes. The dominant reaction pathway is the sequence of reaction steps that establishes under specific operating conditions. This results from the interplay among phenomena occurring at different spatial and temporal scales. Thus, the dominant reaction mechanism is a multi-scale property of the system.

In this work we develop a numerical tool (catalyticFOAM) able to investigate catalytic systems with a first-principles approach, i.e. the governing equations are employed to describe each scale. This allows to study the actual behaviour of the system by coupling computational fluid dynamics (CFD) methodologies with a detailed microkinetic description of surface chemistry. Given the complexity of the numerical problem, an operator splitting technique is adopted. Specifically, the reacting and transport terms are computed separately.

The catalyticFOAM solver allows for the dynamic solution of reacting flows over solid catalysts. The surface reactivity is described by detailed kinetic schemes with no theoretical limits to the number of species or reactions involved. Specifically, CHEMKIN and UBI-QEP format, along with classical rate-equations, can be implement.

The flow field is described by the Navier-Stokes equations, both in laminar and turbulent conditions. The solution of the energy equation allows to simulate the system both in isothermal and adiabatic conditions. The possibility to investigate systems with geometries of arbitrary complexity confers generality and flexibility to the solver.

In order to investigate the reliability of the catalyticFOAM, a validation has been performed. The fuel-rich H_2 combustion over Rh catalyst has been analyzed and the simulation results have been compared with experimental data. Two hypothesis about the imperfect fitting of measured data have been formulated and validated. Furthermore, a study of the transient behaviour of the reactor has been conducted.

Abstract

Una profonda conoscenza dell'intero processo reattivo è di fondamentale importanza per lo sviluppo e l'ottimizzazione delle tecnologie catalitiche industriali. In questo senso, l'identificazione del *meccanismo dominante di reazione* è cruciale per una piena comprensione dei processi catalitici. Il cammino dominate di reazione è la sequenza delle reazioni elementari che si instaurano sotto determinate condizioni operative ed è il risultato delle interazioni tra i vari fenomeni che avvengono alle diverse scale temporali e spaziali. Perciò il meccanismo dominante di reazione è una proprietà multi-scala del sistema.

In questo lavoro di tesi è stato sviluppato uno strumento di calcolo (catalyticFOAM) capace di predire il comportamento di sistemi catalitici mediante un approccio ai principi primi. Questo significa che la descrizione del sistema è realizzata impiegandole equazioni regolatrici dei fenomeni a ciascuna scala. L'utilizzo di un simile approccio consente di studiare il comportamento effettivo del reattore accoppiando le metodologie seguite dalla fluidodinamica computazionale (CFD) con la descrizione dettagliata della cinetica di reazione superficiale. Data la complessità del problema è stata adottata una tecnica di splitting-operator per rendere possibile la risoluzione delle equazioni: ciò significa che il termine reattivo e quello di trasporto vengono calcolati separatamente.

Il solutore catalyticFOAM permette di descrivere la dinamica dei flussi reattivi su catalizzatori solidi. La reattività della superficie catalitica è descritta da schemi cinetici dettagliati:lo strumento è organizzato in modo che non vi sia un limite teorico al numero di specie o di reazioni coinvolte. Inoltre possono essere implementati schemi cinetici UBI-QEP oltre a meccanismi classici in formato CHEMKIN.

Il campo di moto è descritto dalle equazioni di Navier-Stokes, sia in condizioni laminari che turbolente. La soluzione dell'equazione dell'energia permette di simulare sistemi sia

in condizioni isotermiche che adiabatiche. Inoltre la possibilità di studiare sistemi aventi geometrie di arbitraria complessità conferisce generalità e flessibilità al solutore.

Una convalida su catalyticFOAM è stata condotta al fine di studiarne l’affidabilità. E’ stata analizzata la combustione su rodio di una corrente ricca in idrogeno e i risultati sono stati confrontati con i dati sperimentali. Per giustificare il disaccordo dei dati sperimentali con quelli simulati è stata formulata e convalidata un’ipotesi. Infine è stato condotto uno studio del comportamento del reattore durante il transitorio.

Summary

List of Figures

Chapter 1.

Introduction and main results

1.1. General overview

Catalyst based technologies are widely used in chemical and fuel industry. In order to develop industrial processes with more active and more selective catalysts, a deep understanding of the entire reacting process is required. In this sense, the identification of the *dominant reaction mechanism* is crucial for a full comprehension of catalytic processes at the molecular scale.

Essentially, the dominant reaction pathway consists of the set of the most significant chemical pathways by which the reactants convert to the products under specific operating conditions. The dominant reaction mechanism turns out from the interaction among the whole set of potential chemical events acting at the micro-scale at specific conditions of temperature, pressure and composition.

Therefore, the selection of preferential reaction pathways is the result of the interplay among microkinetic events and macro-scale phenomena. Indeed variables at the molecular scale are determined by transport phenomena of mass, energy and momentum, taking place at the reactor scale.

Since the dominant reaction pathway is the result of the interplay between micro-, meso- and macro-scale phenomena, different time and length scales are involved (Figure 1.1).

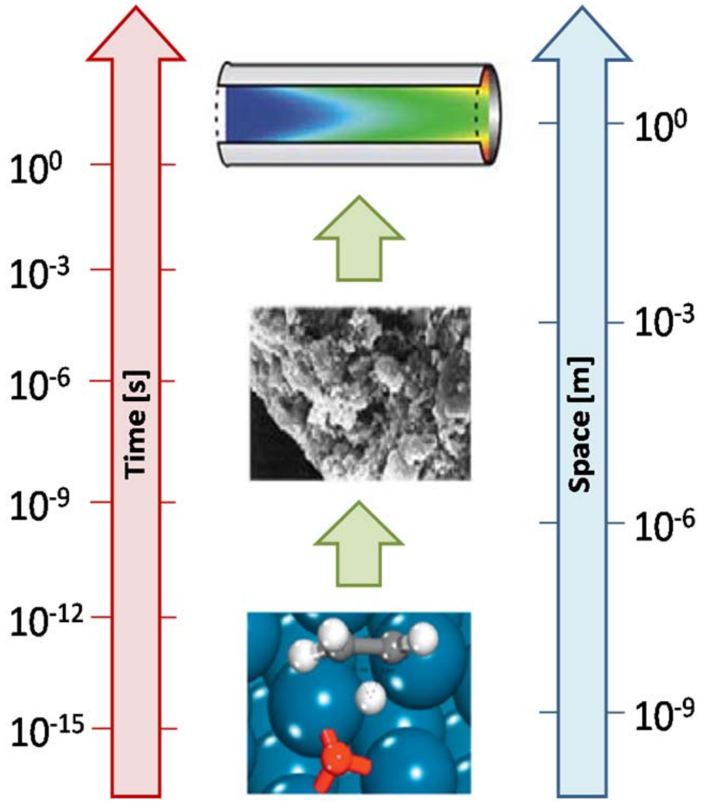

Figure 1.1 Time and length scales involved in heterogeneous catalytic processes.

The microscopic scale is associated with making and breaking of chemical bonds between atoms and molecules. At the mesoscopic scale the interplay between all the elementary steps involved in the catalytic process determines the main reaction pathway. At the macroscopic scale transport of mass, energy and momentum determines local composition, temperature and pressure.

This means that the dominant reaction mechanism is a multi-scale property of the system (Maestri 2011). The description of different phenomena is achieved by employing a first principles approach, i.e. at each scale the fundamental governing equations are used.

- ✓ At the molecular scale the behaviour of the system is described through detailed kinetic models, whose parameters are computed via first-principles electronic-structure calculations.
- ✓ At the meso-scale statistical methods give a rigorous representation of mechanisms taking place at the catalytic surface. Anyway the most common approach used in literature is the mean field approximation(Vlachos, Stamatakis et

al. 2011). This approach assumes a perfect and rapid mixing of reactants, products and intermediates on the surface.

- ✓ At the macro-scale methods based on continuum approximation are employed, e.g. resolution of Navier-Stokes equations with Computational Fluid Dynamics (CFD) methodologies (Reuter 2009).

Such a fundamental approach implies the development of efficient methodologies to connect the fundamental aspects across all the scales involved and link them in one multi-scale simulation.

Unluckily, the resulting numerical problem places highly computational demands mainly related to:

- ✓ The dimensions of the system are proportional to the number of species involved in the reacting process. Therefore, the more detailed the kinetic scheme is, the higher the required time is.
- ✓ The discretization of the geometric domain is required to solve the problem. The number of cells in which the volume is divided is proportional to the accuracy and to the dimensions of the problem.
- ✓ The problem is very stiff because of the difference among the characteristic time of the scales.
- ✓ The presence of a reacting term implies a strong non-linearity of the governing equations.

In the following, a summary on the most interesting approaches to this problems available in literature is provided.

1.2. State of Art

The development of tools capable to describe the actual behaviour of catalytic systems via first principles and multi-scale approaches is still in the initial phase. This is due to the complexity of the numerical problem that one has to handle. Recent advances in this field are owed to the vast diffusion of CFD applications.

Nowadays CFD is able to predict very complex flow fields due to the recent development of numerical algorithms and the availability of more performing computer hardware. However CFD methodologies still lack in efficient handling of detailed kinetic schemes, mainly due to the difficult management of the huge number of reactions and species involved and to the stiffness of the problem.

Recently the attention has been focused on the development of tools that implement heterogeneous kinetic models. In this section the most recent and challenging studies on coupling of microkinetic modeling and CFD are provided.

The most noticeable advances in this framework have been provided by (Deutschmann, Tischer et al. 2008) with the development of the DETCHEM^{TM} software. This is a FORTRAN based package designed to couple detailed chemistry models and CFD. The software package contains tools able to simulate time dependent variations of gas-phase systems as a result of homogeneous gas-phase and/or heterogeneous surface chemical reactions. The list of tools contained in the DETCHEM library is presented above, specifying mathematical aspects and range of applicability (Deutschmann, Tischer et al. 2011).

- ✓ DETCHEM^{BATCH} and DETCHEM^{CSTR} are computational tools that simulate homogeneous and heterogeneous reactions taking place respectively in a batch and CSTR reactor. These tools adopt maximum gradient mono-dimensional model and does not solve the Navier-Stokes equations. The reactors can be simulated under both isenthalpic and adiabatic conditions. The DETCHEM^{BATCH} can perform sensitivity analysis in order to refine the kinetic mechanism.
- ✓ DETCHEM^{PLUG} is an application able to simulate the behaviour of plug flow chemical reactors for gas mixture. The model is mono-dimensional and it have been developed in the assumption of negligible axial diffusion and absence of variations in transverse direction.
- ✓ DETCHEM^{PACKEDBED} is a tool for the simulations of packed bed reactors. The model is one-dimensional heterogeneous and assumes that there is no axial diffusion and no radial variations in the flow properties. The governing equations used are the same of the DETCHEM^{PLUG}, apart from the use of experimental correlations for the computation of heat and mass transfer coefficient.

- ✓ DETCHEM^{CHANNEL} is a computational tool that simulate the steady state chemically reacting gas flow through cylindrical channels using the boundary-layer approximation. This states that, for systems with a main direction of the convective flow, the diffusive transport along this direction can be neglected. Indeed, at high flow rates in a channel, radial diffusion and convective transport prevail over axial diffusion. Thus, all the second derivatives in the flow direction can be eliminated. Furthermore, pressure gradients in axial direction also vanish. The original system of elliptical differential equations is reduced to a parabolic one. This hypothesis becomes valid when the Reynolds number is sufficiently high(Bird 2002).
- ✓ DETCHEM^{MONOLITH} is a simulation code that is designed to simulate transient problems of monolithic reactors, used whenever the interactions of chemistry, transport and reactor properties shall be investigated in monolithic structures of straight channels. Monolithic reactors consist of a large number of parallel channels: the behaviour of the representative channels are described by DETCHEM^{CHANNEL} or DETCHEM^{PLUG}. The monolith temperature is computed by using a two or three dimensional model. It is assumed that there is no gas exchange between the channels and that the residence time of the gas inside the channels is small compared with the response time scale of the monolith. Furthermore, it is assumed that the cross-section of the monolith does not change along the channel axis.
- ✓ DETCHEM^{RESERVOIR} is an application that allows to simulate isothermal transient behaviour of monolith reactors. Only selected surface concentrations are assumed to vary over time, and are called storage concentrations. The approach used consists in iterating steady-state and transient calculations. For each time step the DETCHEM^{CHANNEL} or DETCHEM^{PLUG} routines are called. The obtained steady-state values are then used by DETCHEM^{RESERVOIR} as initial values in the integrations of site conservation balances of storage species. The main constraint that limits the validity of this splitting method is that the time scale for surface storage reactions must be larger than the residence time of the gases inside the channel.

- ✓ DC4FLUENT is a collection of user defined functions and works by coupling the DETCHEM routine with the commercial CFD code FLUENT. Furthermore the routines of the DETCHEM library are used to calculate source terms for the governing equations of mass, species and energy by the DC4FLUENT plugin.

The studies that have been developed by using this software package are presented in the following.

In (Deutschmann, Correa et al. 2003) the start-up of the catalytic partial oxidation (CPO) of methane over rhodium/alumina in a short contact times reactor was investigated. The study was conducted by employing the DETCHEM^{MONOLITH} code. The triangular shape of the single channel of the monolith was approximated with a cylindrical structure. Five representative channels were simulated in order to describe the behaviour of the monolith. The kinetic scheme adopted comprehends both gas-phase and surface reaction mechanism.

A study on the abatement of automotive exhaust gases on platinum catalysts was performed by (Koop and Deutschmann 2009), by using the DETCHEM^{CHANNEL} application. The two-dimensional flow-field have been described and a detailed reaction mechanism for the conversion of CO, CH_4, C_3H_6, H_2, O_2 and NO_x has been included. Based upon experiments with a platinum catalyst in an isothermal flat bed reactor, a detailed surface reaction mechanism has been developed. Numerical simulations of the thermodynamic equilibrium of nitrogen oxides and calculations of surface coverage on platinum have been performed.

Mladenov and co-workers performed a CFD study in order to understand the impact of the real washcoat shape on the overall reaction rate. The computational tools used from the DETCHEM package are DETCHEM^{CHANNEL} and DC4FLUENT plugin. The aim of the work was to study mass transfer in single channels of a honeycomb-type automotive catalytic converter operated under direct oxidation conditions. Specifically, 1D, 2D and 3D simulations were performed on channels of different shapes, respectively circular cross section, square cross section and square cross section with rounded corners. Furthermore, the effect of diffusion in porous washcoat was investigated. The reaction mechanism comprehends 74 reactions among 11 gas-phase and 22 adsorbed surface species(Mladenov 2010).

The catalytic partial oxidation of the gasoline surrogate iso-octane over a Rh coated monolith was investigated by Hartmann and co-workers, using the DETCHEM$^{\text{CHANNEL}}$ tool. The final kinetic mechanism consists of 7193 homogeneous and 58 heterogeneous reactions among 857 gas phase and 17 surface species (Hartmann, Maier et al. 2010).

Besides these work developed with the DETCHEM library, another interesting study have been realized by Vlachos and co-workers. They performed a study on catalytic combustion of propane on platinum in micro-reactors under laminar conditions. A comprehensive parametric analysis was made investigating the role of inlet velocity, equivalence ratio and reactor size. A two-dimensional model was used. The kinetic model adopted consisted of a one-step reaction mechanism, obtained via a-posteriori model reduction of detailed microkinetic mechanism (Vlachos, Kaisare et al. 2008).

As seen in this section all the works presented contain a variety of approximations concerning with governing equations, kinetic mechanisms and specific geometries. Instead, our work provides a tool able to simulate the actual physic of the system without introducing any restrictive approximation. The flow field can be trustfully predicted either for laminar or turbulent conditions. Moreover, it can take into account detailed kinetic mechanisms without any constraint on the number of species and reactions involved. A better description of the microkinetic mechanism can be achieved by the use of UBI-QEP schemes. Finally, the shape of the geometric domain is not subjected to any limitations. Any three-dimensional domain can be investigated. If the system has specific symmetry properties, it can be studied with a 2D simulation. This allows to save a huge amount of time.

The methodologies followed in our work to accomplish these objectives are explained in the next paragraph.

1.3. Methodologies and main results

The tool developed in this work, named catalyticFOAM, was built up in the OpenFOAM® framework, an open source CFD code.

The available CFD tools that solve this class of heterogeneous reacting problems have large difficulties in handling multi-scale coupling efficiently. On one side fully coupled methods are suitable only for problems of small dimensions. On the other side segregated methods are inappropriate for the solution of stiff and non-linear problems. To overcome these difficulties we propose a new approach based on the splitting operator method. This allows to split the problem in two sub-problems and to solve them decoupled. In Figure 1.2 a schematization of the splitting operator method is presented.

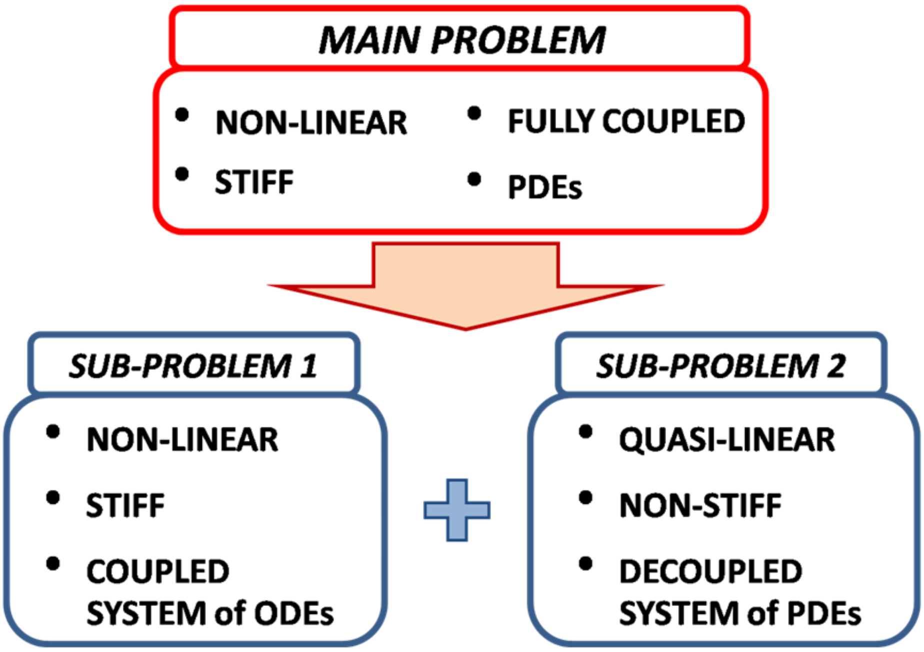

Figure 1.2. Schematization of the splitting operator method.

This implies the following advantages:

- ✓ Opportunity to select the best numerical algorithm for each sub-problem.
- ✓ Stiffness and non-linearity are enclosed in one sub-problem.
- ✓ Low stiffness and quasi-linearity permit to adopt a fully segregated approach.

Consequently the problem can be efficiently solved (Strang 1968; Pope and Zhuyin 2008).

The application of the Strang splitting scheme to our problem has been achieved by separating the portions of the governing equations containing chemical reaction terms from those containing the transport terms. The latter are solved in sequence, each one decoupled from the others, as prescribed by the segregated approach. Instead of having a huge system of PDEs, one has to solve each equation of the system decoupled. A special attention has to be paid to the Navier-Stokes equations. Indeed, the strong coupling with the continuity equation makes it necessary to treat the inter-equation coupling in an explicit manner. The procedure followed is the Pressure Implicit Splitting Operator (PISO) method. PISO and their derivatives are the most popular methods for dealing with inter-equation coupling in the pressure-velocity system for transient solutions (Jasak 1996)**.** Further details on the development of the tool are provided in Chapter 2.

The microkinetic description is provided by the CatalyticSMOKE libraries. These adopt standard CHEMKIN correlations and can handle both classical and UBI kinetic schemes. The detailed structure and functioning are provided in Chapter 3.

The application of these methodologies led to the development of the catalyticFOAM solver. The work was mainly focused on the implementation of the code. This was made by adding one feature at a time and validating it before proceeding. The main features of our tool are:

- ✓ The possibility to solve both homogeneous and heterogeneous reacting flows.
- ✓ The ability to perform simulations with an accurate description of the velocity field by the resolution of the Navier-Stokes equations in both laminar or turbulent conditions, with any arbitrary geometric domain.
- ✓ The possibility to describe the reaction mechanisms with detailed kinetic models.
- ✓ The capability to simulate a wide variety of operating conditions, e.g. isothermal or adiabatic conditions.

The performance of catalyticFOAM is tested with a series of convergence tests, reported in Chapter 4. In particular, an analysis of the discretization of space and time domains is required. The number of cells in which the geometric domain is divided is crucial for the achievement of convergence. The study comprehends sensitivity analysis for the number of units employed to describe the system in the directions perpendicular and parallel to the catalyst, both in chemical and diffusive regime. The main results are listed below.

- ✓ The discretization of the coordinate parallel to the catalyst strongly affects the final solution.
- ✓ The number of cells in which the coordinate perpendicular to the catalyst surface is divided has a low impact on the solution.

- ✓ The convergence is achieved by adopting a small number of cells for systems under chemical regime.
- ✓ For systems dominated by mass-transfer phenomena, the convergence is achieved only with a well refined discretization of spatial domain. This behaviour is due to the presence of gradients with high magnitude. Their description is crucial to the achievement of convergence.
- ✓ The width of the temporal step of integration depends on the type of system considered and in particular is related to the velocity field and the reactivity of the catalyst.
- ✓ The computational times increase with the rising of the reactivity of the system and in particular with the augment of magnitude of composition and temperature gradients.

In order to investigate the reliability of the catalyticFOAM, a validation has been performed in Chapter 5. The fuel-rich H_2 combustion over Rh catalyst in an annular reactor has been analyzed and the simulation results have been compared with experimental data. Specifically, the oxygen conversion achieved in the reactor at different temperatures has been computed with isothermal simulations. The results show a discrepancy between experimental and computed data in the high temperature range.

The hypothesis about the imperfect fitting of experimental data assumes that a catalyst evaporation and redeposition of Rh occurs upstream and downstream the main bed. The performed simulations show the validity of this assumption.

In order to provide a further analysis of the experimental apparatus the possible imperfect eccentricity of the annulus has been taken into account.

Finally, a study of the transient behaviour of the reactor has been conducted. The radial and axial gradients of composition have been reported in order to fully describe the analyzed study.

Chapter 2.

The catalyticFOAM solver

In this chapter, we present the main features of the solver developed in this work. First a general overview of the OpenFOAM® framework is provided. Then the catalyticFOAM solver is presented. The mathematical model and the numerical challenges are discussed.

2.1. General overview

OpenFOAM® (Open Field Operation And Manipulation) is an open source C++ library developed for finite volumes calculation applications. It was created in 1993 and it is increasing its popularity in the last years. The main reason for this wide success is that OpenFOAM® is released under General Public License (GPL), including the possibility to have at disposal the whole code and eventually modify it as needed. In August 2011 the OpenCFD Ltd. by SGI(OpenFOAM® 2011).

The aim of this section is to introduce the main features of OpenFOAM® as support code for CFD simulations and its practical use.

OpenFOAM® is a C++ library and it is an object-oriented numerical simulation toolkit for continuum mechanics. For this reason it is capable to support all the typical features of C++ programming, e.g. creation of new types of data specific for the problem to be solved, construction of data and operations into hierarchical classes, handling of a natural syntax for user defined classes (i.e. operator overloading) and it easily permits the code re-use for equivalent operations on different types (Mangani 2008).

OpenFOAM® is not meant to be a ready-to-use software, even if it can be used as a standard simulation package. Rather, it offers a support in building user specific codes. As the widest part of CFD software, OpenFOAM® provides tools not only for the finite volumes calculations, but also for pre and post processing. A schematic of the library structure is given in Figure 2.1.

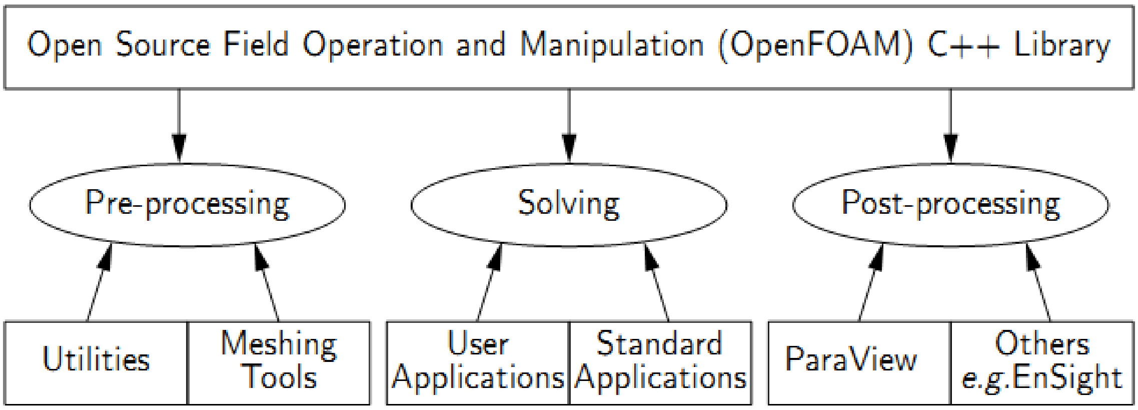

Figure 2.1. OpenFOAM® library structure.

Pre-processing tools enable the set-up of the simulations by the generation of the computational mesh, only with the corresponding initial and boundary conditions. Post-processing utilities allow one to view and analyze simulations results. The computational part is based on solvers, applications designed to solve specific classes of engineering problems, e.g. aerospace, mechanics, chemistry.

The latest OpenFOAM® version (2.0.1) includes over 80 solver applications and over 170 utility applications that perform pre- and post-processing tasks, e.g. meshing, data visualization, etc.

In the following we present the structure and organization of an OpenFOAM® case. In general the sequence of work in OpenFOAM® can be divided into three consecutive steps:

- *pre-processing*: firstly one has to set-up the problem;
- *processing*: the simulation is performed by a solver;

- *post-processing*: results are displayed with specific application for data analysis and manipulation.

2.1.1. Pre-processing

The basic directory structure for the set-up of an OpenFOAM®case is represented in Figure2.2.

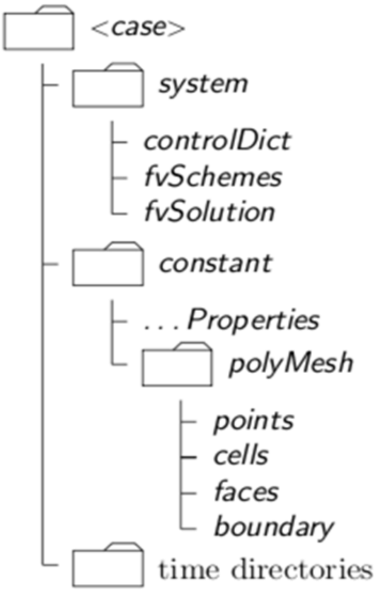

Figure 2.2. Directory structure for the set-up of an OpenFOAM® case.

The case folder includes:

- The “*polyMesh”* folder providing a full description of the case mesh.
- The “*constant”* directory that includes the files with physical properties.
- The “*time”* directories containing individual data files for each field (e.g. temperature, pressure, compositions) at different times of simulation.
- The “*system”* directory for setting numerical parameters associated with the solution procedure.

It is necessary to pay great attention to the creation of the computational mesh in order to ensure a valid and accurate solution. OpenFOAM® provides a mesh generation utility called *blockMesh* that creates parametric meshes with specified grading and arbitrary curved edges. The mesh is generated from a dictionary file named *blockMeshDict* located in the *constant/polyMesh* directory. The utility reads this dictionary, generates the mesh and creates the mesh data.

In order to generate a mesh in a simpler way it is possible to use a variety of software, such as *GAMBIT* (Fluent 2004), a mesh generation software owned by Ansys FLUENT that writes mesh data to a single file. OpenFOAM®provides a tool for the conversion of GAMBIT meshes to OpenFOAM® format.

Initial and boundary conditions for a certain number of fields are required in order to start the simulation. These data are stored in the t_0 folder: each file contains the initial condition for the internal field and the declaration of each boundary condition. The latter has to be chosen from a list of pre-built standard conditions (OpenFOAM® 2011).

The *system* directory contains at least the following three files: *controlDict, fvSchemes* and *fvSolution*. In the first one run control parameters are set, including start/end time, time step and other specifications. The *fvSchemes* file contains the discretization schemes used in the solution. Typically one has to assign the discretization methods for gradient, divergence etc. In the *fvSolution* file algorithms for the solution of each equations are selected and tolerances for each variables are set.

2.1.2. Processing and post-processing

During the calculation the solver iterates the numerical procedure and periodically writes results at intermediate times.

OpenFOAM® is supplied with the post-processing utility ParaView, an open source multi-platform data analysis and visualization application which provides a lot of useful tools for these scopes.

2.2. The math behind OpenFOAM®

The widest part of complex engineering systems is described by one or more Partial Differential Equations (PDEs). Since the majority of these equations does not have an analytical solution, it is necessary to solve them with numerical methods (Quarteroni and Valli 1999).

In this paragraph the fundamentals of numerical procedures of discretization and solution are presented.

2.2.1. Discretization algorithm

The purpose of any discretization practice is to transform one or more PDEs into the resulting system of algebraic equations to allow the numerical solution. The discretization process consists of splitting of the computational domain into a finite number of discrete regions, called control volumes or cells. For transient simulations, it is also required to divide the time domain into a finite number of time-steps. Finally, it is necessary to re-write equations in a suitable discretized form.

The approach of discretization adopted by OpenFOAM® is the Finite Volume Method (FVM) (Versteeg and Malalalsekera 1995).The main features of this method are listed below:

- The governing equations are discretized in the integral form.
- Equations are solved in a fixed Cartesian coordinate system on the computational mesh. Solution can be evaluated both for steady-state and transient behaviors.
- The control volumes can have a generic polyhedral shape: together they form an un-structured mesh (Patankar and Spalding 1972; Van Doormaal and Raithby 1985).

In the following we provide a description of discretization of domain, time and equations.

2.2.1.1. Domain discretization

The discretization via FVM entails the subdivision of the domain in control volumes or cells. These have to completely fill the domain without overlapping. The point in which variables are calculated is located in the centroid of the control volume of each cell, defined as:

$$\int_{V_P} (\boldsymbol{x} - \boldsymbol{x_P})dV = \boldsymbol{0} \tag{2.1}$$

where $\boldsymbol{x_P}$ stands for the coordinate of the centroid, as shown in Figure 2.3.

The domain faces can thus be divided in two classes: internal faces, between two control volumes, and boundary faces, which coincide with the boundaries of the domain. A simple example of domain discretization is showed in Figure 2.3.

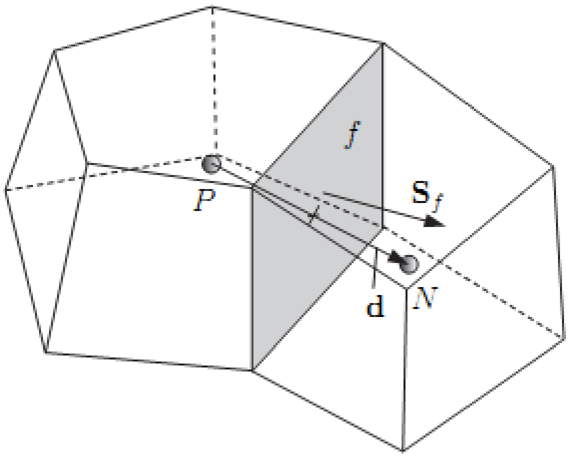

Figure 2.3. Example of finite volume discretization.

In Figure 2.3 the point *P* and *N* represents the centroid of the cells of the geometric domain. The vector *d* represents the distance between the two centroids. The vector S_f is the surface vector outgoing from the generic flat face *f*.

2.2.1.2. Equations discretization

Let us consider the standard form of the transport equation of a generic scalar field ϕ:

$$\frac{\partial \rho \phi}{\partial t} + \nabla \cdot (\rho \boldsymbol{U} \phi) - \nabla \cdot (\Gamma \nabla \phi) = 0 \tag{2.2}$$

where $\boldsymbol{U}$ is the velocity vector and Γ is the generic diffusion coefficient (e.g. thermal conductivity). For the sake of clarity the source term has been neglected. Further details on the discretization of the source term can be found in section 2.3.3.

The finite volume method requires that Eq. (2.2) is satisfied over the control volume V_P in the integral form:

$$\int_t^{t+\Delta t} \left[\frac{\partial}{\partial t} \int_{V_P} \rho \phi dV + \int_{V_P} \nabla \cdot (\rho \boldsymbol{U} \phi) dV - \int_{V_P} \nabla \cdot (\rho \Gamma \nabla \phi) dV \right] dt = 0 \tag{2.3}$$

The discretization of each term of Eq. (2.3) is achieved by applying the Gauss theorem in its general form:

$$\int_V \nabla\phi dV = \oint_{\partial V} \phi dS \tag{2.4}$$

Having in mind that each cell is bounded by a list of flat faces, it is possible to re-write the integral of Eq. (2.4) as a sum over all faces. The combination of Eq. (2.3) and (2.4) leads to:

$$(\nabla\phi)V_P = \sum_f S_f\phi_f \tag{2.5}$$

where V_P is the volume of the cell, S_f is the surface of the cell and ϕ_f is the flux of the generic scalar ϕ through the face f.

2.2.1.3. Time discretization

In transient problems it is fundamental to adopt numerical methods to handle temporal integration. Let us consider the first term of Eq. (2.3):

$$\int_t^{t+\Delta t}\left[\frac{\partial}{\partial t}\int_V \rho\phi dV + \int_V \Psi(\phi)dV\right]dt \tag{2.6}$$

where $\Psi(\phi)$ is a generic non linear function.

The time integration can be evaluated in three different ways in OpenFOAM®:

- **Euler implicit:** the time term is discretized in an implicit way (Buzzi-Ferraris 1998), thereby taking current values ϕ^n:

  $$\int_t^{t+\Delta t}\Psi(\phi)dt \cong \Psi_D(\phi^n)\Delta t \tag{2.7}$$

  where $\Psi_D(\phi^n)$ is the discretized form of the spatial quantity $\Psi(\phi)$ and n indicates the new computed value. This method provides first order accuracy, guarantees boundedness and is always stable (Jasak 1996).

- **Explicit:** the spatial term is discretized in explicit way, which means that old values of ϕ are used:

  $$\int_t^{t+\Delta t}\Psi_D(\phi^n)\, dt \cong \Psi_D(\phi^o)\Delta t \tag{2.8}$$

  where $\phi^o$are the old values of ϕ. This method is first order accurate and the solution depends only on previous times. The main disadvantage is that this method becomes unstable when the Courant number is larger than unity. Further details on the Courant number are provided in section 4.3.

- **Crank-Nicholson:** a trapezoid rule is used to discretize the temporal integral:

$$\int_{t}^{t+\Delta t} \Psi_D(\phi)\, dt \cong \Psi_D\left(\frac{\phi^n + \phi^o}{2}\right)\Delta t \tag{2.9}$$

  This method is second order accurate and stable, but does not guarantee boundedness of the solution (Ferziger and Peric 1999).

In the rest of this dissertation the Euler implicit method has been adopted.

2.2.1.4. Boundary conditions

In order to complete the formulation of the discretized problem one has to set boundary conditions. First of all, it is important to separate physical and numerical conditions:

- **Physical conditions:** these conditions are derived from engineering interpretation of the true system behavior. These conditions are set during the creation of a mesh. Each physical condition is the union of several numerical conditions. Here we provide some significant examples:
  - ✓ Inlet: the velocity profile at inlet is assigned and, for consistency, pressure gradient is set to zero.
  - ✓ Outlet: the pressure profile is assigned and velocity gradient is set to zero.
  - ✓ Symmetry plane: in bidimensional cases it is necessary to specify the symmetry plane of the system. The related boundary condition implies that the components of the gradient normal to the surface are set to zero.
- **Numerical conditions:** these conditions provide a suitable expression for the value of variables at boundaries. Their values are specified with the initial conditions. Specifically, the most important conditions are Dirichlet (or fixed value) and Neumann (or fixed gradient).

2.2.2. Algebraic linear systems

OpenFOAM® implements different algorithms for the solution of linear algebraic systems of equations. Algorithms are selected by specifying the following features:

- *Preconditioner*: allow one to choose a method for the preconditioning of the system. More details on this methods are given in (OpenFOAM® 2011). This improves the conditioning of the problem and save computational time.
- *Linear solver*: specifies which solver has to be used. Here we cite Krylov subspace solvers and GAMG (OpenFOAM® 2011), which evaluate the solution on a coarse grid and then refine it on a finer mesh.
- *Smoothers*: improve computational speed reducing the number of iterations required to reach the convergence.

2.3. The catalyticFOAM solver

In this section the attention is focused on the development of the new solver, focusing on mathematical and numerical aspects. First the mathematical description of the problem is given.

To define the mathematic approach to the problem it is compulsory to elucidate physical and chemical aspects of the catalytic process. Let us consider a simple cylindrical plug flow reactor with outer wall covered by catalyst. The incoming gas flows through the pipe in laminar or turbulent regime, influencing pressure and density. Meanwhile the species diffuse and react in the homogeneous phase. Moreover, on the catalytic surface reactants and products continuously adsorb and desorb at the gas-surface and adsorbed species react at the catalytic surface.

As a consequence, the variables needed to be solved for a full characterization of the system are:

- ✓ Velocity
- ✓ Pressure
- ✓ Density

- ✓ Temperature
- ✓ Gas species concentrations
- ✓ Adsorbed species concentrations

All these variables are in principle a function of spatial coordinates and time.

In the following section we point out the mathematical model used to describe the behaviour of the system.

2.3.1. Mathematical model

For a correct description of the flow field it is necessary to solve the Navier-Stokes equations for the momentum transport under the hypothesis of Newtonian fluids:

$$\frac{\partial(\rho\boldsymbol{U})}{\partial t} + \nabla\cdot(\rho\boldsymbol{U}\boldsymbol{U}) = -\nabla P + \nabla\cdot(\mu\nabla\cdot\boldsymbol{U}) + \rho\boldsymbol{g} \tag{2.10}$$

where μ is the dynamic viscosity, $\boldsymbol{g}$ is the gravity acceleration and P is the pressure.

Since the density field depends on pressure and velocity variations, it is necessary to add the continuity equation:

$$\frac{\partial\rho}{\partial t} - \nabla\cdot(\rho\boldsymbol{U}) = 0 \tag{2.11}$$

For compressible flows it is requested the knowledge of the pressure field, described by the equation of state. Since the technological interest is focused on processes where the flowing phase is gaseous, the ideal gas approximation is adopted:

$$PV = nRT \tag{2.12}$$

As we want to consider multicomponent mixtures, we solve the transport equation of species under the hypothesis of Fickian diffusion, as follows:

$$\frac{d(\rho\omega_i)}{dt} + \nabla\cdot(\rho\boldsymbol{U}\omega_{\boldsymbol{i}}) - \nabla\cdot(\rho\mathcal{D}_{\mathrm{i}}\nabla\omega_{\mathrm{i}}) = \sum \mathrm{R_j}\nu_{ij}\,\mathrm{MW_i} \tag{2.13}$$

where ω_i is the mass fraction of the *i*th component, $\mathcal{D}_{\mathrm{i}}$ represents the diffusivity of the *i*th species in the reacting mixture andν_{ij} is the stoichiometric coefficient of the *i*th species in the *j*th reaction. $\mathrm{R_j}$ is the rate of the *j*th reaction and includes both homogeneous and heterogeneous reactions.

In order to describe the temperature field, the solution of the energy balance is required.

$$c_p \frac{\partial(\rho T)}{\partial t} + c_p \nabla \cdot (\rho \boldsymbol{U} T) - \lambda \nabla^2 T = \sum \mathrm{R_j} \Delta \mathrm{H_j} \tag{2.14}$$

where$T$ is the temperature, c_p is the specific heat of the gas mixture and $\Delta \mathrm{H_j}$ is the heat of reaction of the *j*th reaction. The energy dissipation due to the viscosity of the fluid is neglected. Furthermore the pressure term can be ignored (Bird 2002). The specific heat of the mixture is assumed not to vary during the integration of the single time step.

In order to take into account the presence of the catalyst surface, it is necessary to define appropriate boundary conditions for both species mass-fractions and temperature. Indeed the reactants move from the gas phase to the surface and products travel in the opposite direction, creating a concentration gradient normal to the catalyst. These are written as follows, and their derivations are provided in Appendix A.

$$\rho \mathcal{D}_{\mathrm{i}} \frac{\partial \omega_i}{\partial r} = -\sum_{j=1}^{NR} R_j^{het} \nu_{ij} MW_i \, \alpha_{cat} \tag{2.15}$$

$$\lambda \frac{\partial T}{\partial r} = -\sum_{j=1}^{NR} R_j^{het} \Delta H_j \alpha_{cat} \tag{2.16}$$

where $r$is the coordinate normal to the catalytic surface, R_j^{het} is the heterogeneous surface reaction rate of the *j*th reaction and MW_i is the molecular weight of the *i*th species. Since the catalyst structure is highly complex and tortuous, its rigorous description is feasible only for geometries of dimensions comparable with those of pores.

Given the complexity of the catalyst surface, the face of the mesh adjacent to the catalytic layer is approximated with a flat surface. This allows for the use of less detailed meshes: the morphology of the catalyst is indeed neglected. In order to take into account the higher availability of surface sites of porous catalysts, it is necessary to introduce a new parameter (Maestri, Beretta et al. 2008). We define the α_{cat} constant as the ratio between geometric and effective catalytic area, as follows:

$$\alpha_{cat} = \frac{A_{cat}}{A_{react}} \tag{2.17}$$

where A_{cat} is defined as the real catalytic area measured with chemisorption analysis.

The mathematical derivation of this term is provided in Appendix A. This approximation make our tool suitable for a large variety of heterogeneous reacting systems, except those under internal diffusive regime.

Furthermore site conservation balances have to be written as follows:

$$\Gamma_{site}\frac{\partial \vartheta_i}{\partial t} = \sum_{j}^{NCF} R_{j,sur}\nu_{ij} \tag{2.18}$$

where ϑ_i is the site fraction of the *i*th species and Γ_{site} is the site fraction.

2.3.2. Numerical challenges

As largely anticipated in the first chapter, the aim of our work is to develop a powerful tool able to predict the behaviour of homogeneous and heterogeneous reacting system with special attention to the latter, taking into account detailed kinetic schemes.

Detailed kinetic schemes usually consist of hundreds of chemical species (molecular and radical species) and thousands of elementary direct and inverse reactions. Consequently, the direct coupling of a CFD code with detailed kinetic schemes is complex and disposes severe demands of computational resources.

For instance, it is quite simple to get an idea of the global dimensions of the numerical problem since they are proportional to the product between the number of computational cells (N_C), in which the system is discretized, and the number of chemical species (N_S), along with a few additional variables (e.g. temperature, pressure, and momentum).Consequently, it would be quite common to have some millions of variables describing the coupled CFD and kinetic problem(Manca, Buzzi-Ferraris et al. 2009).

Additionally, in a catalytic process extremely different time and length scales are involved. Elementary steps of reaction concern atoms and molecules at a length scale of 0,1 nm. The characteristic time for a single chemical event varies in the order of femto-seconds for a single dissociation and picoseconds for diffusion over a distance of 10 nm. Chemical species continuously adsorb and desorb on the catalytic surface with a characteristic time of microseconds. Variables at the molecular scale are influenced by transport phenomena of mass, energy and momentum taking place at the reactor scale.

The coupling among these scales is crucial in determining the real behaviour of the system (Maestri 2011). Consequently the resulting numerical problem can be very stiff. This means that, in order to solve the problem considering properly every phenomena at each scale, it would be necessary to adopt an integration step of magnitude smaller then the characteristic time of the fastest process.

Moreover, in case of reacting systems, strong non-linearities are present in the equations. The diffusion and convection terms are slightly non-linear, and therefore they can be easily lagged or linearized without large losses of accuracy in the solution (Jasak 1996). Nevertheless the source term due to the reaction is highly non-linear: in fact the widest part of kinetic constants are expressed in the Arrhenius form and the reaction rate is proportional to concentrations at the power of the respective reaction order. For this reason in order to solve the problem it is necessary to adopt specific algorithms.

Nowadays, available CFD codes encounter a large amount of difficulties in the solution of these problems, especially in case of the use of detailed microkinetic description of the surface chemistry. For all the reasons presented above, it is compulsory to rely on numerical techniques that permit to overtake these difficulties and obtain a satisfying and accurate solution.

2.3.3. Continuum equations of change

Since the fully coupled problem is too computationally demanding to be solved, it is necessary to adopt a segregated approach. This means that equations are solved one at a time with the inter-equation coupling eventually treated in the explicit manner. The computation is then achieved in much fewer amounts of time and the loss of accuracy has a small impact on the final solution. The application of this method to our problem is affected by two main issues.

- ✓ The first problem is owed to the presence of the pressure explicit term in the Navier-Stokes equations. Indeed, in order to solve the momentum equations, it is necessary to know the pressure field. Since we solve them decoupled, an explicit inter-equation coupling is required. In section 2.3.3.1, the PISO procedure proposed by (Issa 1986) is described. In transient calculations, all inter-equation couplings apart from the pressure-velocity system are lagged.

- ✓ The second problem is that the segregated approach can be adopted only in case of linear and non stiff problems. Anyway, in case of chemical reactions and especially with heterogeneous catalytic ones, it is necessary to introduce a source term in the species transport and temperature equations. Nevertheless the source term is highly non-linear and the system of equations becomes very stiff. In order to overtake these problems, it is convenient to use a splitting method (Ren and Pope 2008). In section 2.3.3.2 an overview of the Strang splitting scheme is given by following the description reported in (Pope and Zhuyin 2008).

2.3.3.1. Pressure-velocity coupling

The pressure-velocity coupling is taken into account by the PISO loop, a transient splitting method for the solution of the Navier-Stokes equations. Its algorithm is composed by three steps:

- ✓ Firstly, Navier-Stokes equations are solved assuming a constant pressure field. Its value is assigned at the previous step. This stage is called momentum predictor and an approximated value of the velocity field is obtained.
- ✓ Using predicted velocity it is possible to solve the continuity equation and consequently get the correct pressure field: this step is called pressure solution.
- ✓ The velocity field is corrected in an explicit manner making it consistent with the new pressure field. This is the explicit correction stage.

The PISO loop is iterated till the tolerance for the pressure-velocity system is reached: at this point one obtain the pressure and velocity fields for the current time step.

The correction of velocity actually consists of two parts: an adjustment due to the change in the pressure gradient and another one due to the variation of the neighbouring velocities. In the PISO algorithm, velocity is corrected explicitly: this means that the second correction is neglected and the whole error is assumed to be due to the error in the pressure term. This assumption is not true and makes it necessary to iterate the calculus procedure to achieve the correct solution. In other words, the PISO loop consists of an implicit momentum predictor followed by a series of pressure solutions and explicit velocity corrections (Jasak 1996).

The transient solution procedure we use for the solution of the entire problem can be summarized as follows:

- ✓ Assembling and solving the momentum predictor equation.
- ✓ Go through the PISO loop till the tolerance for pressure-velocity system is reached. At this stage, pressure and velocity fields for the current time-step are obtained.
- ✓ Solve all the other equations in the system.

The procedure have to be iterated till the reaching of the final time.

2.3.3.2. The Strang splitting scheme

The numerical scheme consists of splitting the equations into sub-equations, and integrating each one separately and sequentially. Typically, each sub-equation describes only one part of the physics of the problem. The results of the integration at each sub-step are combined to approximate the final solution with high accuracy(Strang 1968).

Let us consider the equations of transport:

$$\frac{\partial \boldsymbol{\varphi}}{\partial t} = \boldsymbol{M}(\boldsymbol{\varphi}, \boldsymbol{u}(\boldsymbol{\varphi}), t) + \boldsymbol{S}(\boldsymbol{\varphi}, \boldsymbol{u}(\boldsymbol{\varphi})) \tag{2.19}$$

where $\boldsymbol{\varphi}$ comprehend the entire set of species composition and the temperature. Therefore it is a vector of NS+1 variables written as $\boldsymbol{\varphi}=[\omega_1, \omega_2,\dots \omega_{NS}, T]$. Furthermore $\boldsymbol{M}$ denotes the transport processes due to diffusion and convection, and $\boldsymbol{S}$ denotes the source term due to chemical reactions. The dependent variables $\boldsymbol{\varphi}$are called primary variables and the variables $\boldsymbol{u}$ depend on the previous ones and are called secondary variables.

In our case the $\boldsymbol{S}$ term is stiff and highly non-linear in concentrations and temperature. The $\boldsymbol{M}$ term instead presents a low stiffness and a quasi-linear nature. In fact the non-linearity is dictated only by the presence of the secondary variables, e.g. density dependence on temperature.

Instead of solving the entire system, the Strang method provides the splitting of these equations in two systems of equations, the first taking into account only the reaction term and the second one considering only the transport term. The resulting system can be represented in this way:

$$\begin{cases} \dfrac{\partial \varphi_1}{\partial t} = S\big(\varphi_1, u(\varphi_1)\big) \\ \dfrac{\partial \varphi_2}{\partial t} = M(\varphi_2, u(\varphi_2), t) \end{cases} \tag{2.20}$$

$$\overline{}$$

$$\frac{\partial \varphi}{\partial t} = M(\varphi, u(\varphi), t) + S(\varphi, u(\varphi))$$

The Jacobian matrix of the whole system of PDEs that takes into account the reaction is block-unstructured and sparse (Figure 2.4). The Jacobian matrix has the dimension of $N_C \times NU$, where N_C is the total number of computational cells and NU is the number of unknowns, given by the sum of species, three components of velocity, pressure and temperature. The Jacobian of each cell is dimensioned as $NU \times NU$.

By adopting the Strang splitting scheme and the segregated approach the Jacobian matrix of convective and diffusive terms is transformed into a group of Jacobians with the same sparseness of the global matrix and dimensioned $N_C \times NU$.

The Jacobian matrix that describes the reactive terms becomes a diagonal blocks matrix. Indeed the rate of production of each cell depends only on the conditions of the cell itself. This implies that the system of PDEs can be turned into a group of decoupled Ordinary Differential Equations (ODEs) system. The resulting numerical problem is constituted by a system of quasi-linear PDEs and a group of non-linear ODEs system.

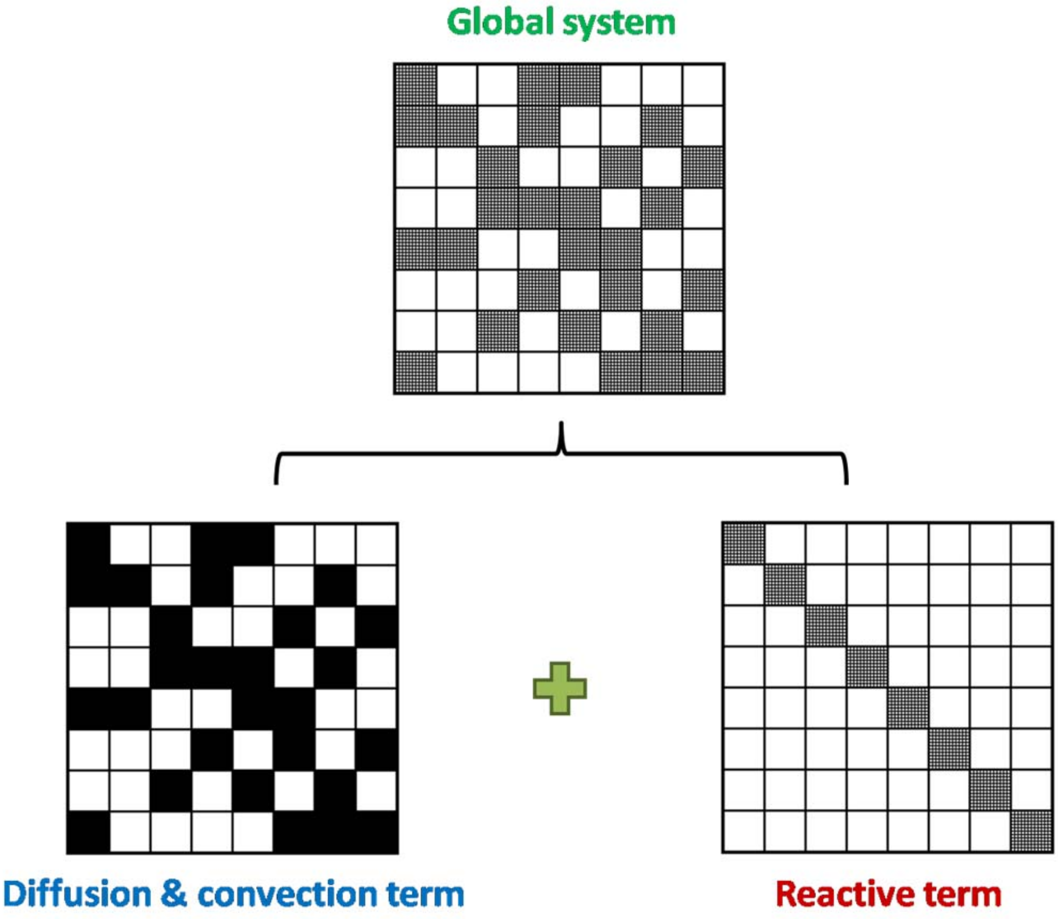

Figure 2.4. Jacobian matrix of the PDEs and ODEs systems.

A computationally efficient solution of the system is obtained through the use of the modified Strang splitting scheme with a predictor-corrector step. This method computes the predictor value integrating the ODEs system on the whole time step Δt. The system solved are stiff, decoupled and dimensioned as $NS+1$.

Then the transport equations are solved using the obtained values as initial conditions: once again integration is performed over the same time step Δt. The corrector consists of the integration of the PDEs with an Euler implicit algorithm in order to obtain the values of temperature and mass fractions are computed. The final solution is second order accurate in time (Pope and Zhuyin 2008). In Figure 2.5 a schematization of the integration over time according to the Strang splitting scheme is provided.

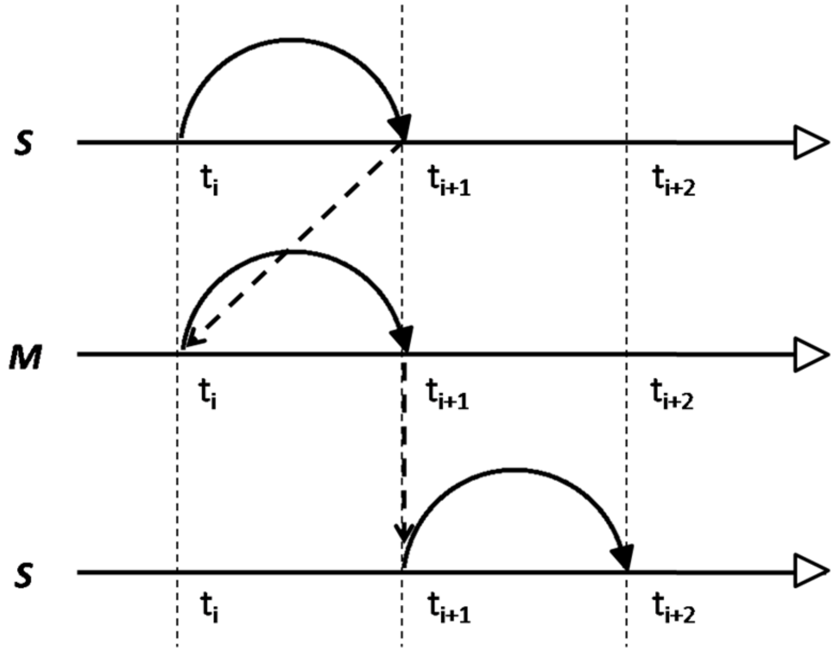

Figure 2.5. Schematization of time splitting.

The main advantage of using a splitting scheme is the possibility to adopt the best numerical algorithm for each sub-system. In Figure 2.6 a schematization of the Strang predictor-corrector method is given.

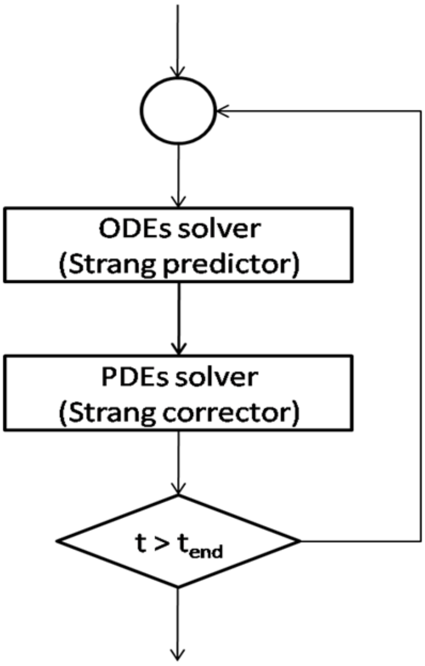

Figure 2.6. Diagram of the Strang predictor-corrector method.

The reacting sub-system requires a specific integrator for non-linear and stiff ODEs systems. In our case we use the BzzOdeStiffObject routine (Buzzi-Ferraris 2011) based on the Gear's algorithms (Gear 1971). Nevertheless, in principle any available solver for stiff ODE systems can be adopted. The transport sub-system has a low stiffness and is quasi-linear: it is then possible to adopt a segregated approach.

2.3.3.3. Physical model

In the previous section a detailed description of the modified Strang splitting scheme is given. Here the application of this method to our problem is provided. In our case, the expression of the generalized transport equation (2.19) is:

$$\frac{\partial \rho \phi}{\partial t} + \nabla \cdot (\rho \boldsymbol{U} \phi) - \nabla \cdot (\Gamma \nabla \phi) = \boldsymbol{S} \tag{2.21}$$

where $\boldsymbol{S}$ is the source term due to chemical reaction. It is possible to apply the modified Strang scheme with predictor-corrector sub-steps to Eq. (2.12).

The predictor takes into account the variations of species composition owed to chemical reactions. Since reactions take place both in the gas and adsorbed phase, it is required to discriminate the cells neighbouring the catalyst (catalytic cells) from the other ones (homogeneous cells). A schematization of the system is given in Figure 2.7.

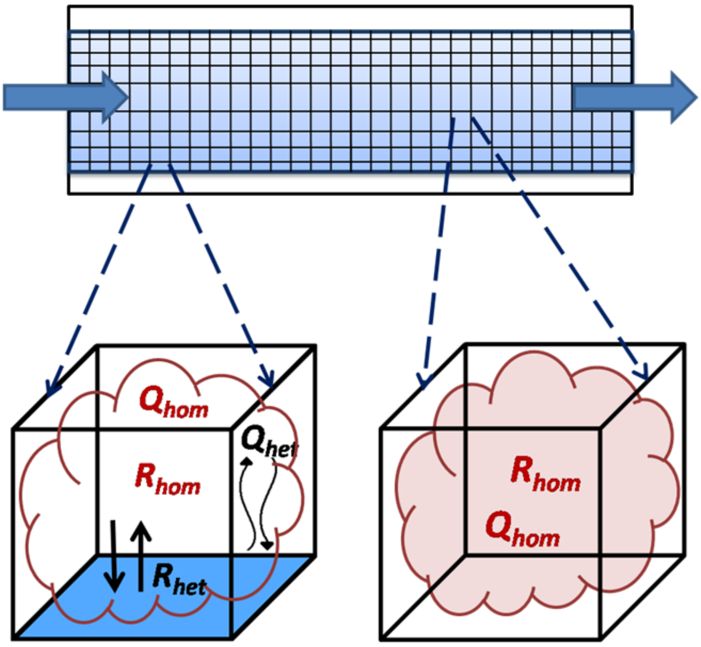

Figure 2.7. Scheme of boundary reacting cell

As shown in Figure 2.7, while the homogeneous cells contain only the gas phase reactions, the catalytic cells involve the heterogeneous reactions too.

The predictor values for an homogeneous cell are calculated by solving the following system of equations (see Appendix A):

$$\begin{cases} \rho \dfrac{d\omega_i}{dt} = \displaystyle\sum_{j=1}^{NR} R_j^{hom} \nu_{ij} MW_i \\ \\ \rho c_p \dfrac{dT}{dt} = Q^{hom} \end{cases} \tag{2.22}$$

where R_j^{hom} is the homogeneous reaction rate and Q^{hom} is the net heat of production of the gas phase species. The mass balance of the *i*th species is written for each component of the gas mixture.

For the catalytic cells the expression of the predictor system have to take into account additional terms. Indeed in these cells the flowing gas adsorbs on the catalytic surface: adsorbed species react through a number of elementary steps and desorb in the gas phase. Therefore, to describe the evolution of the catalytic surface it is necessary to:

- ✓ Add the heterogeneous reaction term to gas phase balances. This takes into account the adsorption and desorption reactions at the catalytic surface.
- ✓ Introduce a term to satisfy the total mass balance on the gas-phase. Since our solver has to be able to describe transient behaviour, the mass balances of the gas phase has to include the sum of the production rates over each component due to chemisorption reactions.
- ✓ Consider site conservation balances of the adsorbed species, according to e.g. (Maestri, Beretta et al. 2008). These include both surface and chemisorption reactions.

Mathematically the ODEs system becomes:

$$\begin{cases} \dfrac{d\omega_i}{dt} = \dfrac{\tilde{R}_i^{hom} MW_i}{\rho} + \dfrac{1}{\rho V_{react}} \left[\displaystyle\sum_{k=1}^{NCF} \alpha_{cat}^{(k)} A_{face}^{(k)} \left(\tilde{R}_{ik}^{het} MW_i - \omega_i \sum_{i=1}^{NC} \tilde{R}_{ik}^{het} MW_i \right) \right] \\ \dfrac{dT}{dt} = -\dfrac{1}{\rho \widehat{c_p}} \displaystyle\sum_{i=1}^{NCF} \widehat{H}_i^{hom} \widehat{R}_\imath + \dfrac{1}{\rho \widehat{c_p} V} \sum_{k=1}^{NCF} \alpha_{cat}^{(k)} A^{(k)} \sum_{i=1}^{NCF} \tilde{R}_{ik}^{het} MW_i (\widehat{H}_{ik}^{het} - \widehat{H}_i^{hom}) \\ \Gamma_{site} \dfrac{\partial \vartheta_i}{\partial t} = \displaystyle\sum_{j}^{NCF} R_{j,sur} \nu_{ij} \end{cases} \tag{2.23}$$

where $R_{j,sur}$ is the production rate of the ith surface species and Γ_{site} denotes the catalyst site density, $A_{face,j}$ is the area of the cell of the catalytic surface,V_{cell} is the volume of that cell and $\widehat{H}_{tot}$ is .*NCF* is the Number of Catalytic Faces of the cell. The mass balance of the *i*th gas species is written for each component of the gaseous mixture. The site conservation equation is written for each adsorbed species including the free catalytic sites for each catalytic face.

In order to account for the surface coverage of the reactor wall, we introduced the α_{cat} parameter, calculated as the ratio of the effective catalytic area over the geometric surface. This simple approximation serves as moderator of the catalytic activity. However it does not allow to properly describe the internal mass transfer phenomena.

After solving the predictor step it is necessary to solve the corrector which is described by a PDEs system. As seen in section 2.3.3.1 the numerical problem is quasi-linear and has a low stiffness degree. Therefore a segregated approach can be adopted. Species and temperature transport equations are solved decoupled in the following form:

$$\frac{d(\rho\omega_i)}{dt} + \nabla \cdot (\rho \boldsymbol{U} \boldsymbol{\omega_i}) - \nabla(\rho \mathcal{D}_\mathrm{i} \nabla \mathrm{\omega_i}) = 0 \tag{2.24}$$

$$c_p \frac{\partial(\rho T)}{\partial t} + c_p \nabla(\rho T) - \lambda \nabla^2 \mathrm{T} = 0 \tag{2.25}$$

In Figure 2.8 a physical interpretation of the procedure of solution is given. The predictor describes an ensemble of perfectly mixed batch reactors. The corrector represents the mass and energy exchange between these reactors.

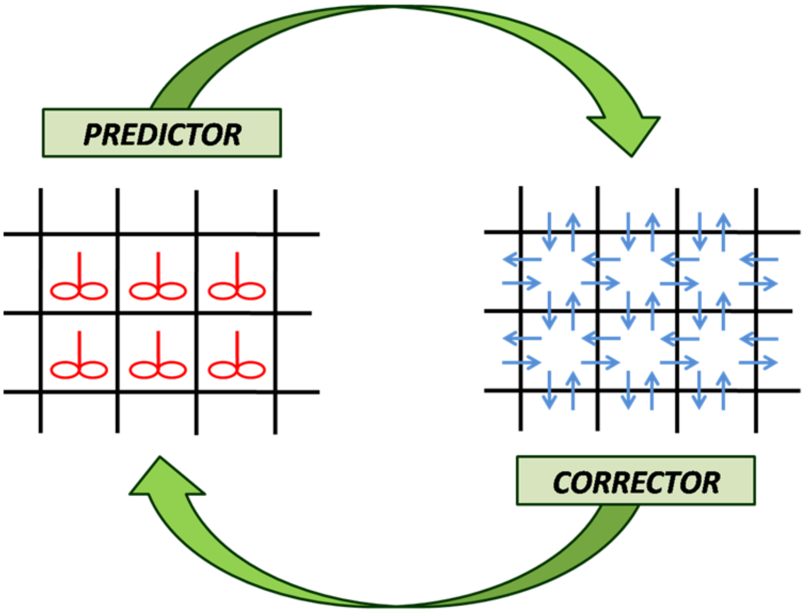

Figure 2.8. Physical interpretation of the predictor-corrector routine.

According to (Pope and Zhuyin 2008) even if this method requires the solution of the ODEs system for each cell of the computational mesh, the final solution obtained is second order accurate in time. Moreover it is much less computationally demanding than solving the entire PDEs system in a fully coupled approach.

The calculation of the formation rate of gaseous species is achieved by the OpenSMOKE®library. For the computation of chemisorption reaction rate of both phases and the calculation of surface reaction rates the CatalyticSMOKE library has been used. Further details are provided in Chapter 3.

2.3.4. The catalyticFOAM structure

The catalyticFOAM structure is organized in more levels, as shown in Figure 2.9.

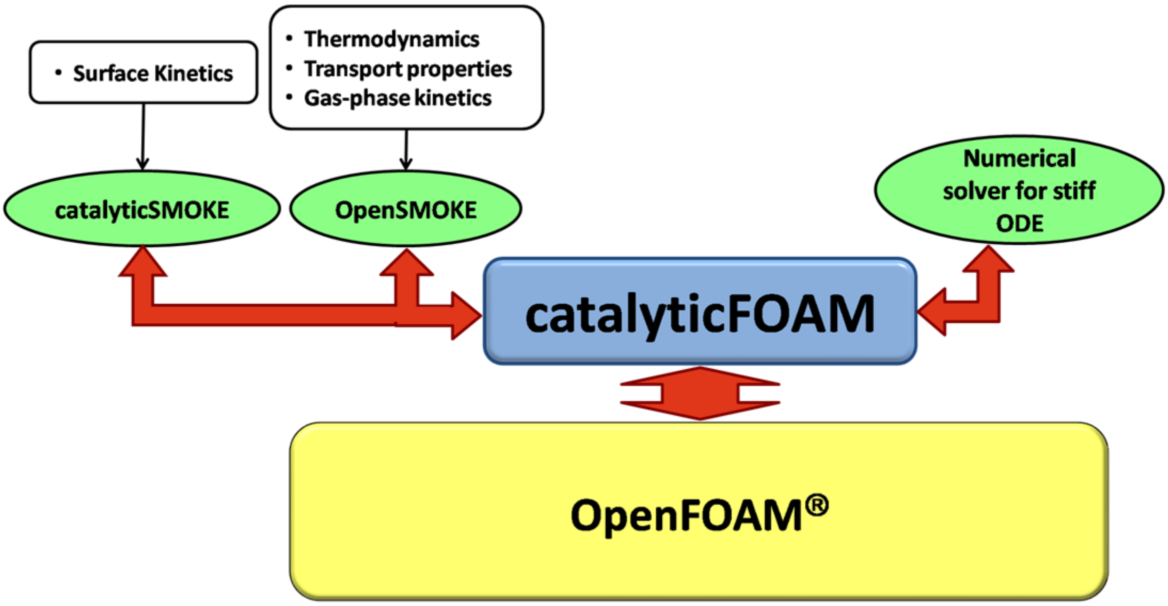

Figure 2.9. Schematization of the catalyticFOAM structure.

The whole program is based on the OpenFOAM®framework, that handles the discretization and solution procedures via FVM. The catalyticFOAM solver contains the entire set of equations and manages the solution procedure. At each iteration the PDEs are transmitted to OpenFOAM®and solved. Instead, the ODEs system is solved for each cells by the BzzMath library. The thermodynamic and transport properties of the gas phase are calculated by the OpenSMOKE® library, using the CHEMKIN standard correlations(ReactionsDesign 2008). Furthermore, the computation of gas phase kinetic is achieved by OpenSMOKE® library. Instead, the surface kinetic is evaluated by the CatalyticSMOKE library.

A detailed description of the solution loop achieved by catalyticFOAM is given in Figure 2.10.

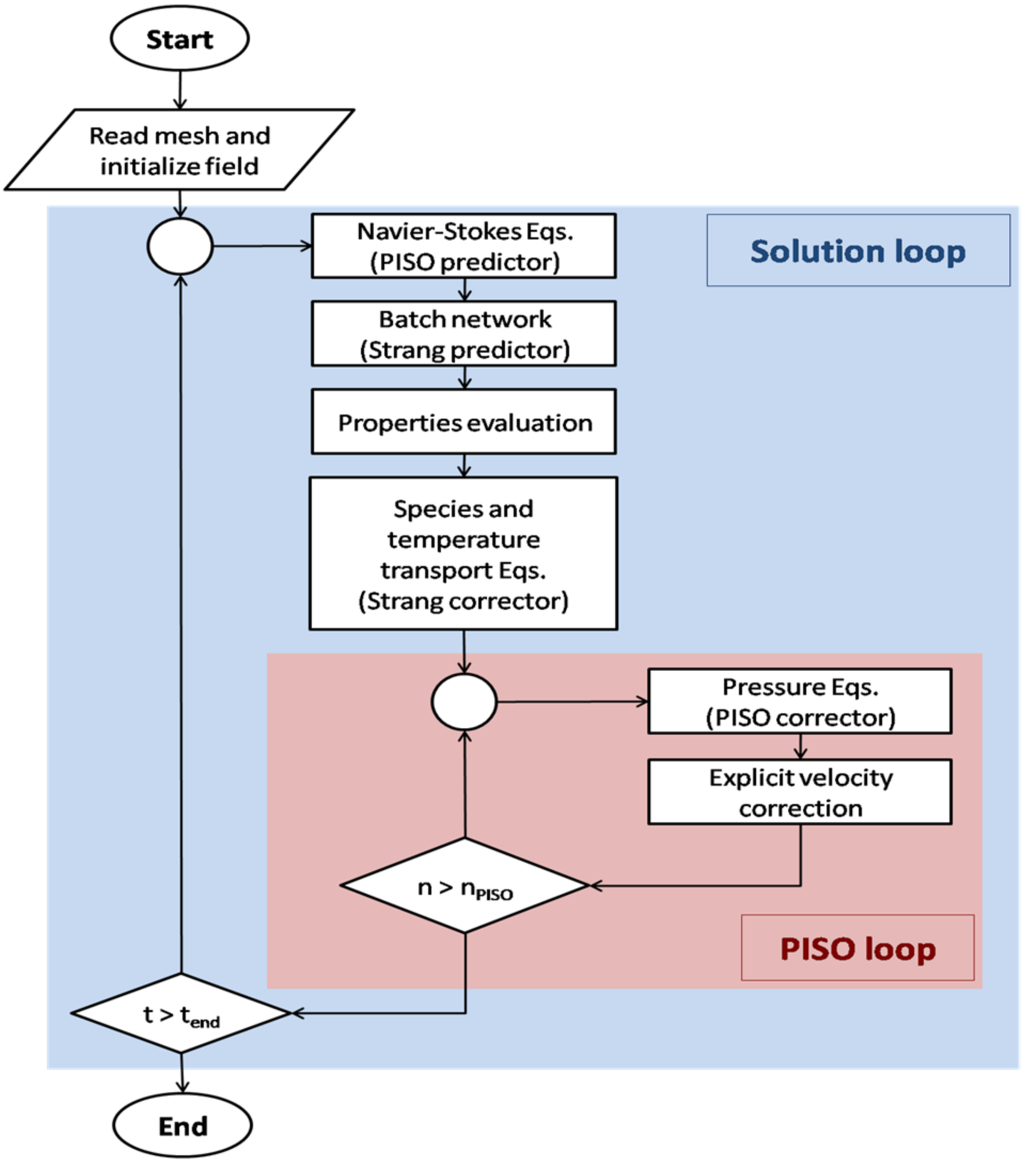

Figure 2.10. Schematization of the solution procedure of catalyticFOAM

Initially the geometric domain is discretized by the creation of the computational mesh. Then temperature, pressure, velocity and species concentrations are initialized. The iterative procedure starts with the implementation of the momentum equations. Then the ODEs system is solved and properties are updated. The transport equation is solved for each species at this point. Consequently the new temperature is computed. Finally the PISO loop start: the continuity equation is solved and the velocity field is corrected explicitly. The whole procedure is iterated till the reaching of the end time.

Chapter 3.

The kinetic library

In this section a detailed description of the kinetic library is provided. A general introduction is reported in 3.1. The gas-phase kinetics is handled by the OpenSMOKE library, described in 3.2.1. The heterogeneous kinetic mechanism is implemented in the CatalyticSMOKE library, illustrated in 3.2.2. The formalization of the surface kinetic mechanism is reported in 3.2.2.1 and the expressions for the computation of reaction rates are delineated in 3.2.2.2.

3.1. General overview

In the chemical industry the necessity to control reactions at the molecular level quickly increased within the requirement of more energy efficient and selective processes. In order to achieve this goal during most of the 20th century the approach consisted in proposing a rate equation and fitting it with experimental data to obtain the most suitable rate constants. Even though this method leads to powerful results, these models give satisfying results only in a narrow range of operating conditions (Dumesic, Huber et al. 2008).

In recent years kinetic models have been reinterpreted thanks to the possibility of modeling in detail the surface chemistry. Indeed, the aim of kinetic modeling is to provide valuable tools for the design of chemical reactors under a wide range of conditions and for the analysis and optimization of catalytic processes (Gokhale, Kandoi et al. 2004).

During the last years the attention has been focused on the kinetic models that try to incorporate the basic surface chemistry involved in the catalytic reaction (Schlögl 2001). This new prospective leads to the development of a new rational design of the catalyst based on predictive capability of first-principles models, without any experimental input. Even though, this approach still presents many challenges to overtake, in order to have a full description and control of all chemical transformations.

In this work, we develop a numerical library able to evaluate the heterogeneous reaction rates, called CatalyticSMOKE.

3.2. The kinetic libraries

In order to confer to the solver the maximum generality and flexibility, the catalyticFOAM tool can implement both gas-phase and surface reaction mechanisms. The kinetic scheme handling relies on two libraries, one for the homogeneous and the other for the heterogeneous phase. These are presented in the following section.

3.2.1. The OpenSMOKE library

The gas-phase is entirely managed by the OpenSMOKE library. This has been written in C++ by the CRECKmodeling group (Faravelli, Cuoci et al.) and provides an efficient handling of thermodynamic, transport and kinetic data (Faravelli, Cuoci et al. 2008; Faravelli, Cuoci et al. 2009).

In order to use the OpenSMOKE library two steps are required:

- ✓ The first one is the interpretation of the input files: in this phase the interpreter program reads information from files, checks if these are correct and consistent, elaborate data and print them in binary files. The input files contain respectively thermodynamic, transport and kinetic information and are written in the standard CHEMKIN® format (ReactionsDesign 2008).

- ✓ The second one is the computation of desired properties: binary files are read, data are saved in the Random Access Memory (RAM) to improve the speed of access and requested properties are calculated by calling the required functions.

The structure of the OpenSMOKE library is described in Figure 3.1.

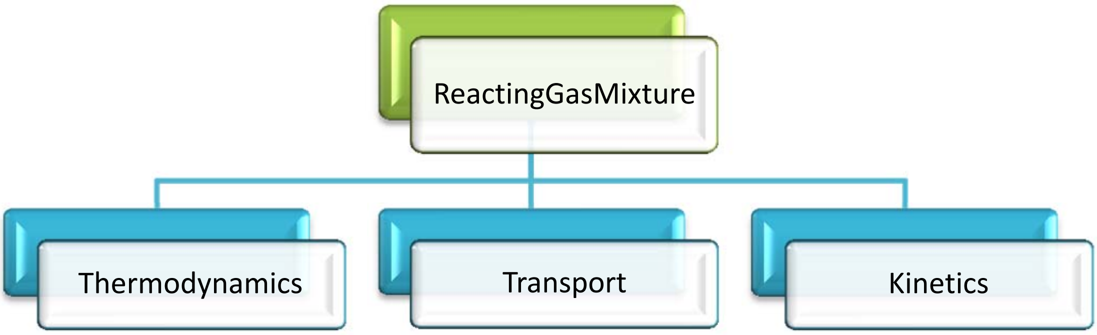

Figure 3.1. Schematization of the object-oriented library OpenSMOKE.

The main class is the “ReactingGasMixture”, that contains species data, e.g. molecular weight and species names, and a number of useful functions, e.g. conversion from molar to massive fractions and computation of the mean molecular weight of the gas mixture. Furthermore, it comprises references to:

- ✓ The “thermodynamic” class, which contains functions for the computation of thermodynamic properties such as enthalpy, entropy and specific heats.
- ✓ The “transport class”, which provides methods for the calculations of diffusivity, viscosity and other transport properties.
- ✓ The “kinetics” class, which comprises all the necessary functions for the computation of reaction rates and heats of reaction.

3.2.2. The CatalyticSMOKE library

For the handling of the heterogeneous kinetic scheme we developed the CatalyticSMOKE library. The main purposes of this instrument are:

- ✓ to provide the efficient handling of traditional kinetic schemes basing on the SURFACE CHEMKIN® standard format;

- ✓ to give the possibility to implement non-standard kinetic schemes, such as mechanisms based on Unity Bond Index-Quadratic Exponential Potential (UBI-QEP) mechanisms.

The organization of this tool is based on the OpenSMOKE library structure. Thus, two applications are required: the first one to read and interpret input files, the second to compute the desired properties. In the following, we provide a description of the entire library.

3.2.2.1. Input file

As previously said, the input file has to be written in the SURFACE CHEMKIN® format (ReactionsDesign 2008). The main features of this format are:

- ✓ broad generality: the SURFACE CHEMKIN® standard is adopted by the widest part of the scientific community;
- ✓ great flexibility: there is no limit to the number of materials, catalytic sites, adsorbed species and surface reactions in a single kinetic scheme;
- ✓ possibility to take into account standard, stick and coverage-dependent reactions;
- ✓ intuitive and easy-to-use interface.

One of the main tasks of our interpreter is that it is able to read and process data for UBI-QEP schemes. Furthermore it is possible to adopt both UBI and classic kinetic mechanisms. We inserted this option because this semi-empirical method provides an efficient approach for the detailed description of microkinetic behaviour of reacting systems (Maestri, Vlachos et al. 2009; Maestri and Reuter 2011).

This UBI-QEP technique is an hybrid theoretical method able to handle complex systems of reaction. In this mechanism the interactions among adsorbates species are taken into account in order to compute the energetics of the heterogeneous reactions. The UBI method compute the heat of surface reactions by considering a simple thermodynamic circle: the reactants desorb from the surface, react in the gas phase and products adsorb on the catalyst. For this reason the knowledge of the heats of chemisorption of each species are required. Further details on this are provided in Appendix B.

Since CHEMKIN® does not support UBI-QEP mechanisms and there is no standard codification for these schemes, we propose a new intuitive standard for the use of these mechanisms in engineering applications. An example of input data file is provided in Figure 3.2. The complete kinetic scheme is given in Appendix C.

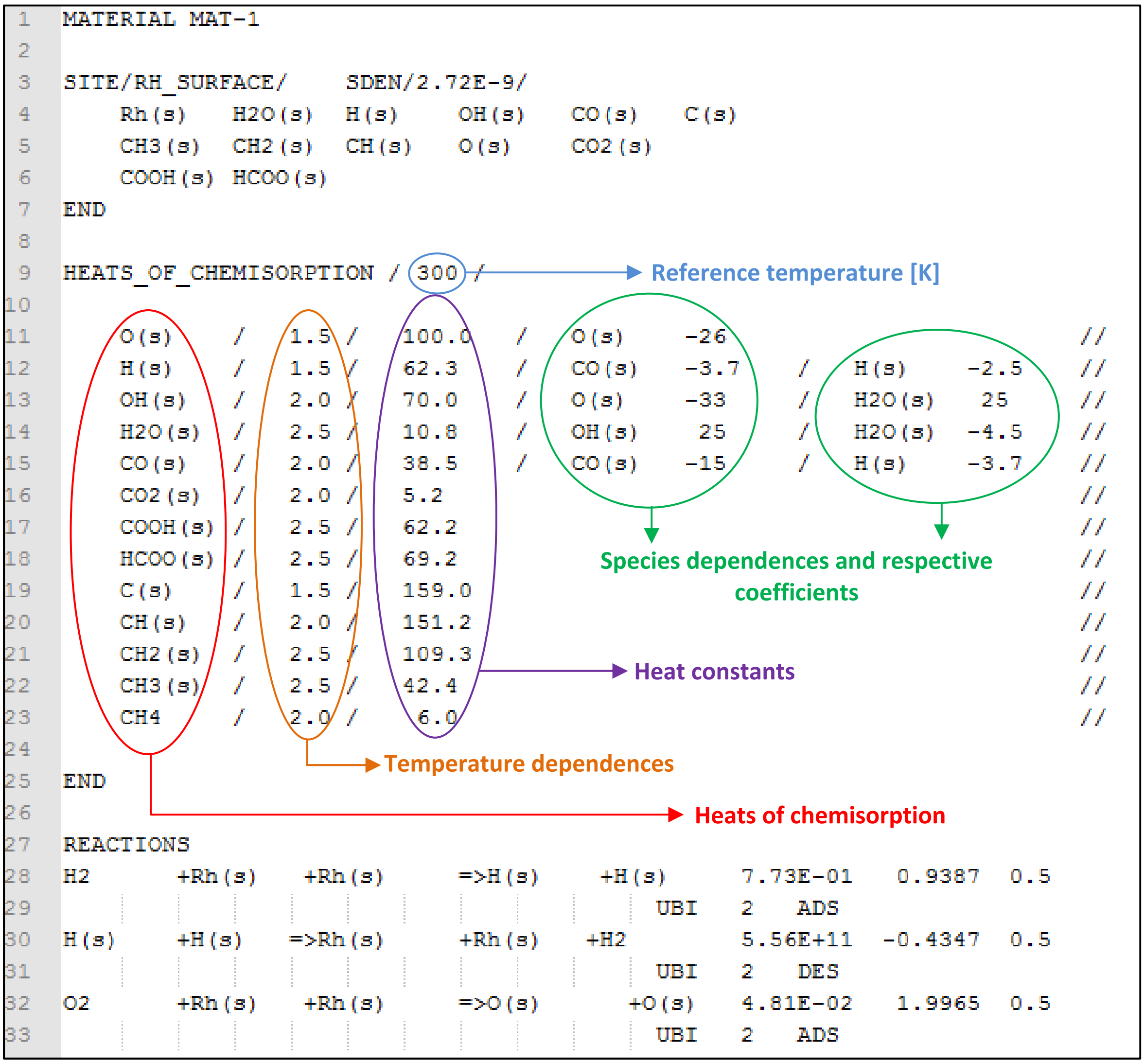

```
 1  MATERIAL MAT-1
 2
 3  SITE/RH_SURFACE/    SDEN/2.72E-9/
 4      Rh(s)   H2O(s)  H(s)    OH(s)   CO(s)   C(s)
 5      CH3(s)  CH2(s)  CH(s)   O(s)    CO2(s)
 6      COOH(s) HCOO(s)
 7  END
 8
 9  HEATS_OF_CHEMISORPTION / 300 /
10
11      O(s)    /   1.5 /   100.0   /   O(s)    -26                             //
12      H(s)    /   1.5 /   62.3    /   CO(s)   -3.7    /   H(s)    -2.5        //
13      OH(s)   /   2.0 /   70.0    /   O(s)    -33     /   H2O(s)   25         //
14      H2O(s)  /   2.5 /   10.8    /   OH(s)    25     /   H2O(s)  -4.5        //
15      CO(s)   /   2.0 /   38.5    /   CO(s)   -15     /   H(s)    -3.7        //
16      CO2(s)  /   2.0 /   5.2                                                 //
17      COOH(s) /   2.5 /   62.2                                                //
18      HCOO(s) /   2.5 /   69.2                                                //
19      C(s)    /   1.5 /   159.0                                               //
20      CH(s)   /   2.0 /   151.2                                               //
21      CH2(s)  /   2.5 /   109.3                                               //
22      CH3(s)  /   2.5 /   42.4                                                //
23      CH4     /   2.0 /    6.0                                                //
24
25  END
26
27  REACTIONS
28  H2      +Rh(s)   +Rh(s)     =>H(s)    +H(s)     7.73E-01   0.9387  0.5
29                                            UBI   2   ADS
30  H(s)    +H(s)   =>Rh(s)     +Rh(s)   +H2        5.56E+11  -0.4347  0.5
31                                            UBI   2   DES
32  O2      +Rh(s)   +Rh(s)     =>O(s)      +O(s)   4.81E-02   1.9965  0.5
33                                            UBI   2   ADS
```

Figure 3.2. Example of input data file for a UBI-QEP kinetic scheme.

The declaration of the surface material and adsorbed species is the same of the SURFACE CHEMKIN® format. The keyword HEATS_OF_CHEMISORPTION indicates the declaration of the correlations for the computations of heats of chemisorption of gas-phase species. The reference temperature of these values is written in Kelvin at line 9.

From line 11 to line 23 the expressions for the heats of chemisorption are given. Since their value is computed by Eq. 3.2, one has to specify the *i*th species, the temperature dependence k, the heat constant Q_i and the coefficient of coverage-dependence $a_{i,j}$ of the jth species.

$$Q_i(T) = \left[Q_i(T_0) + \sum_{j=1}^{NAS} a_{i,j}(T_0)\theta_j \right] - kR(T - T_0) \qquad (3.1)$$

The second part of the UBI-QEP kinetic scheme consists of the declaration of surface reactions. These are written in a CHEMKIN® like format: it is noticeable that the use of the reversible reaction operator "<=>" is not possible, since each reaction has to be coupled with the respective inverse. The three values indicated near the reaction respectively stands for the turnover frequency, the temperature exponent and the bond index. Under the reaction three labels are printed in sequence: the first one indicates that the reaction is of UBI type, the second one shows the kind of surface reaction and the third one allows to distinguish among adsorption, desorption and surface reactions.

The input file previously described is then elaborated and the kinetic parameters are stored in a binary file named "surface.bin".

3.2.2.2. Library structure

The kinetic parameters stored in the binary file can be read by the CatalyticSMOKE library. The structure of this computational tool is described in Figure 3.3.

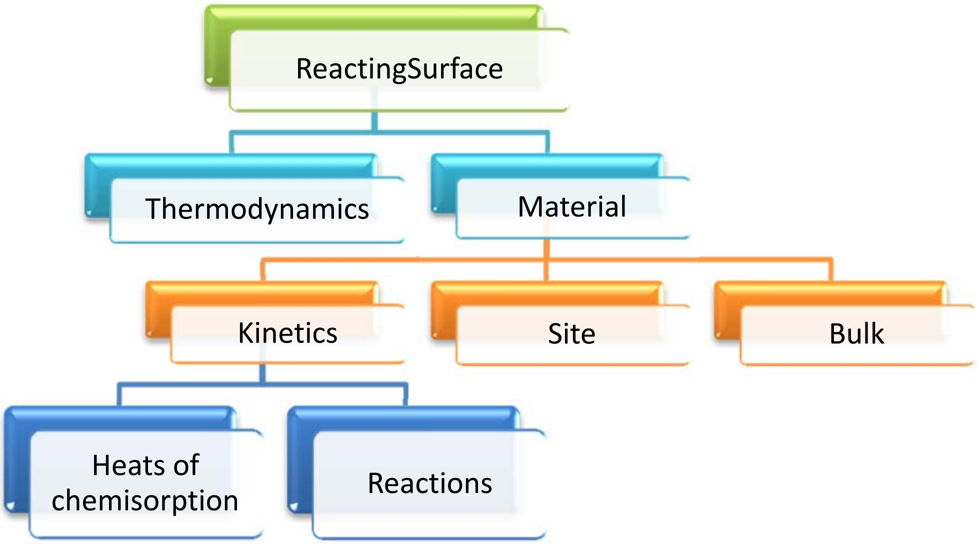

Figure 3.3. Schematization of the structure of the CatalyticSMOKE library.

The main class is “ReactingSurface” and contains references to “Thermodynamics” and “Material” classes. The former provides information on the thermodynamic properties, the latter contains the material properties and is linked to the “Site”, “Bulk” and “Kinetics” classes. The most important is the last one: this contains information about the kinetic scheme adopted and manages the calculations of heats of chemisorption. Furthermore, it is linked to the “Reactions” class, which comprises all the reaction parameters and methods.

In order to exploit the potentiality of C++ language and in particular of object-oriented design, each component of the CatalyticSMOKE library is arranged as an object. Specifically, each object has its own methods and can be evoked by hierarchically superior objects. The function that computes the reaction rates is the most important of the CatalyticSMOKE library. This can be recalled from the main program by pointing to the main class. The function execute a loop over the materials considered in the kinetic scheme. Since the single material can be composed by one or more active elements, the computation of the reaction rates is accomplished for each kind of site. The information about the kinetic schemes are contained in the “Kinetic” class, while the properties of each site, e.g. site density, are grouped in the “Site” class. The reaction rate evaluation in made by recalling each “Reaction” object, which contains all the necessary data, e.g. activation energy, pre-exponential factor.

3.2.2.3. Surface reaction rates computations

The CatalyticSMOKE interpreter requires the declaration of both direct and inverse reaction. This allows to compute the heats of reaction as:

$$\Delta H_j = E_{f,j} - E_{b,j} \tag{3.2}$$

where $E_{f,j}$ and $E_{b,j}$ are the forward and the backward activation energies of the *j*th reaction. This relationship is required to ensure the enthalpic consistency.

The CatalyticSMOKE library has two tasks: the first one is to provide information on the surface kinetic scheme, e.g. number of materials involved, site densities, species. The second is to compute production and consumption rates of each component.

There are four ways in which this can be achieved.

- ✓ The first one is employed for standard reaction types: the kinetic constant is expressed by the modified Arrhenius formula (Eq. 3.3):

$$k_j = A_j T^{\beta} \exp\left(-\frac{E_{att,j}}{RT}\right) \tag{3.3}$$

- ✓ The second is used in case of sticky reactions, i.e. for those adsorption reactions in which the probability of the molecule of sticking on the catalyst is expressed by the probability factor γ, named sticking coefficient, as expressed in Eq. 3.4:

$$\gamma_j = \min\left[1, a_i T^{b_i} \exp\left(\frac{c_i}{RT}\right)\right] \tag{3.4}$$

where a_i, b_i and c_i are the pre-exponential factor, the temperature exponent and the activation energy of the sticking coefficient.

The rate constant is then calculated as shown in Eq. 3.5:

$$k_j = \gamma_j \frac{\prod \sigma_{j,i}^{\nu'_{i,j}}}{(\Gamma_{site})^m} \sqrt{\frac{RT}{2\pi MW_j}} \tag{3.5}$$

where $\sigma_{j,i}^{\nu'_{i,j}}$ is the number of sites that each adsorbed species occupy, elevated to the respective reaction order, $\Gamma_{site}$is the site density and MW_j is the molecular weight of the gas-phase species.

- ✓ The third is adopted when the reaction rate depends on the surface coverage of the catalyst. In this case the rate constant is expressed by Eq. 3.6:

$$k_j = A_j T^{\beta} \exp\left(-\frac{E_{att,j}}{RT}\right)$$

$$\prod_{i=1}^{NS_j} 10^{\eta_{ij}[\theta_i(n)]} [\theta_i(n)]^{\mu_{ij}} \exp\left(-\frac{\varepsilon_{ij}\theta_i(n)}{RT}\right) \tag{3.6}$$

$$\prod_{i=1}^{NB_j} 10^{\eta_{ij}[a_i(n)]} [a_i(n)]^{\mu_{ij}} \exp\left(-\frac{\varepsilon_{ij}a_i(n)}{RT}\right)$$

where η_{ij} , μ_{ij} and ε_{ij} are the experimental parameters for the coverage dependence of the kinetic constant, $\theta_i(n)$ is the site fraction of the *i*th species on the *n*th material and $a_i(n)$ is the bulk fraction of the *i*th species in the *n*th material.

- ✓ The fourth choice is the calculation of reaction rates according to the UBI-QEP method. In contrast to the previous options, this one is not implemented in the SURFACE CHEMKIN® framework. Further details on the UBI-QEP method are provided in Appendix B. Here we provide the computation procedure for reaction rates in UBI kinetic schemes.

  First of all it is necessary to specify that the UBI-QEP approach assumes that the activation energies of reaction are not constant, and thus they have to be computed at each iteration. Since the activation energies of forward and backward reaction are linked by Eq.(3.1), it is convenient to compute them coupled.

  The first step of the procedure consists of the calculation of the dissociation energy of species involved in the reaction. Thus, it is necessary to write the dissociation reaction in the gas-phase:

$$\begin{gathered} AB \rightarrow A + B \\ E_d = H_A + H_B - H_{AB} \end{gathered} \tag{3.7}$$

  It is noticeable that a much simpler expression can be adopted to compute the dissociation energy without taking into account the dissociation reaction of each component. Let us consider the generic surface reaction of Eq.(1.8):

$$AB(s) + CD(s) \rightarrow AC(s) + BD(s) \tag{3.8}$$

  It is possible to write down the dissociation reaction in the gas-phase for each component, as shown in Eq.(3.9)

$$\begin{gathered} AB \rightarrow A + B \\ CD \rightarrow C + D \\ AC \rightarrow A + C \\ BD \rightarrow B + D \end{gathered} \tag{3.9}$$

The dissociation energy can be calculated as previously shown.

$$E_{d,j} = \sum_{i=1}^{NR} \nu_{ij}\, E_{d,ij} - \sum_{j=1}^{NP} \nu_{ij} E_{d,ij} =$$

$$= H_A + H_C - H_{AC} + H_B + H_D - H_{BD} - (H_A + H_B - H_{AB} + H_C + H_D - H_{CD}) = H_{AB} + H_{CD} - H_{AC} - H_{BD} \tag{3.10}$$

It is easy to see that the final expression reduces to:

$$E_{d,j} = \sum_{i=1}^{NP} \nu_{ij} H_i - \sum_{j=1}^{NR} \nu_{ij} H_i \tag{3.11}$$

It is important to notice that the dissociation reactions that have to be considered are in the gas phase. This means that for each surface species a corresponding gas-phase component has to be present.

The dissociation energy of forward reactions has to be positive because one of the assumptions on which the UBI-QEP method is based is that the dissociated species are more stable than the entire molecule. A more detailed explanation is provided in Appendix B. Furthermore, it can be noticed from Eq.(3.11) that forward and backward reactions have opposite dissociation energies. This implies that this parameter is calculated once for both reactions. The sign of the dissociation energy determines whether the reaction is forward or backward.

Now it is possible to compute the heat of reaction using the expression of Eq.(3.12):

$$\Delta H_j = E_{d,j} + \sum_{i=1}^{NR} \nu_{ij} Q_i - \sum_{i=1}^{NP} \nu_{ij} Q_i \tag{3.12}$$

where Q_i stands for the heat of chemisorption of the *i*th component. These are computed with Eq.(3.2).

The activation energy of the reaction can be now computed. The exact expressions are reported in Appendix B**.** The backward activation energies are calculated by using Eq.(3.1).

Since activation energies can be either positive or zero, it is necessary to check the obtained values. Specifically, if E_f or E_b becomes negative, it is set to zero and the other one equal to the heat of reaction. More details are provided in Appendix B.

The kinetic constant of the *j*th reaction is computed by the expressions reported in Eq.(3.13). The first one is used for desorption and superficial reactions, the second one is employed for adsorption reactions.

$$k_j = \frac{s_j}{(\Gamma_{site})^{m-1}} \left(\frac{T}{T_0}\right)^{\beta} \exp\left(-\frac{E_{att,j}}{RT}\right)$$

$$k_j = \frac{s_j}{(\Gamma_{site})^{m}} \sqrt{\frac{RT}{2\pi MW_j}} \left(\frac{T}{T_0}\right)^{\beta} \exp\left(-\frac{E_{att,j}}{RT}\right) \tag{3.13}$$

The reaction rate is then computed using Eq.(3.14).

$$r_j = k_j (\Gamma_{site})^m \prod_{i=1}^{NAS} \theta_j^{\nu_{ij}}$$

$$r_j = k_j (\Gamma_{site})^m x_{g,i}^{\nu_{ij}} \prod_{i=1}^{NAS} \theta_j^{\nu_{ij}} \tag{3.14}$$

where $x_{g,i}^{\nu_{ij}}$ is the mole concentration of the *i*th gas species elevated at the respective stoichiometric coefficient.

Chapter 4.

Numerical tests

In this chapter, first we present a series of numerical tests made in order to analyze the performance of the new solver catalyticFOAM. A general overview on the simulation test case is provided in the first section. The numerical issues regarding spatial and temporal discretization are pointed out in section 4.2. In the last section, the study on the computational time is reported.

4.1. Introduction

In order to investigate the performances of the solver, a sequence of numerical tests have been performed. Before proceeding with the validation of the tool with experimental data, it is compulsory to assess the convergence of solution with respect to the calculated parameters. In particular, the effects of changing the temporal step and the number of spatial grid cells are investigated. These parameters have a great influence in the resolution of the numerical problem: for example, increasing the number of cells the accuracy of the final solution increases, but the total amount of computational time increases too. Hence, the aim of this analysis rises also from the necessity to optimize the accuracy of the solution and the computational costs required for the simulation. A sensitivity analysis is made by modifying these parameters. Then, the best set of values obtained is used to generate an accurate and reliable output.

Since the OpenFOAM® software is widely used and its reliability is well assessed, in this discussion it is assumed that velocity and pressure fields are correctly computed.

The test case selected for these numerical tests is taken from (Maestri, Beretta et al. 2008). In Chapter 5 the simulations results are compared to the experimental data provided in the article. Maestri and co-workers developed a dynamic two-dimensional model of a catalytic annular reactor and validated it comparing model and experimental results. A UBI based kinetic scheme for the combustion of hydrogen on rhodium was used, as reported in Appendix C. The simulations were performed under isothermal and isobaric conditions. A schematic representation of the catalytic reactor is given in Figure 4.1.

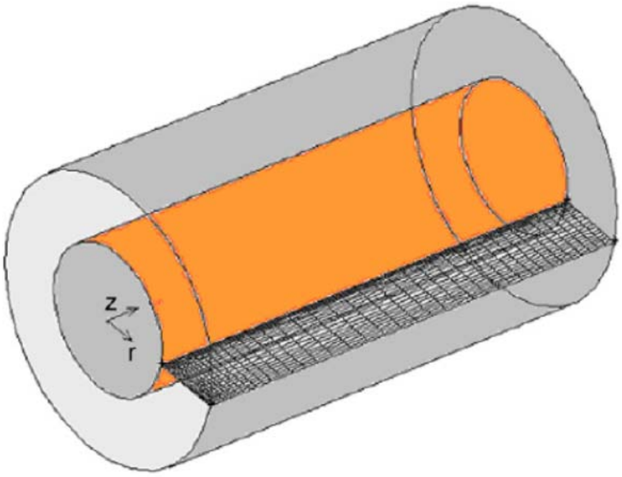

Figure 4.1. Sketch of the annular catalytic reactor, adapted from (Maestri, Beretta et al. 2008).

As shown in Figure 4.1, the Rh/α-Al_2O_3 catalyst is deposited over the surface of the inner wall of the reactor (colored in orange).

Operating conditions	
Inner radius	0.235 cm
Outer radius	0.450 cm
Reactor length	1.5 cm
O_2 mole fraction	0.04 (-)
H_2 mole fraction	0.01 (-)
N_2 mole fraction	0.95 (-)
Pressure	1atm

Table 4.1. Simulation parameters.

The operating conditions and the geometric parameters of the reactor are presented in Table 4.1. The ratio between catalytic area and effective reactor volume (V_{react}) is known and is called a_{cat}. From this parameter the α_{cat} is obtained by Eq. 4.1.

$$\alpha_{cat} = a_{cat}\frac{V_{react}}{A_{react}} \tag{4.1}$$

where A_{react} is the geometric area of the catalytic surface.

The spatial discretization of the geometrical domain was simplified in order to reach the steady state conditions with a smaller computational effort. Specifically, thanks to the symmetry of the annular reactor, it is possible to consider only one slice of this reactor. This is very convenient because this allows one to consider a 2D mesh instead of a 3D one. The 2D mesh is obtained considering the slice of a cylinder with a width of 5°. The number of required cells is thus 72 times lower than the one required for a 3D grid. A schematic view of the mesh is presented in the Figure 4.2.

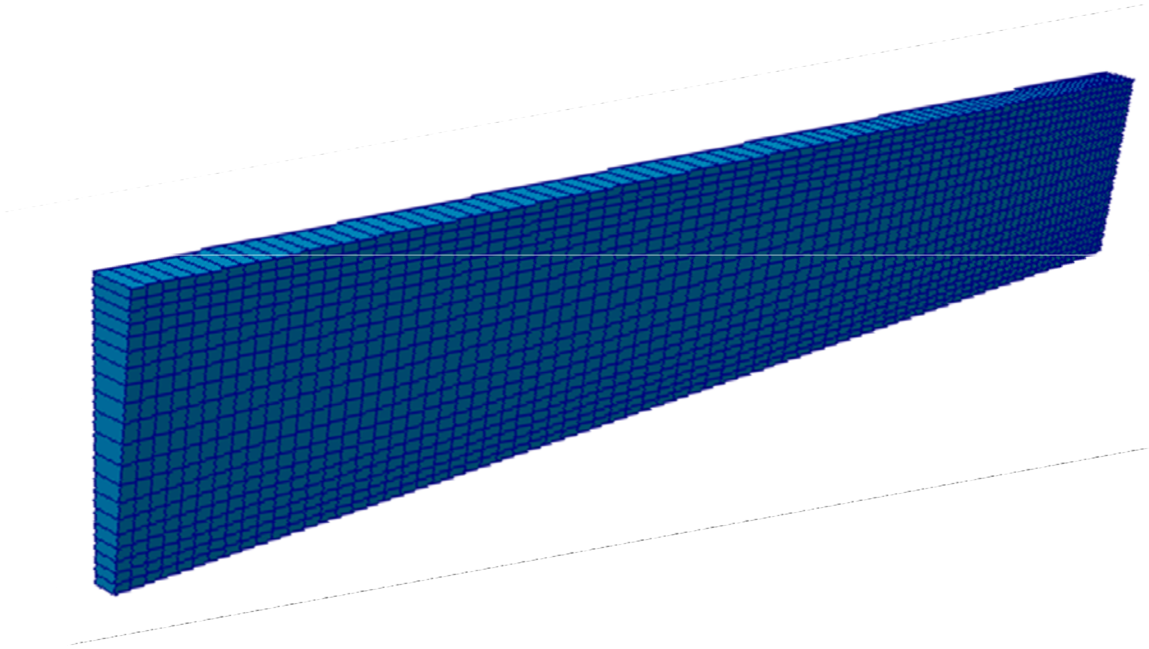

Figure 4.2. 2D mesh used for the numerical simulation.

As shown in Figure 4.2, the geometrical domain is divided in a series of cells by partitioning the axial and radial coordinates. The simulations are performed over an optimized mesh composed by 250 units in axial direction and 24 units in the radial one for an overall amount of 6000 cells. Further details about the optimized number of cells are provided in the following sections.

In addition the grid is refined with a specific grading, i.e. the length of each cell of the mesh is not constant. The expansion ratio of the cells is calculated as the ratio among the length of the first and the last cell along one edge of a block. This enables the mesh to be graded, or refined, in specified directions for a specific factor. The introduction of a non-constant step grid allows one to describe certain areas of the system in a more detailed way. In our case, since the zone close to the catalyst is interested by strong normal gradients, the mesh is highly refined near the catalytic wall in the radial direction. A further grading was introduced in the axial direction to provide a proper description of the rapid consumption of reactants at the reactor inlet.

For the temporal discretization a Courant number of 0.1 is adopted.

In order to provide an exhaustive analysis on the performance of catalyticFOAM, the simulations are performed at two different temperatures. In the first case (423.15 K) the system is under chemical regime, in the second one (773.15 K) it is controlled by mass transfer phenomena.

The convergence tests were performed on an Intel core i7 950 CPU @ 3.07 GHz with 8 GB of available RAM memory. In the following the main results of these numerical tests are presented.

In Figure 4.3 the velocity profiles for the two temperatures investigated are reported.

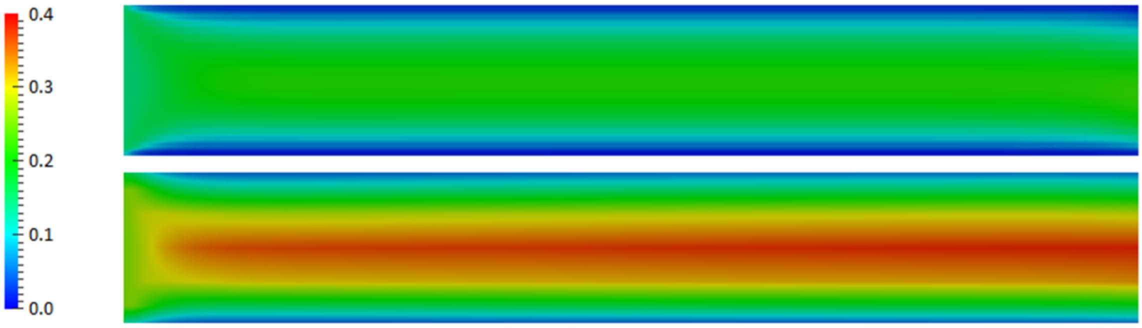

Figure 4.3. Velocity magnitude profiles [m s^{-1}] at 423.15 K and 773.15 K.

Since the inlet flow is constant, the velocity is higher in the second case (773.15 K). It can be noticed that the flow is laminar and thus the radial profile of velocity is parabolic.

In Figure 4.4 and 4.5 the O_2 and H_2O molar fractions are reported.

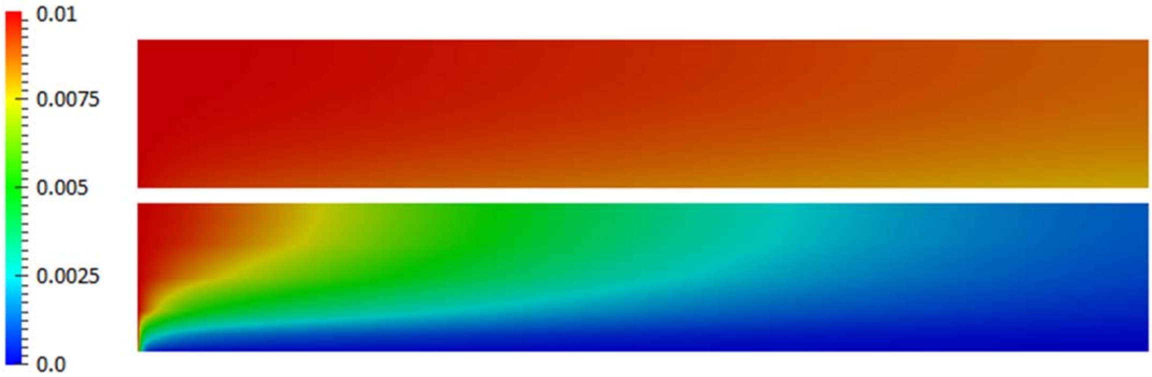

Figure 4.4. O_2 mole fraction profiles at 423.15 K and 773.15 K.

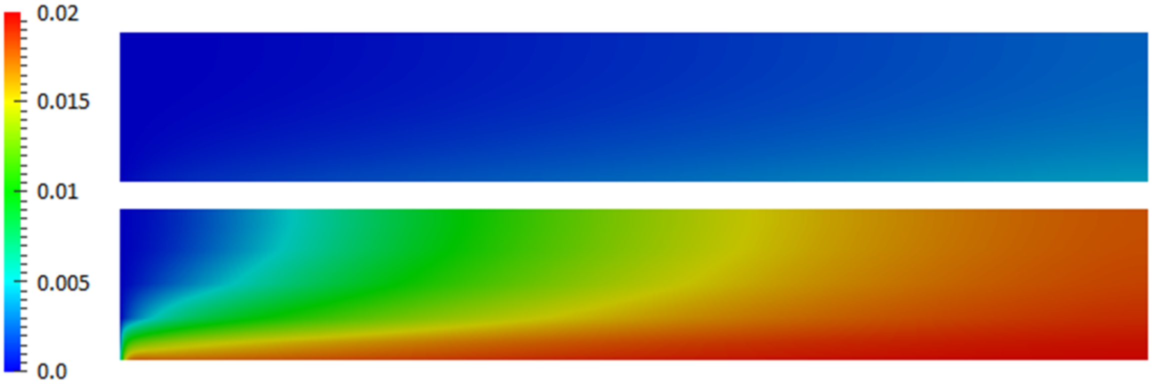

Figure 4.5. H_2O mole fraction profiles at 423.15 K and 773.15 K.

The simulation results show the amount of O_2 increase in the radial direction. This is an evidence of the reactions occurring at the catalytic surface. At 773.15 K the conversion of O_2 is fairly complete. It noticeable that near the catalyst, in the first 0.3 mm more than the 90% of the available O_2 is consumed. The trend of the water molar fraction is opposite to that of O_2. The production of H_2O is considerably lower in case of low temperature.

In Figure 4.6 the axial O_2 profiles sampled at different radial positions are presented, the first at 423.15 K and the second at 773.15 K. From Figure 4.6 it is observable that in the first part of the reactor there is an abrupt consumption of O_2.

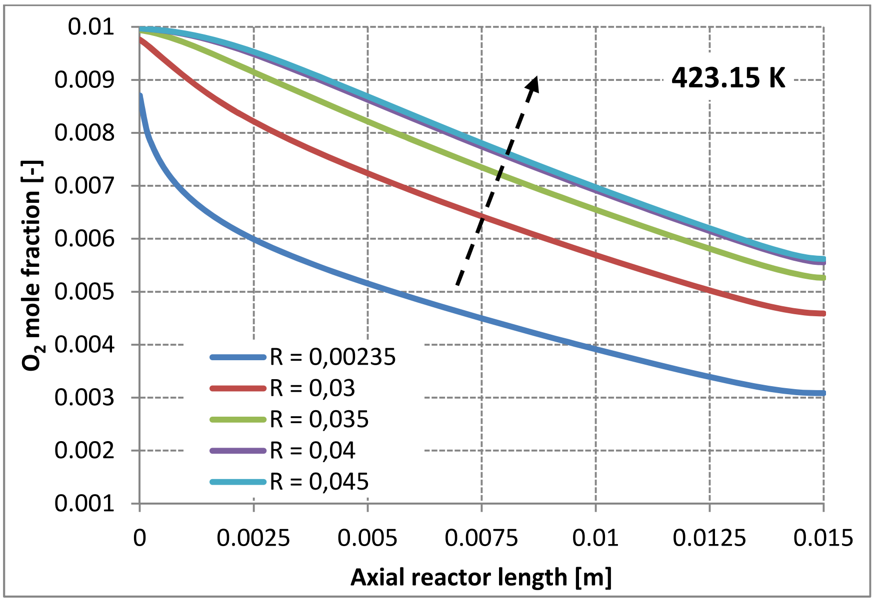

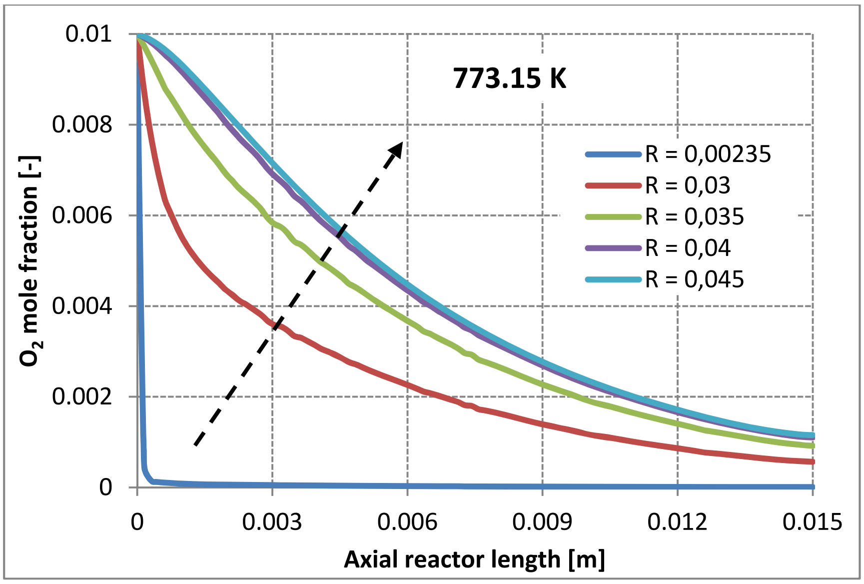

Figure 4.6. O_2 mole fraction profiles vs. axial length at 423.15 K and 773.15 K.

In Figure 4.7 a rapid production of H_2O is shown along the axial coordinate.

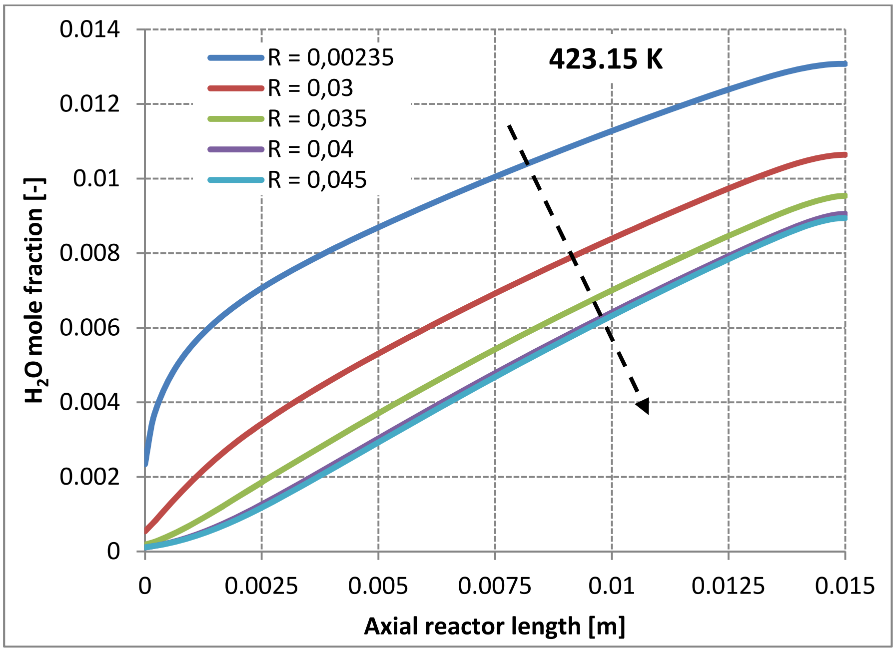

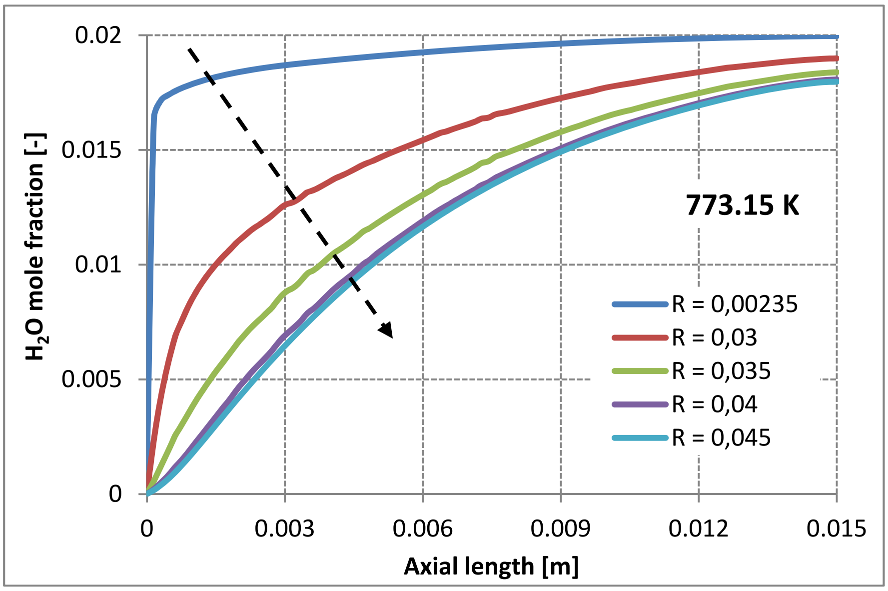

Figure 4.7. H_2O mole fraction profiles vs. axial length at 423.15 K and 773.15 K.

The nearer to the catalytic surface the profile is taken, the higher the conversion of the reactant is. It can be noticed that at 423.15 K the slope of the oxygen and water profiles in the axial direction is smaller than in the case of higher temperature. This highlights the limited reactivity at low temperatures.

In Figures 4.8 and 4.9 the radial profiles of the oxygen and water mole fractions are represented. The profiles are sampled along the radial coordinate at different axial length, at the temperatures of 423.15 K and 773.15 K.

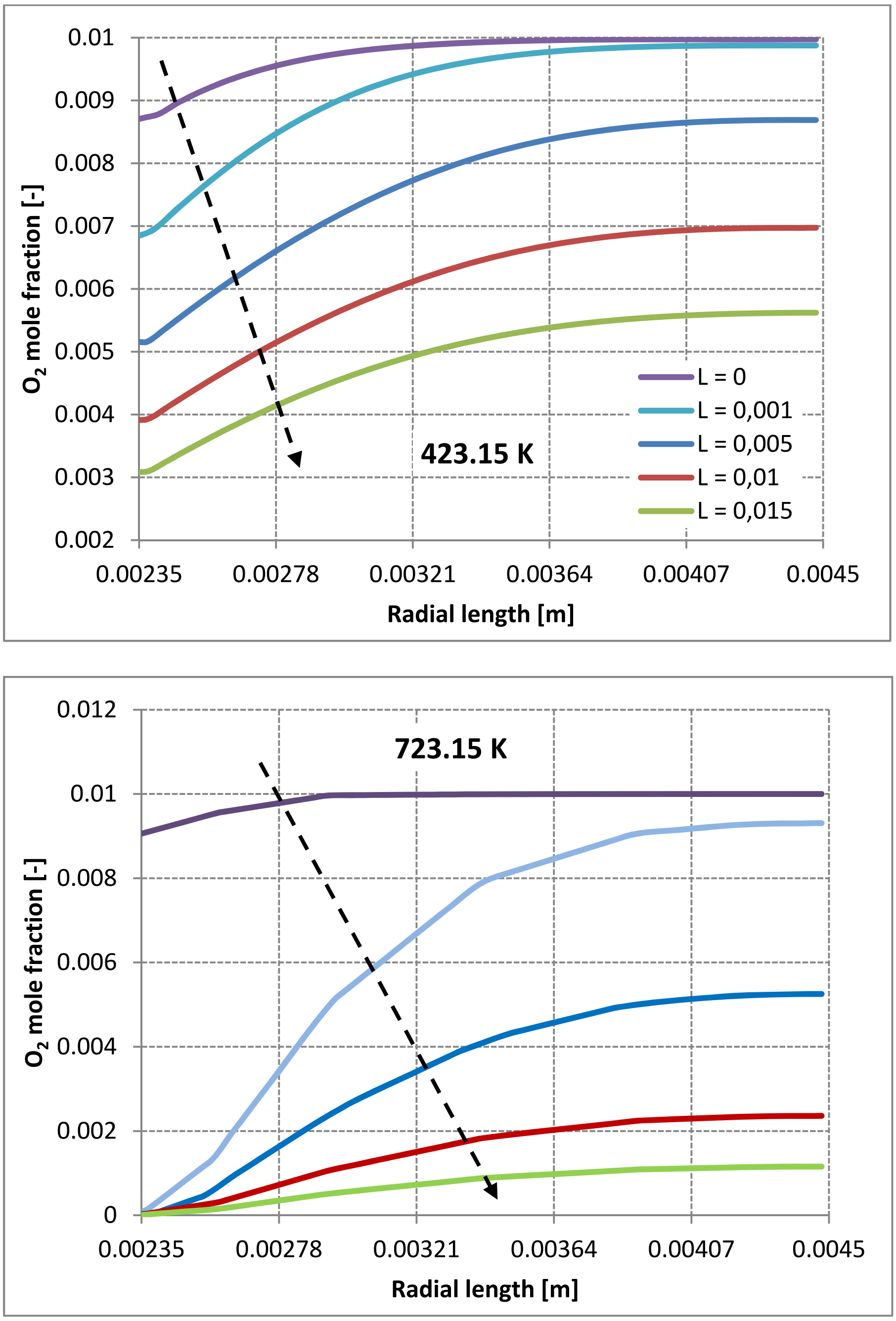

Figure 4.8. O_2 mole fraction profiles vs. radial length at 423.15 K and 773.15 K.

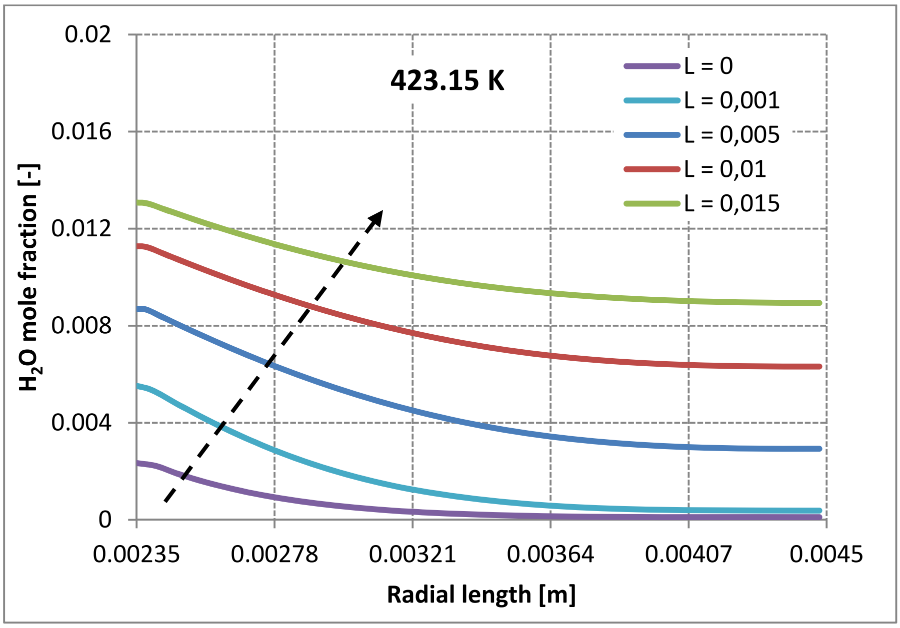

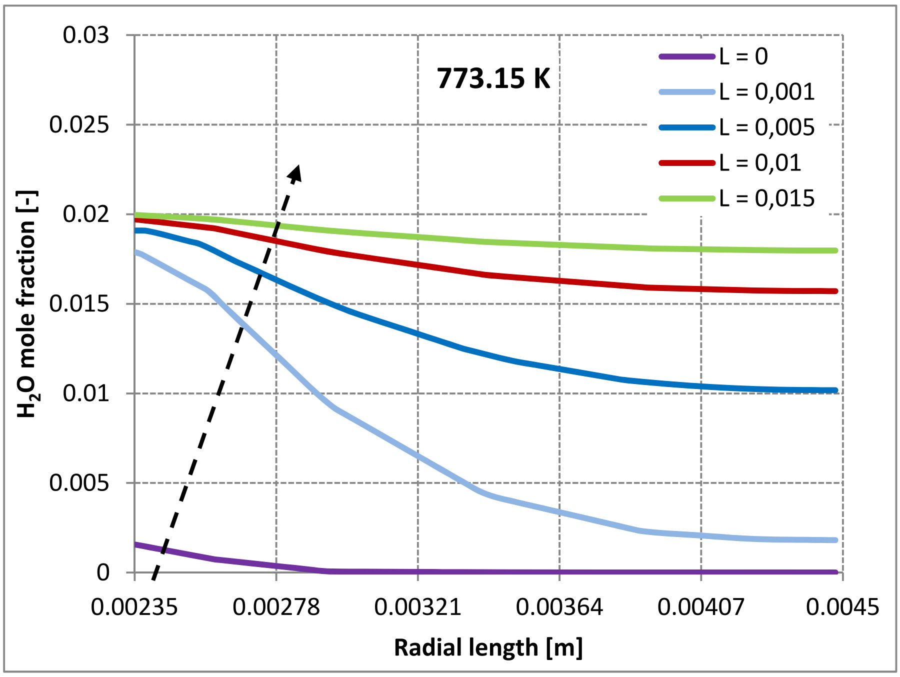

Figure 4.9. H_2O mole fraction vs. radial length profiles at 423, 15 K and 773,15 K.

The slope of the curves decreases going from the inlet to the outlet of the reactor. This trend underlines the high reactivity of the system in the very first millimeters of the reactor.

According to the heterogeneous kinetic model, the H* is the most abundant surface species, as shown in Figure 4.10, in which are depicted the profiles of the adsorbed species on the catalytic surface, at steady-state conditions. Water desorbs as soon as it is produced. The decrease of O* at 773,15 K is caused by the elevate conversion of the gaseous oxygen.

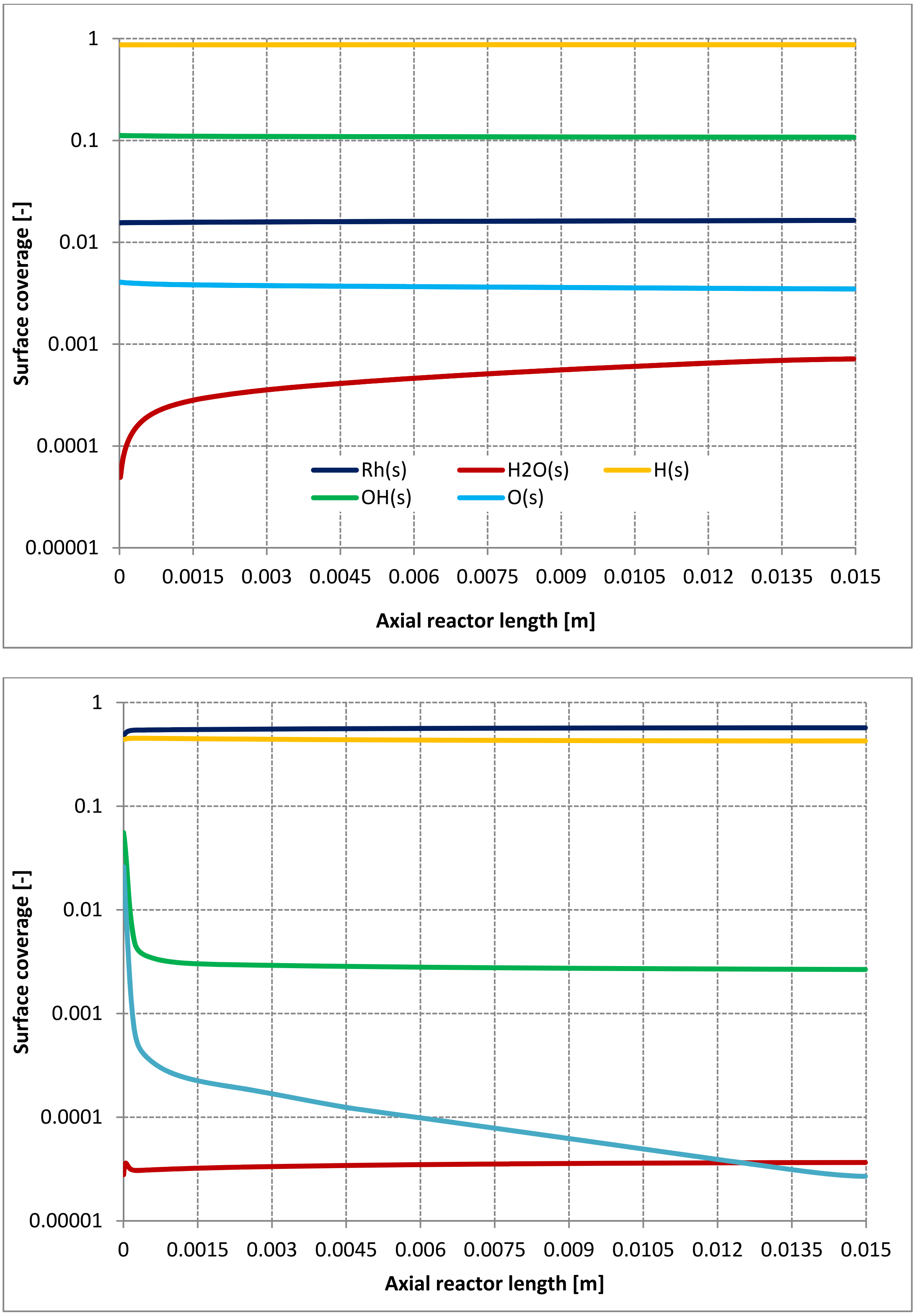

Figure 4.10. Adsorbed mole fraction vs. axial length profiles at 423.15 K and 773.15 K

The achievement of these results has been made possible after solving a series of problems. These regards the numerical nature of the problem and are discussed in the following.

4.2. Numerical issues

In a CFD simulation the spatial and temporal discretization is of primary importance. The finer these coordinates are discretized, the more accurate the solution is and the higher the computational time required is. In this view, it is crucial to identify the optimal values the achieve an accurate solution in the smallest amount of time.

The study is conducted on the case described previously. Specifically, the parameter adopted to compare the results is the oxygen conversion. The discretization of the radial and axial coordinates is taken into account. Furthermore, the effects of varying the temporal discretization are analyzed.

4.2.1. Axial number of cells

The first parameter analyzed is the number of cells in which the geometric domain is divided in the axial direction.

First of all it is necessary to highlight the wide differences in computational times between the different meshes. For example, dividing the control volume in twenty segments implies calculation times of the order of tens of seconds. Otherwise, with a detailed grid with 160 cells in the axial direction, the numerical simulation becomes highly computationally demanding and the final solution requires computational time of the order of 10^5 seconds.

To obtain an exhaustive set of data, two tests are performed: the first is operated at a temperature of 773.15 K, and the second is performed at 423.15 K. These two temperatures permit to check the solver performance in the diffusive regime in the first case and in the chemical regime for the second one.

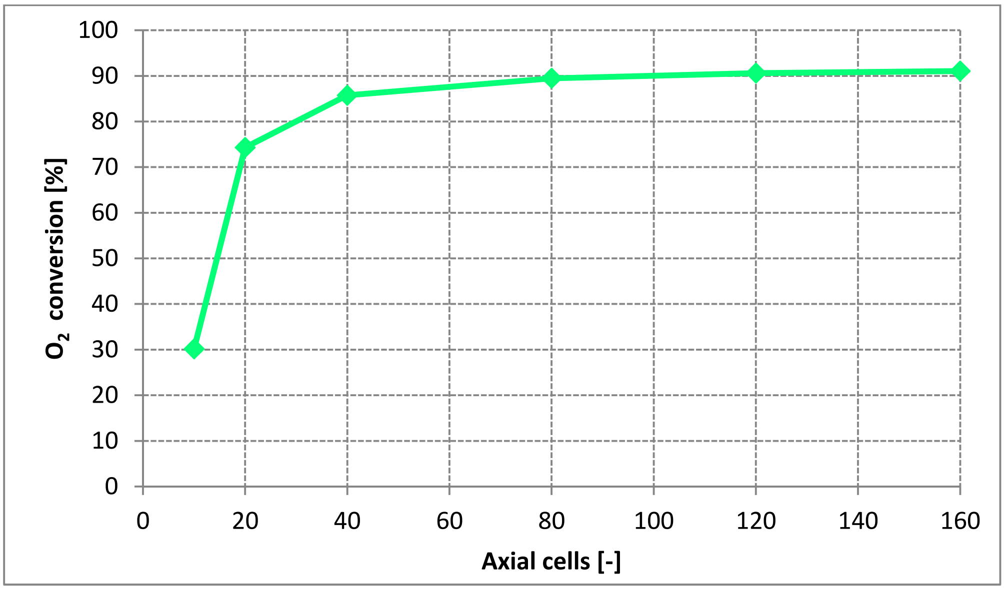

Figure 4.11. O_2 conversion vs. number of cells in axial direction at 773.15 K.

In Figure 4.11 the profiles of the O_2 conversion for different discretization of the geometrical domain along the axial coordinate are provided. It is possible to see that the number of axial cells is of primarily importance to obtain an accurate solution. Indeed, the result of the simulation performed at 20 cells is more than doubled than the result obtained at 10 cells. With a discretization of the mesh in the range of 120-160 cells, the oxygen conversion approaches convergence: the discrepancy between the values of these simulations is reduced to less than 1%.

From Figure 4.11 it can be noticed that the difference among the last two values is 0,48% and this means that the final solution is reached with an approximation inferior to 0,5%. Therefore, we can assume that in this case the accurate final solution can be achieved only using a mesh of 120 or more cells.

The second test is made by running the test case at a lower temperature of 423.15 K (Figure 4.12).

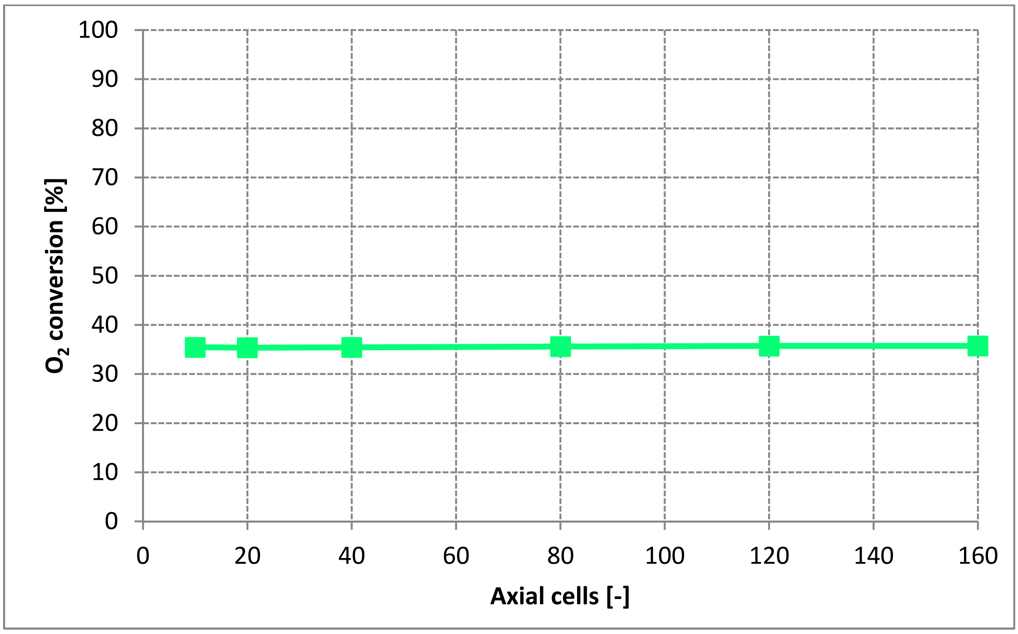

***Figure 4.12.** O_2 conversion vs. number of cells in axial direction at 423.15 K.*

At a lower temperature, we first have to notice that the final oxygen conversion reached in the reactor is inferior to the previous case because of the presence of the chemical regime. As shown in Figure 4.12, the value of conversion remain stable around the 35%. The comparison between the values obtained at different number of cells is smaller than 0.5%. This signifies that the convergence to the final result is reached with a very small error. In this test the loss of accuracy owed to the low discretization of the mesh is negligible. This is mainly due to the temperature of this simulation, that implies lower reaction rates compared to those at 773.15K.

From the previous analysis it is remarkable that the discretization of the axial coordinate has a strong impact on the final solution only at high temperatures. This behaviour can be linked to the surface activity of the catalyst. Indeed, the higher the temperature is, the faster the reactions are. This causes the system to be affected by strong variations in gas-species concentrations in the zone close to the catalyst wall. Moreover, at high temperature in the first millimeters of the reactor, a large conversion of reactants is achieved. This causes the creation of strong axial gradients. The more accurate the description of these gradients is, the more accurate the solution is.

The magnitude of these gradients directly depends on the system reactivity. It is important to investigate the accuracy of the solution for systems with different reactivity.

This can be achieved by varying the α_{cat} parameter. Indeed, it is an indicator of catalyst activity: the increasing of this parameter causes the reaction rate to grow. Further details on the calculation of this coefficient are provided in Chapter 2 and in Appendix A.

The analysis is accomplished by modifying the parameter with a factor of -50% to get an α_{cat} of 0.75 and +50% to get an α_{cat} of 3.0. Moreover the study is conducted at two different temperatures, 423.15 K and 773.15 K. In Figure 4.13 the results of the first test at 773.15 K are reported.

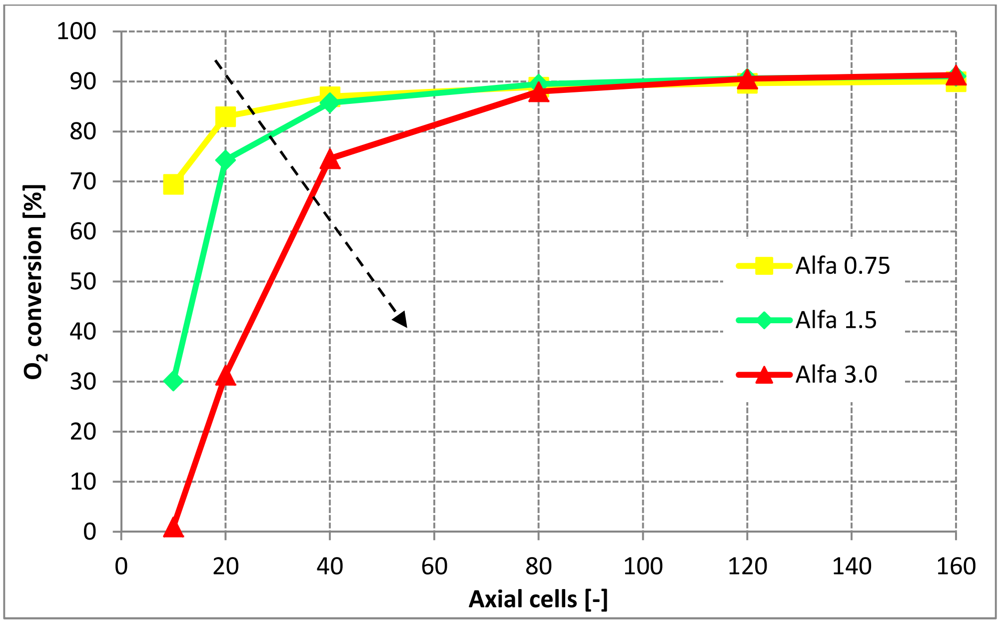

Figure 4.13. O_2 conversion vs. number of axial cells at different value of α_{cat} at 773.15 K.

The trend of oxygen conversion with respect to the number of cells along the axial coordinate shows an interesting effect. Since at the considered temperature the system is in diffusive regime, it is expected that the oxygen conversion does not depend on the catalyst activity. Moreover, one would expect that the higher the reactivity of the system is, the faster the convergence to the final value is reached. The observed behaviour of the system is completely different.

The description obtained by adopting a low number of cells in the axial direction is unfeasible. In fact the final value of conversion should be the same for all the three profiles. On the contrary, the results obtained shown an evident discrepancy between the final oxygen conversions. By rising the number of axial cells, the three lines collapse to the convergence value. As a consequence the system requires at least 120 cells to approach the experimental value.

The explanation of this behaviour is linked to the presence of fast reactions caused by high catalytic activity. This implies the occurrence of strong gradients in the axial direction which require accurate descriptions.

In Figure 4.14, the axial profiles of oxygen mole fraction for different mesh discretization ns along the axial direction are shown. It is possible to see that only with the highest numbers of cells the trend is accurately described.

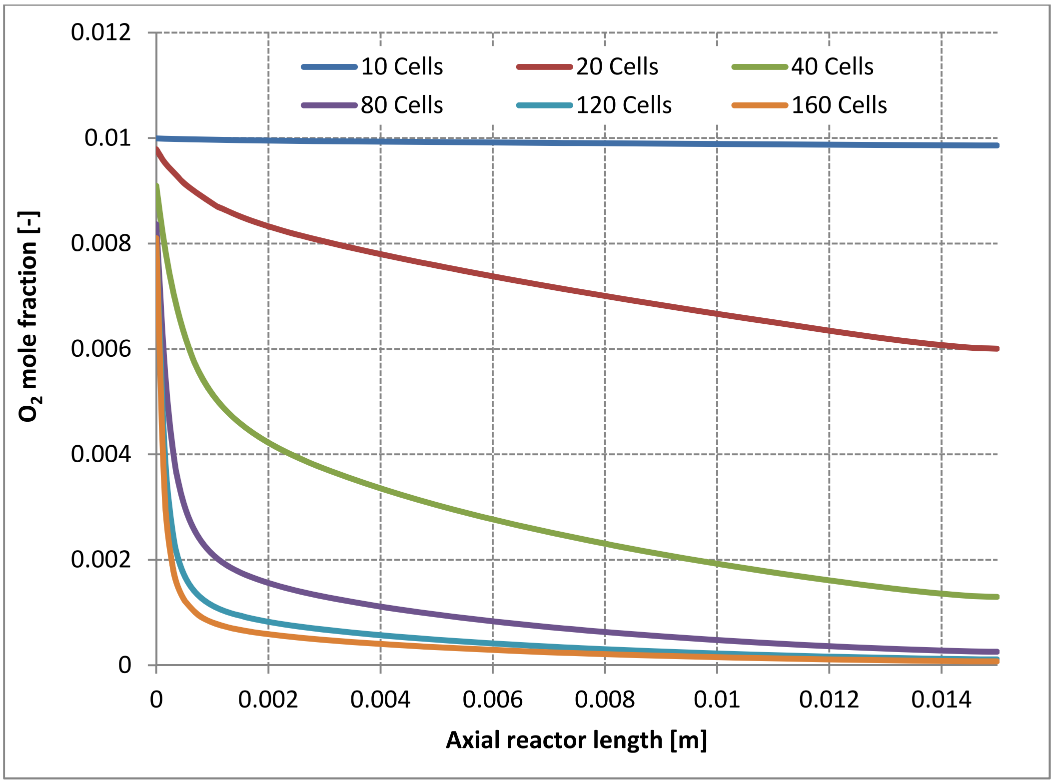

Figure 4.14. O_2 mole fraction profiles vs. number of axial cells at α_{cat}=3.0 and 773.15 K.

The analysis proceeds by repeating the test at low temperature conditions (423.15 K). The Figure 4.14 shows the trends of the conversion of the reactants with the rising of the axial cells number.

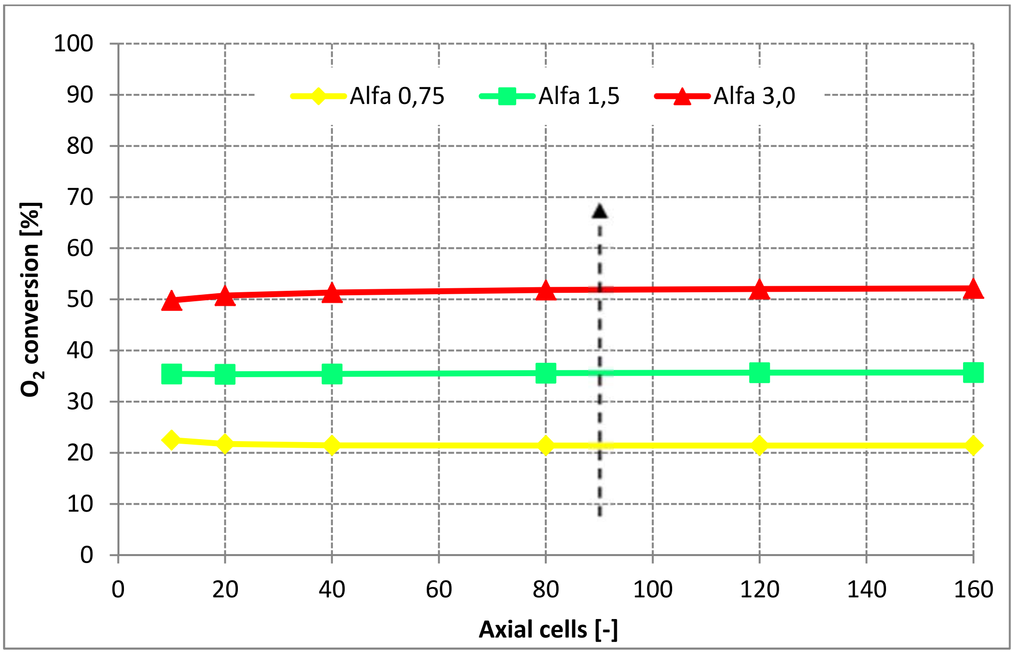

Figure 4.15. O_2 conversion vs. number of axial cells at different value of α_{cat} at 423.15 K.

For the considered temperature the system is under chemical regime, and thus the final oxygen conversion strongly depends on the catalytic activity. Specifically one expects the conversion to rise if the catalytic activity is increased. This behaviour is well depicted in Figure 4.15.

Furthermore, from Figure 4.16 it is evident that the moderate reaction rate limits the magnitude of the gradient: this results in an accurate solution even on meshes with a small number of cells.

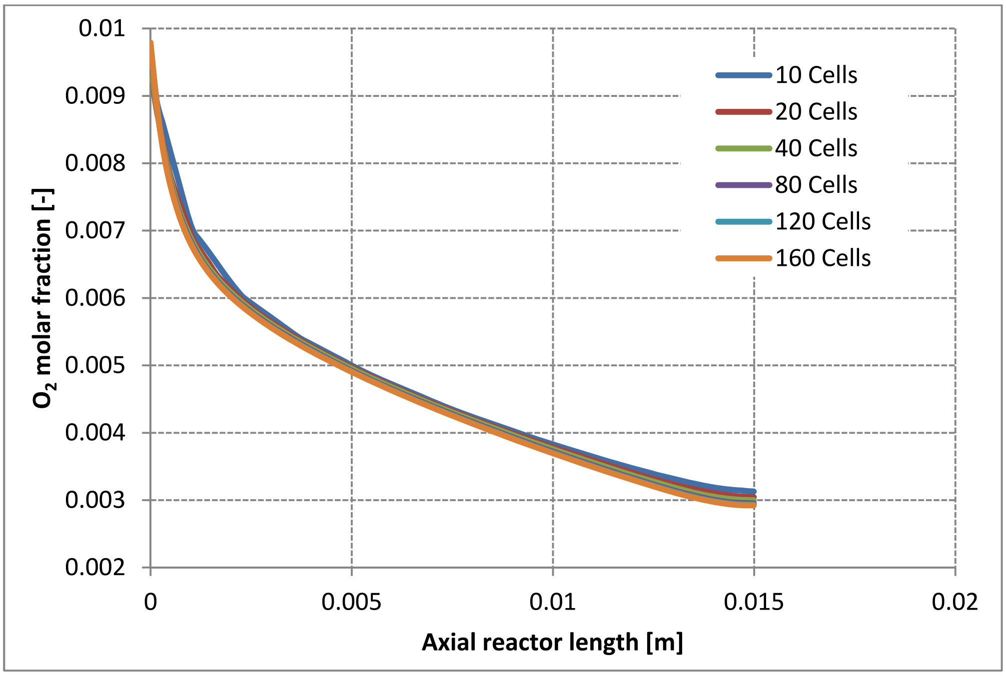

Figure 4.16. O_2 mole fraction profiles vs. number of axial cells at α_{cat}=3.0 and 423,15 K.

Finally, by considering the previous sensitivity analysis conducted on the number of cells in the axial coordination, the optimized value for the axial number of segments turns now to be 160 and necessarily never under 120. An higher discretization is not strictly necessary and even inconvenient, because the computational costs rise but the accuracy of the final solution cannot be improved.

4.2.2. Radial number of cells

Beside the analysis of the axial coordinate, numerical tests on the number of cells in the radial direction have been performed. The operating conditions at which the test is performed are the same of the axial convergence tests. In Figure 4.17 the oxygen conversion is plotted respect to the number of segments in the radial direction. The simulation is performed at the temperature of 773.15 K.

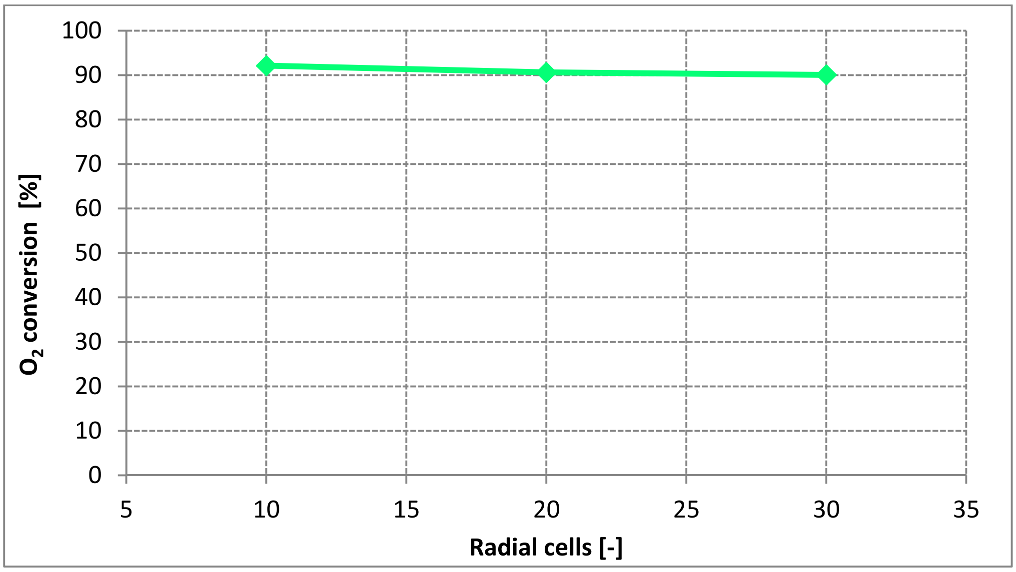

Figure 4.17. O_2 conversion vs. number of cells in axial direction at 773.15 K.

As we can see in Figure 4.17, the conversion preserves a stable value around 91%. The differences between the second and third value remains inferior to 1% and the accurate solution is reached. In this case it is noticeable that the effect of the discretization in the radial direction has a lower influence on the accuracy of the final solution with respect to the number of axial cells.

An analogue observation can be done by analyzing the Figure 4.18, that shows the conversion of oxygen at 423.15 K.

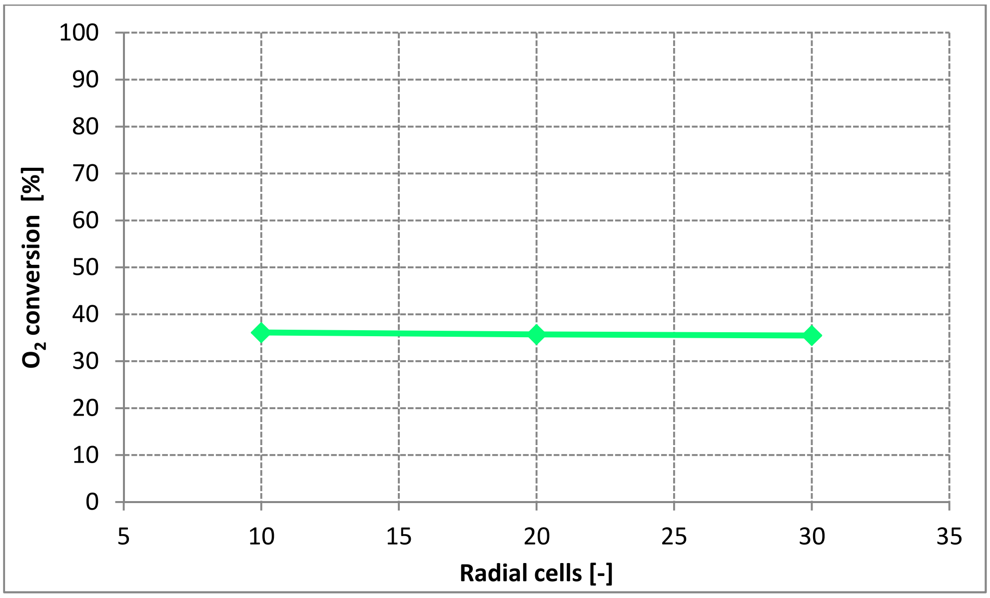

Figure 4.18. O_2 conversion vs. number of cells in axial direction at 423.15 K.

As shown in Figure 4.18 the variation between the different solutions is almost negligible: this proves the fact that at lower temperatures a minor number of cells is required. Concluding, we can consider that, for the simulation of the considered system, the best value for number of radial segments is around 20.

In analogy with the convergence tests focused on the axial coordinate, the effects of the reactivity of the system have been investigated for the radial direction. In Figure 4.19 simulations at different catalytic activities at 773.15 K are reported.

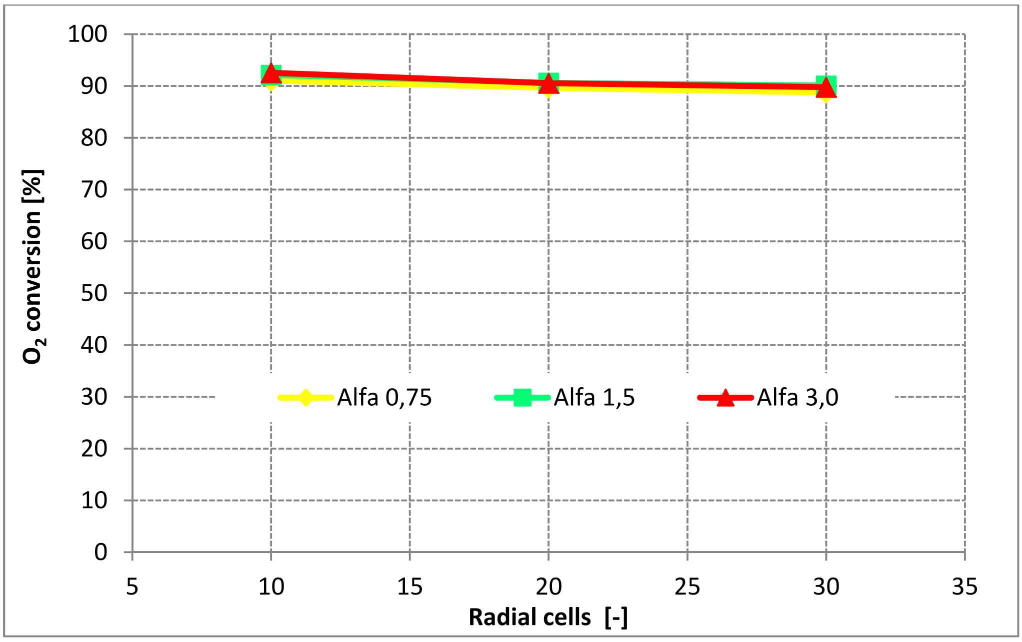

Figure 4.19. O_2 conversion vs. number of radial cells at different value of α_{cat} at 773.15 K.

As previously seen, the results are quite insensitive to the number of cells in the radial direction. The same conclusion can be drawn taking into account Figure 4.20.

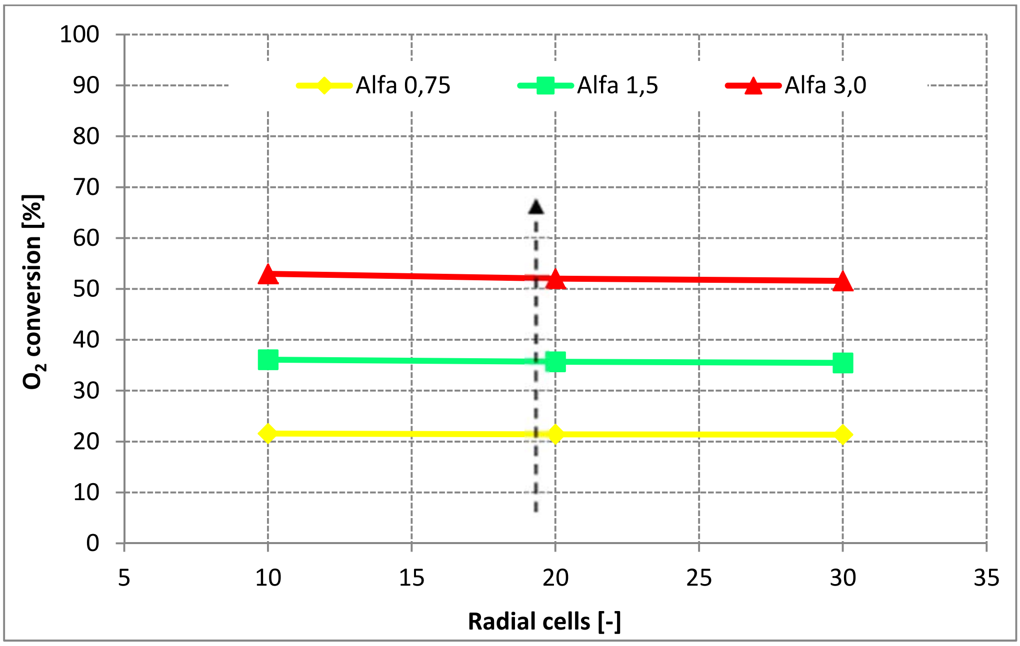

Figure 4.20. O_2 conversion vs. number of radial cells at different value of α_{cat} at 423.15 K.

As observable in Figure 4.19 and 4.20 the final solution is weakly influenced by the number of cells in the radial direction.

4.2.3. Chemical vs. diffusive regime

In order to confirm the previous analysis, we provide a further test: the catalytic activity is varied in order investigate the range of operating conditions in which our solver reaches the convergence. The comparison between different simulations is made by considering that in chemical regime the conversion has to grow if the activity increase. On the contrary, when the system is under diffusive regime the results are not sensitive to variations of the catalytic activity, expressed by α_{cat}.

In Figure 4.21 the variations of the oxygen conversion over different values of α_{cat} at 423.15 K and 773. 15 K are reported.

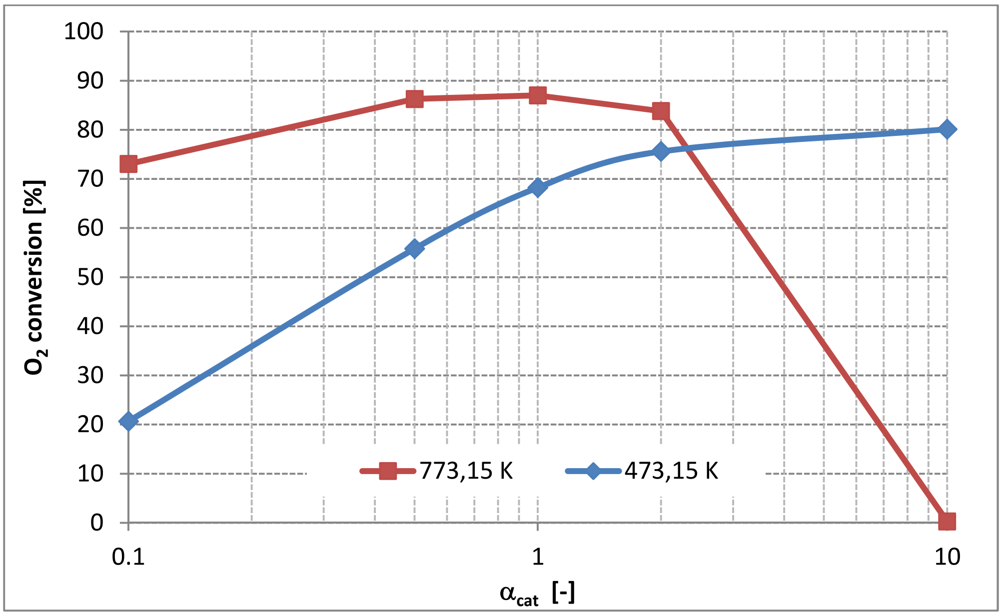

Figure 4.21. O_2 conversion vs. α_{cat} at different temperature.

Let us consider the blue line, which indicates the oxygen conversions obtained by varying the catalytic activity when the system is in diffusive regime. It is evident that to a rising of α_{cat} corresponds an increase of the final conversion: simulations manage to capture the expected behaviour of the system.

Instead, if the red line is taken into account, the results are not satisfying. At the higher temperature of 773.15 K the establishment of the diffusive regime can be observed at values of the α_{cat} of about 0.75. Even if the system is controlled by mass transfer phenomena, the final results achieved with the highest catalytic activity stress out that convergence is definitely not reached.

In Figure 4.22 the axial profiles of the oxygen mole fraction is represented. The data are gathered near the catalytic surface.

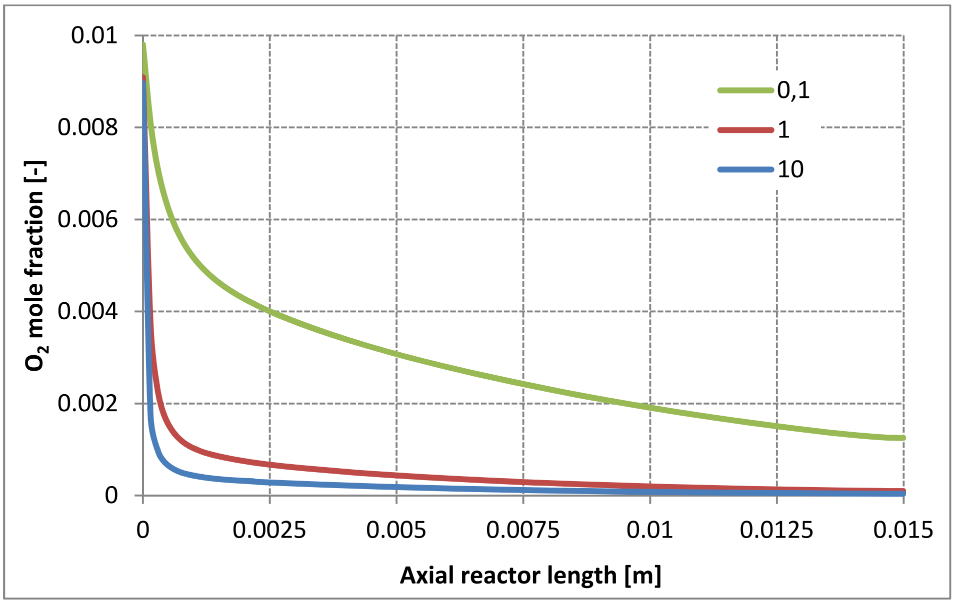

Figure 4.22.O_2 molar fraction vs. axial length at different α_{cat} .

From Figure 4.22 it is possible to notice that the higher the reactivity of the system is, the more elevate the initial slope of the curves is. The elevate magnitude of the gradients implies the use of a better and more detailed mesh.

From Figure 4.23 it can be noticed that the increase in the number of axial cells improves the accuracy of the solution even at low catalytic activities. The main conclusion that can be drawn is that by increasing the refinement of the mesh, the solver acquires the ability to describe the system even in zones where the reactivity is very high. Specifically, for an α_{cat} value of 10 the correct behaviour is described only using 640 axial cells.

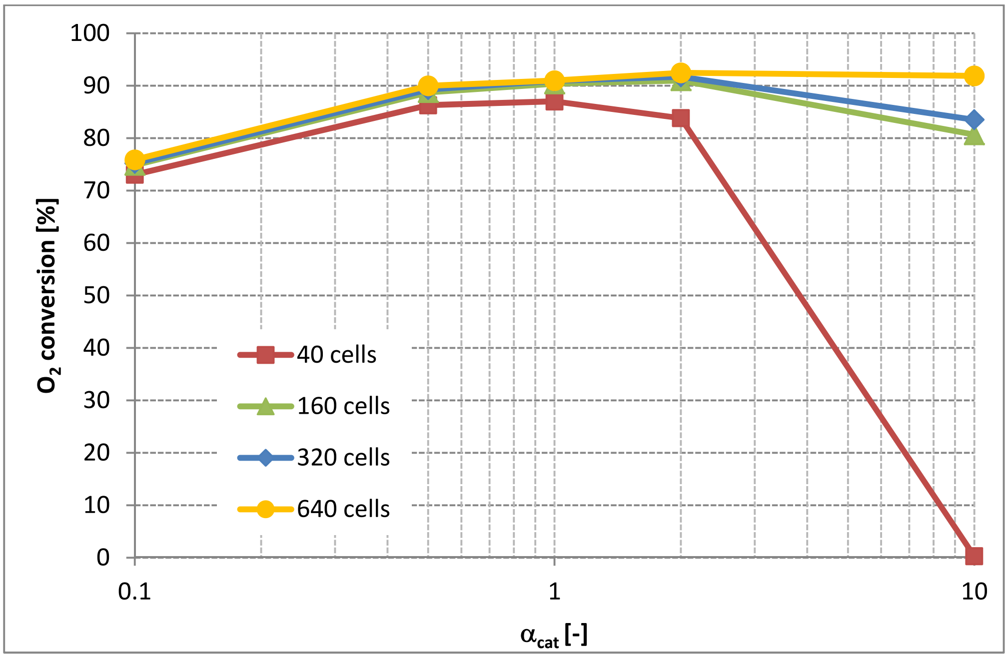

Figure 4.23. O_2 conversion vs. α_{cat} at 773.15 K.

On the basis of the previous studies we can conclude that the reactivity of the system is a parameter of primary importance. The simulation of systems with high conversions of reactants caused either by high temperatures or elevate catalytic activities has to be achieved with well detailed meshes.

4.3. Time step

In the previous section, the effects of the spatial discretization have been studied. Now we present another analysis about the sensitivity of the final solution to the time discretization.

The aim of the analysis is to obtain the optimized time step for the integration. The smaller the time step is, the more accurate the description of the dynamic behaviour of the system is. Anyway the computational time required for the single simulation increases. It is then necessary to find out the threshold value beyond which strong decreases of the temporal step generates negligible improvement in the solution accuracy.

In a CFD simulation the magnitude of the time step has a strong dependence on the system considered. As an example, let us consider the case of section 4.1: the annular reactor has a length of 1.5 cm and an outer diameter of 0.45 cm. Depending on the temperature, the inlet velocity varies in the axial direction in a range of 0.5 – 2 m/s. This means that the mean residence time, i.e. the mean time required for a fluid particle to get through the reactor, is in the order of tens of milliseconds. In order to properly describe the behaviour of the system, the time step required has to be inferior to the residence time. It is noticeable that with an higher flow rate, the mean residence time decreases. Thus, to achieve an accurate solution, a smaller time step is required.

Consequently, it is necessary to identify a general formula for the calculation of the time step needed to reach a reliable solution. Let us consider a generic domain discretized in a number of cells. The necessary condition required to correctly describe the behaviour of the system is that the dynamic of each cell is well defined. As previously said, the mean residence time in the cell has to be higher than the time step in the cell.

$$\delta t < \frac{\delta x}{|U|} = t_{residence} \tag{4.2}$$

where δt is the time step, $|U|$ is the magnitude of the velocity through the cell and δx is the cell size in the direction of the velocity.

It is then possible to introduce the dimensionless Courant number, defined as:

$$Co = \frac{\delta t|U|}{\delta x} \tag{4.3}$$

As a consequence of Eq. 4.2, the Courant number has to be inferior to 1 for each cell of the mesh. It is then convenient to keep the Courant value constant and compute the time step taking into account the cell with the smallest residence time.

For non-reacting fluid dynamic problems it is sufficient to maintain the Courant value inferior to 1. According to (Oran and Boris 2001) for the numerical simulation of reactive flows, a Courant number inferior to 0.5 is required.

Since the time step is calculated by Eq. 4.1, the lower the Courant number is, the higher the accuracy reached during the simulation is and the longer will take the solver to reach convergence.

4.3.1. Effect of Courant number

In order to analyze the effect of varying the temporal step on the final solution, we considered 3 values of the Courant number: 0.075, 0.1 and 0.25. The discretization of the mesh is obtain by using the optimized values: 200 axial cells and 30 radial cells. The study proceeds by analyzing the behaviour of the system both in mass transfer controlled regime and chemical regime.

The following plots report the profile of hydrogen and water mole fractions over the reactor length. The profiles are sampled near the catalytic surface.

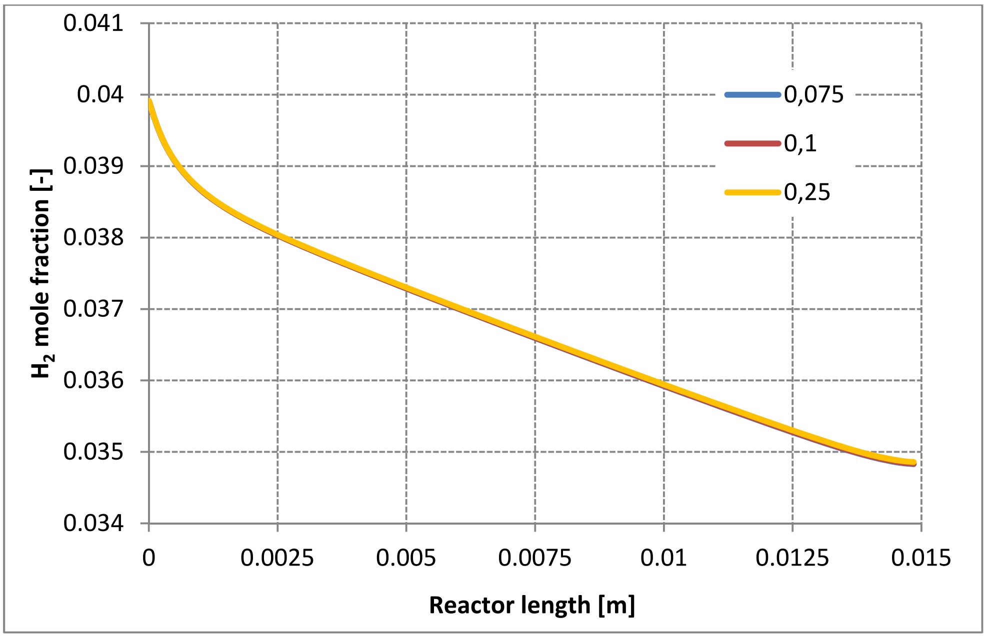

Figure 4.24. H_2 mole fraction profiles vs. reactor length at 423.15 K.

The first tests were performed at a temperature of 423.15 K. This implies that the system is in chemical controlled regime. As consequence, it possible to see in Figure 4.24 that at this low temperature the rate of hydrogen consumption is moderate. Furthermore, the same profile is obtained for three different Courant numbers. This indicates that at low reaction rates, the accuracy of the description of the system is reached even with high Courant values. In fact, though the time step rises with the increase of the Courant number, the steady-state solution is as well properly identified.

The profile of H_2O is reported in Figure 4.25 As previously noticed, the profile description is accurate for all the Courant as a consequence of the chemical regime. Also in this case, the profiles are gathered near the catalytic wall.

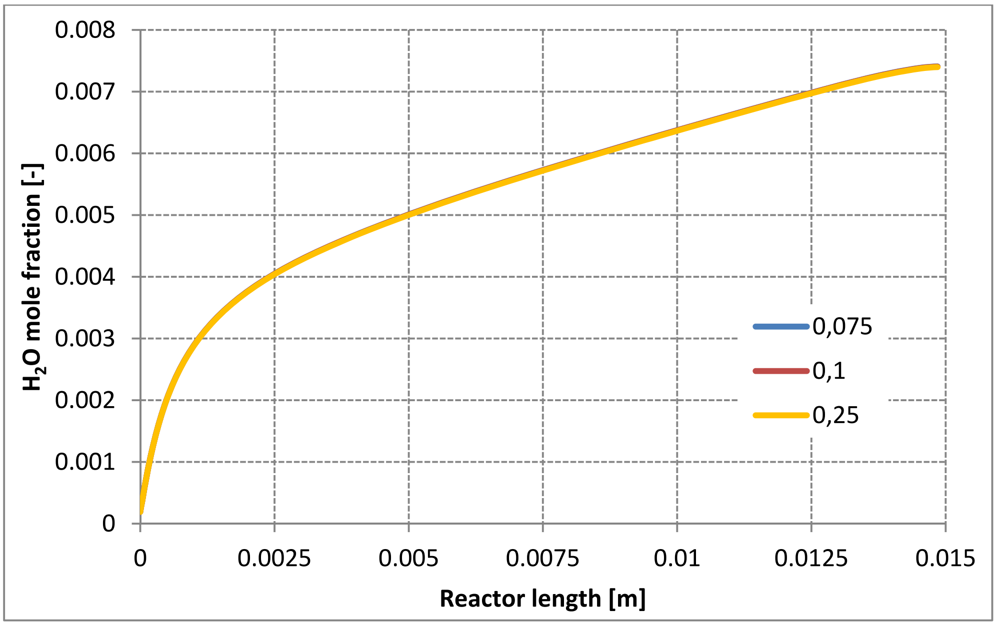

Figure 4.25. H_2O mole fraction vs. reactor length at 423.15 K.

On the contrast, at temperatures higher than 573.15 K the reactor is under diffusive control. In the following figures the profile of H_2 and H_2O mole fraction along the axial coordinate of the reactor are reported by varying the Courant value.

In Figure 4.26 the H_2 profile at the temperature of 773.15 K is presented. It is important to note that the description of the reactant profile is more accurate for values lower than 0.1. The most accurate solution among the curves presented is obtained at 0.075 because with a lower Courant number, the time step width decrease and the solution becomes more accurate. In order to highlight these trends, the thickness of profiles at lower Courant number has been increased.

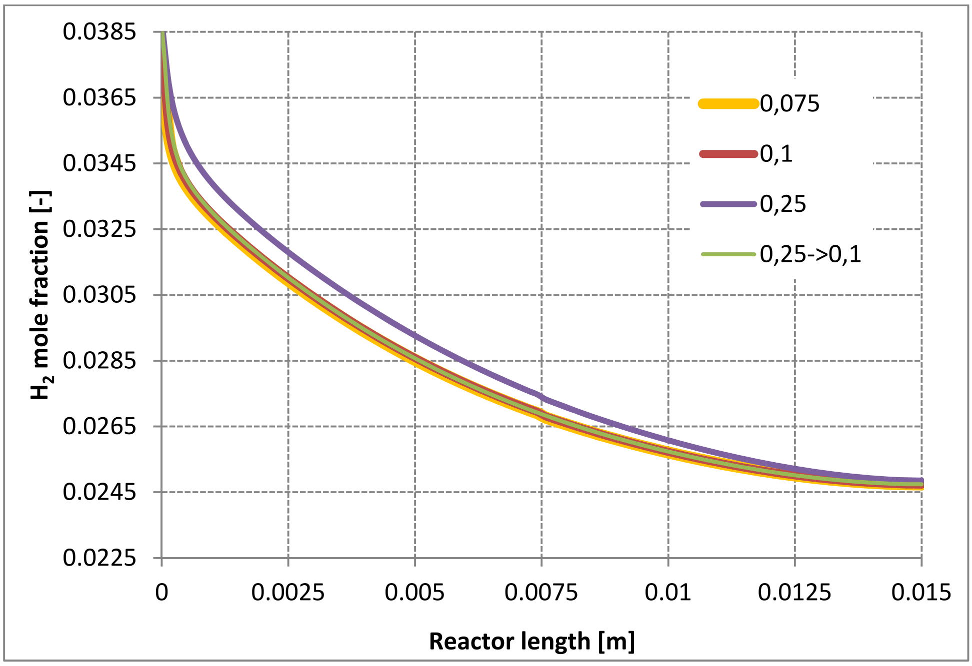

Figure 4.26. H_2 mole fraction profiles vs. reactor length at 773,15 K.

From Figure 4.26 it can be noticed that the profile obtained with a Courant number of 0.25 gives an inaccurate description of the H_2 molar fraction. If during the simulation the Courant number is lowered at 0.1 the solution to convergence is achieved.

The reasons of this behaviour is related to the numerical scheme of solution. To explain this trend the following hypothesis has been considered. When the system is under chemical regime, the composition is controlled by the kinetic of reactions. Since reaction and transport are solved coupled, we expect that the solution is independent from the time step adopted. Instead, since in the diffusive regime the system is entirely controlled by fluid dynamics, the convective and diffusive terms are dominant. These are computed with a segregated approach, i.e. each equation is solved decoupled. This method introduces an error which becomes evident when the time step increases.

The same conclusions can be obtained by examining the profiles of the product over the reactor length, as shown in Figure 4.27. Indeed, the same behaviour is observed.

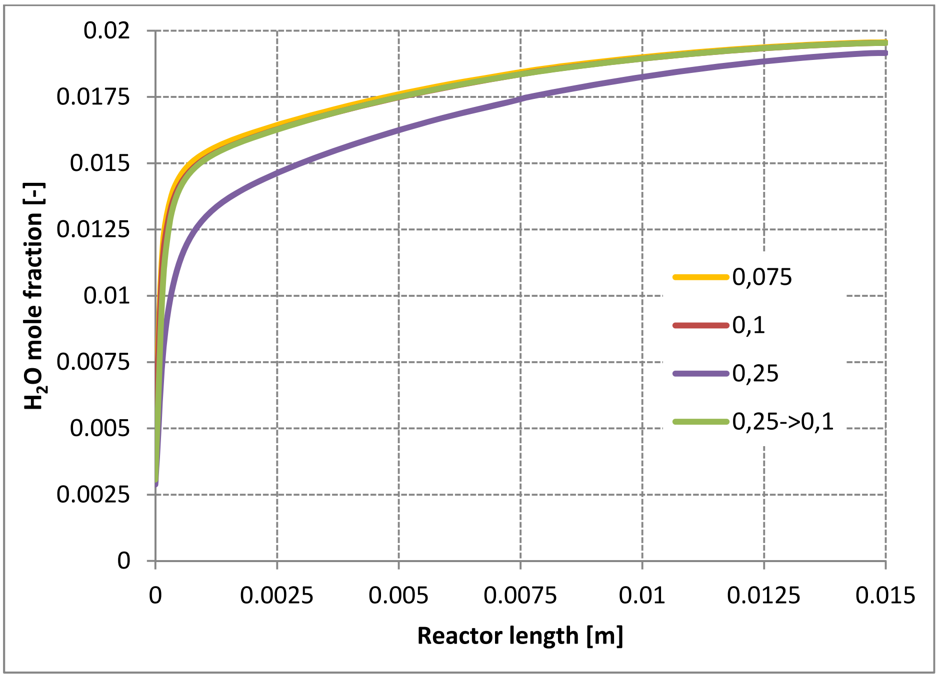

Figure 4.27. H_2O fraction vs. reactor length at 773,15 K.

In the next section, the effect of the variation of the Courant number over the time required to complete a numerical simulation is investigated.

4.4. Execution and clock time

A sensitive analysis has been conducted by studying the computational time required to complete the numerical simulation while varying the Courant number. The analysis regards two time parameters:

- ✓ *Execution time or CPU time*, is the is the actual time taken by a elaboration unit to complete a task.
- ✓ *Clock time or wall time*, measures the total time for the process to complete. In contrast to CPU time, which measures only the time during which the processor is actively working on a certain task, clock time measures the total time for the process to complete. It is the sum of three terms: CPU time, I/O time, and the communication channel delay.

The difference between the CPU time and the wall time consists of time that passes due to programmed delays or waiting for resources to become available. This implies that the clock time is always higher than the execution time in all the cases simulated. It is possible to see this feature in Figure 4.28.

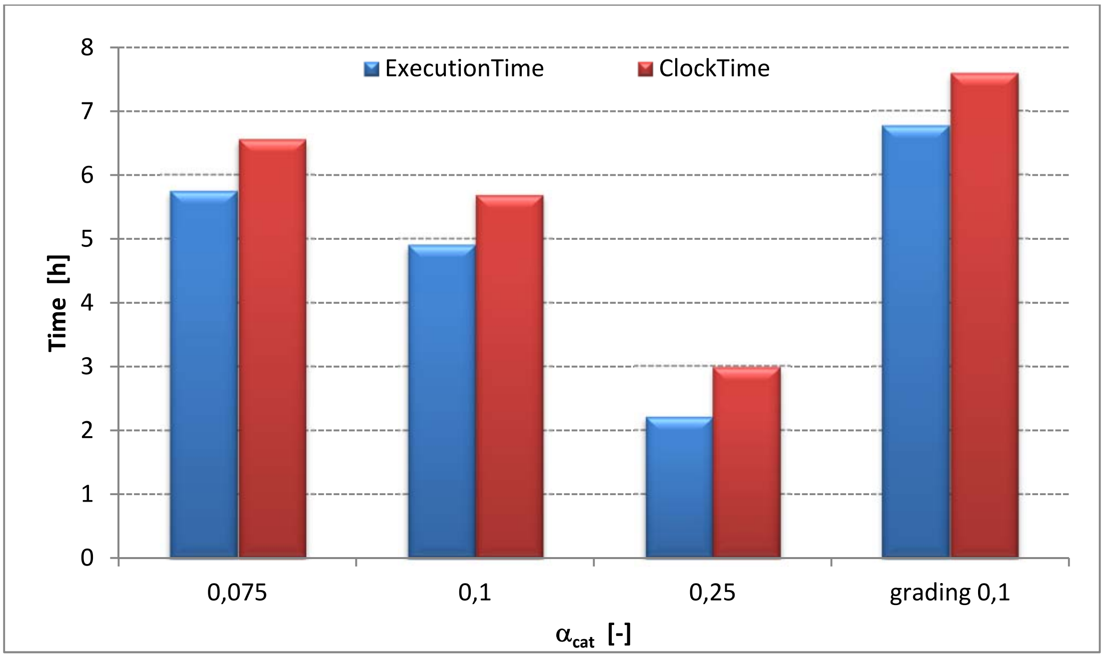

Figure 4.28. Execution time and clock time at different Courant and different mesh grading.

The decrease of the value of the Courant number coincides with a decrease of the time step needed for the simulation of the single cell. This results in the rising of the computational costs required for the numerical solution. As shown in Figure 4.21, it can be notice that the Courant is inversely proportional to the time needed to achieve convergence. Indeed, the simulation performed with the smaller Courant number (0.075) requires an execution that is 2.6 times higher. The optimized value for the this parameter is assumed as 0.1, because it will generate an accurate solution without an enormous request of computational costs.

As previously said in section 4.2, the grading has been considered in performing these simulations. Accordingly to the optimized value of Courant number, the effect on the computational time due to the grading of the mesh is evaluated. In Figure 4.21 it is shown the increase of execution and clock time generated by the refining of the mesh. In this case the execution is accomplished in 1.4 times then the test without grading. The reason of this behaviour is that the mesh grading reduces the minimum width of the cell and thus the time step decreases.

Chapter 5.

Experimental validations

In this chapter we present a validation of the catalyticFOAM solver. A comparison between the numerical results and the experimental data is provided. Furthermore, a study of the transitory behaviour of this system is given in 5.2.2.

5.1. Introduction

In the previous chapter several numerical tests have been performed on catalyticFOAM. The main numerical issues have been investigated and this has led to the achievement of the convergence values of the final solution. In order to validate the reliability of the tool, it is now necessary to test its predictive ability.

The analysis is performed by simulating a catalytic system whose behaviour has been well described in the literature. In order to accurately capture experimental data, a reliable and proved kinetic scheme is adopted.

The case test presented in this chapter concerns the H_2 combustion over Rh catalyst presented in (Maestri, Beretta et al. 2008).

5.2. H_2 combustion over Rh catalyst

The case considered treats the fuel-rich H_2 combustion over Rh catalyst in an annular isothermal reactor. The simulations have been conducted by using the UBI-QEP kinetic scheme provided in Appendix C. Experimental validations of this reaction mechanism are provided in (Maestri, Vlachos et al. 2009).

5.2.1. Comparison with experimental data

In this section the results of a series of isothermal simulations are presented. In Figure 5.1 the measured and calculated conversions of O_2 over temperature at a flow rate of 0.274 Nl/min are reported. The operating conditions are provided in Table 4.1.

Due to the cylindrical symmetry of the annulus reactor, the simulation can be performed over a 2D domain. This geometrical domain is dived in 250 segments in the axial direction and in 24 segments in the radial coordinate, for a total amount of 6000 cells.

Operating conditions	
Inner radius	0.235 cm
Outer radius	0.450 cm
Reactor length	1.5 cm
O_2 mole fraction	0.04 (-)
H_2 mole fraction	0.01 (-)
N_2 mole fraction	0.95 (-)
Pressure	1atm

Table 4.1. Simulation parameters.

The implicit Euler method was applied the temporal discretization. For the spatial coordinates a Gauss upwind scheme is employed.

In the plots the red triangles are the experimental points. The blue line represents the obtained conversions of O_2 at different temperatures. The green lines depict the numerical simulation conducted in the article.

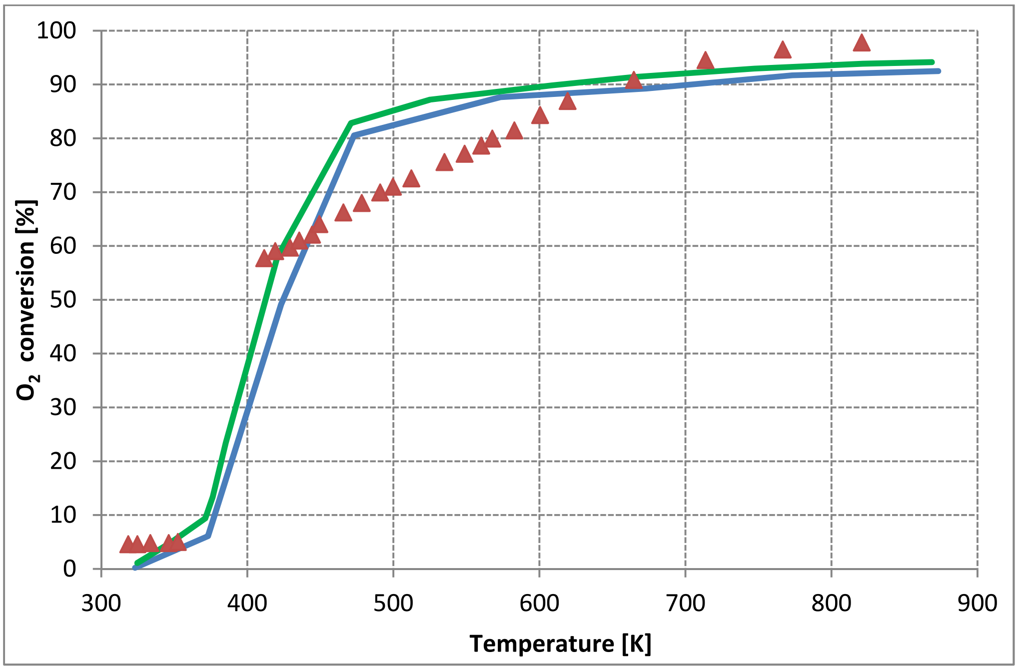

Figure 5.1. Conversion of O_2 vs. temperature at flow rate of 0.274 Nl/min.

The experimental data show that the combustion started at about 373.15 K with a very low conversion of O_2. Then there is a rapid increase of the conversion of O_2 in a narrow range of temperatures. By observing the axial gradient (Figure 4.6.a) it is possible to see that O_2 is present in elevate concentrations near the catalytic layer. Thus, in the temperature field between 373.15 K and 573.15 K the system is in chemical regime. By increasing the temperature, the slope of the conversion profile decreases till the reaching of a plateau because of the establishment of the external diffusive regime.

At this flow rate, the highest conversion is reached at about 773.15 K and is close to 100%. The same fast rise of conversion for the initial temperatures is obtained. Furthermore the model captures the trend to the plateau for the higher temperatures. The model overestimates the oxygen conversion at low temperatures and underestimates it at high temperatures. The reasons of these discrepancies are investigated in the following.

In the following plots a two-fold and four-fold increase of the flow rate is presented. Indeed the increase of the inlet velocity causes convective fluxes to grow at expenses of the diffusive flows. In Figure 5.2 the conversion profile for the flow rate of 0.548 Nl/min is presented.

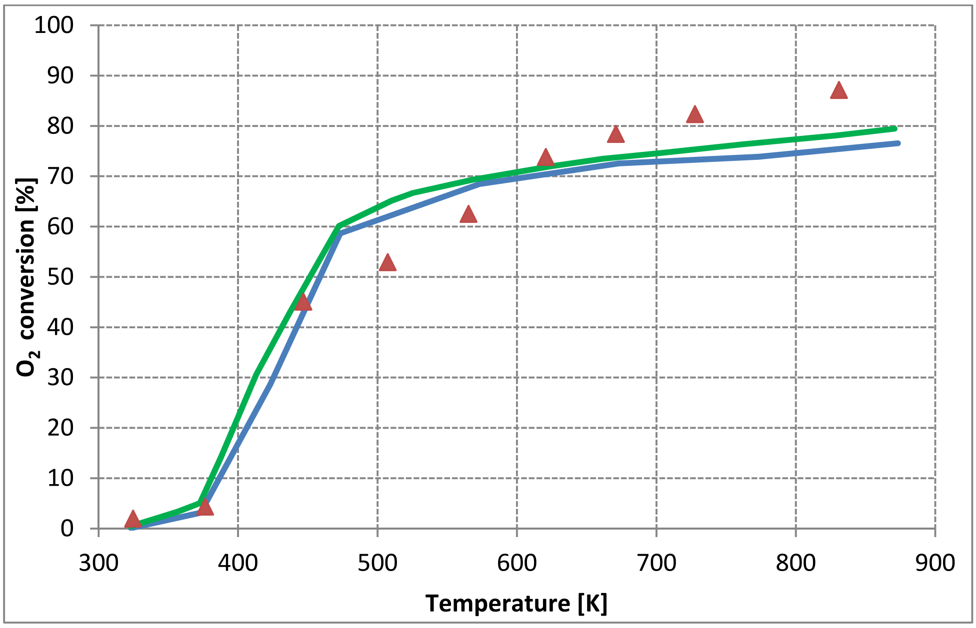

Figure 5.2. Conversion of O_2 vs. temperature at flow rate of 0.548 Nl/min.

As well as in Figure 5.1, the trend of conversion is detected with good accuracy. It is possible to notice that the conversion at 873.15 K is slightly lower than that of the previous case. This is related to the increment of the flow rate: in these conditions the fully external diffusive regime markedly limits the O_2 conversion. As in the cases with flow rates of 0.274 Nl/min and 0.548 Nl/min, it is possible to see the underestimation and overestimation zones in the two different temperature ranges.

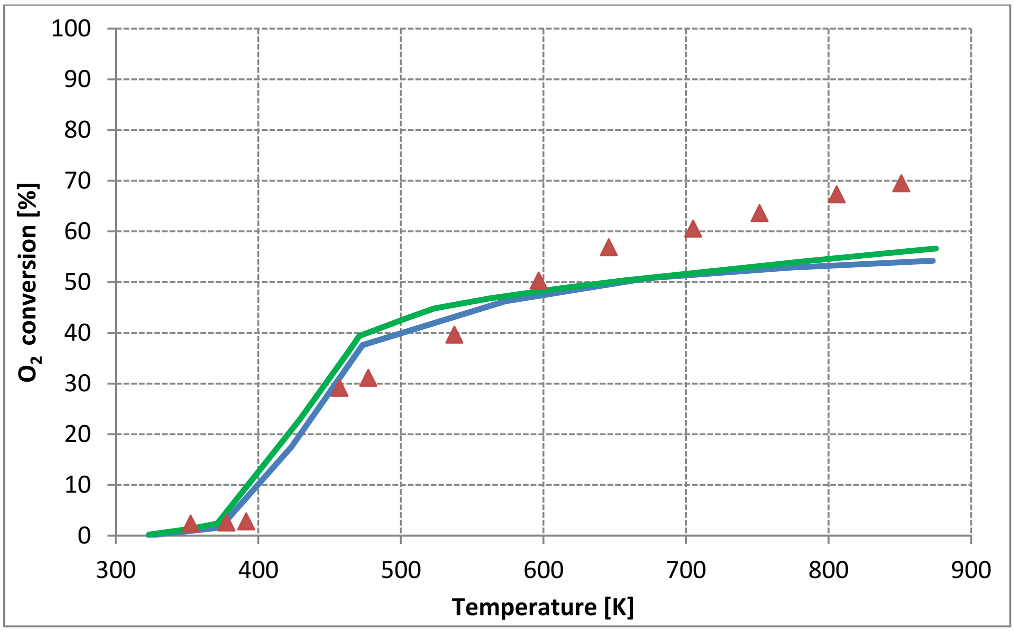

Figure 5.3. Conversion of O_2 vs. temperature at flow rate of 1.096 Nl/min.

The effect of a higher flow rate is presented in Figure 5.3. This led to a lower conversion of reactants and thus the complete consumption of O_2 is not reached. In this case the behaviour of the system is controlled by external mass diffusion phenomena.

It is important to highlight two main issues:

- ✓ The predicted conversion in the low temperature range is overestimated. As previously said, the axial profile of the oxygen molar fraction depicted in Figure 4.6.a shows that its concentration does not fall to zero near the catalytic surface. Since the model is not able to describe intra-porous diffusion processes, the computed conversion is higher than the real one.
- ✓ The numerical solution qualitatively follows the trend to a plateau but does not reach the measured value. Indeed, from the previous three plots it is noticeable that the experimental data show an enhanced conversion respect to the model predictions. The reasons of this discrepancy in the high temperature range are discussed by Maestri and co-workers: the main hypothesis is that Rh evaporation and redeposition downstream the catalytic bed occurred. This brought to the creation of zones of low catalytic activity outside the catalytic bed. Even if at low temperatures these contributions are negligible, at higher temperatures a rise of the oxygen conversion is observable.

The previous hypothesis is investigated by considering the two section with low catalytic activity upstream and downstream the catalytic bed. A catalyst layer of 0.2 cm is added upward the main bed. Another one is added downstream, with a length of 0.7 cm. The catalytic activity of these beds is lowered to 1% of that of the main bed. In Figure 5.4 the catalytic activity profile is shown.

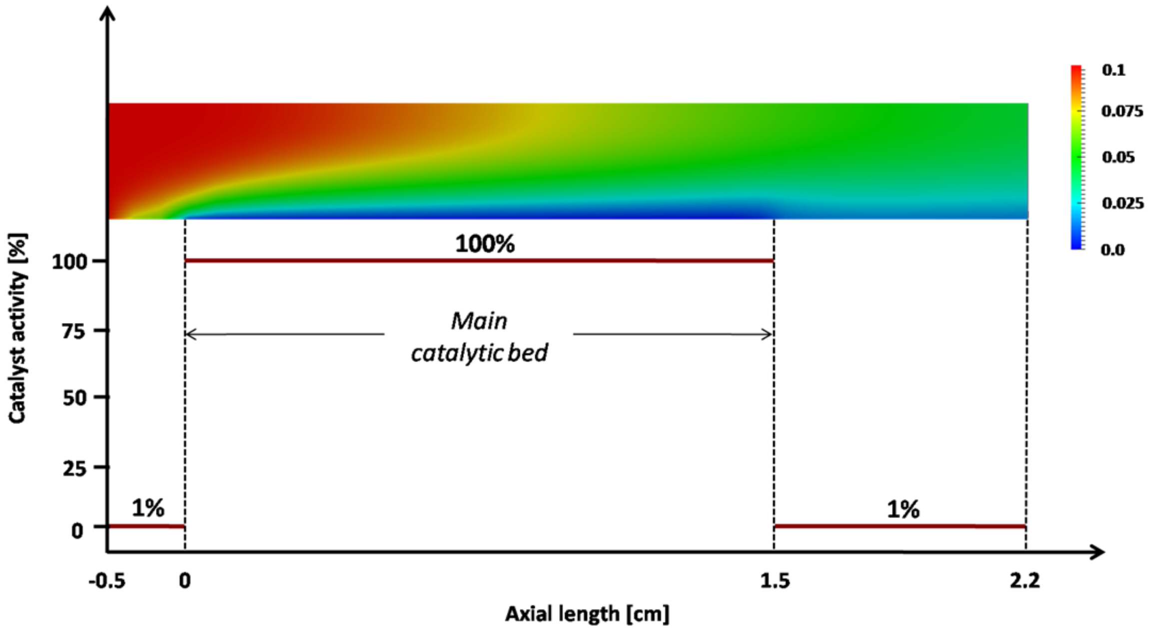

Figure 5.4. Activity of the catalytic bed vs. axial reactor length.

In Figure 5.5 the effect of temperature on oxygen conversion for the extended catalytic bed is represented. The simulations are performed with the highest flow rate of 1.096Nl/min.

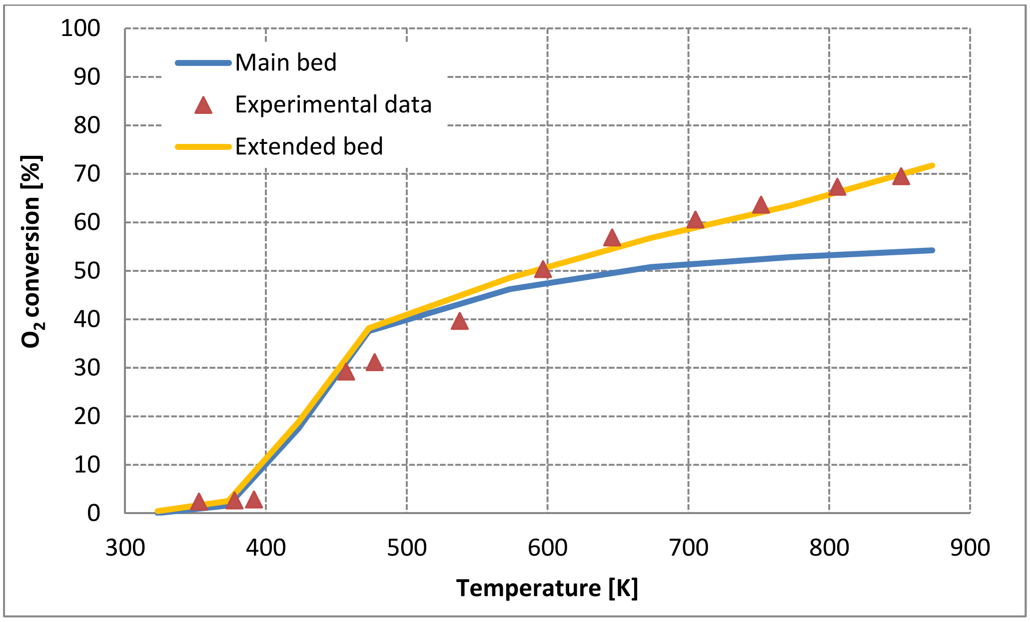

Figure 5.5. O_2 conversion vs. temperature for different catalytic bed at 1.096Nl/min.

The additional low activity sections besides the main bed lead to an increase of the conversion. At low temperatures the contribution is almost negligible. At high temperatures the conversion obtained perfectly fits the experimental data. Due to the low amount of catalyst these two sections work in chemical regime (Maestri, Beretta et al.

2008). The simulations performed at 0.274 Nl/min and 0.548 Nl/min show the same good agreement with the experimental data.

5.2.2. Start-up dynamic

In this section an analysis of the dynamic behaviour of the reactor start-up is described. Initially, the reactor is filled with N_2 at the operating temperature of 773.15 K. The other parameters are reported in Table 4.1.The reacting mixture is continuously fed into the reactor with a flow rate of 0.274Nl/min. The ignition of the mixture is instantaneous and the steady-state is achieved in about 200 ms.

The velocity profile is completely developed after 15 ms, as shown in Figure 5.6. The first profile is sampled at the initial time of the numerical simulation. The second is the velocity profile at 2 ms and the third is the trend at steady-state condition.

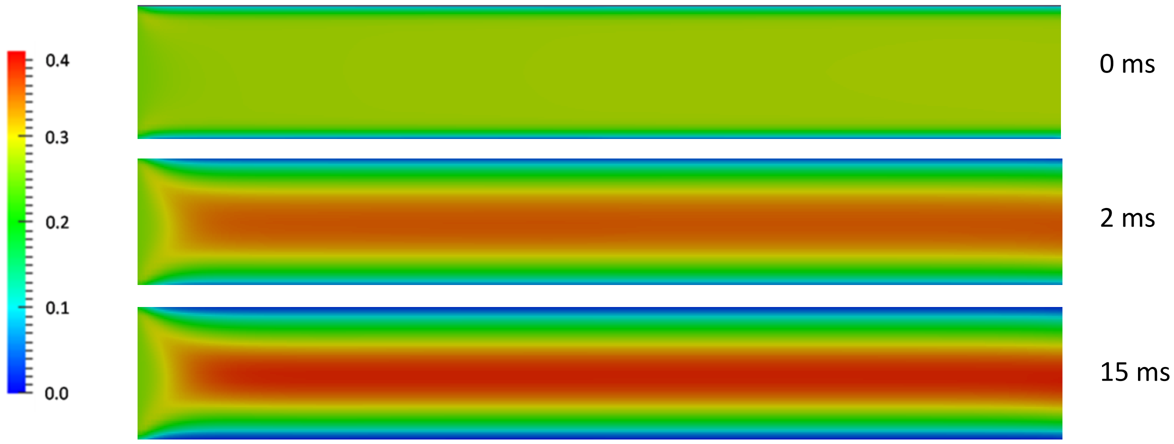

Figure 5.6. Velocity magnitude [m s^{-1}]profiles at 773.15 K at 0, 2 and 15 ms.

In Figure 5.7 the O_2 profiles at different times are reported. The catalytic layer is located in the lower part of the figures.

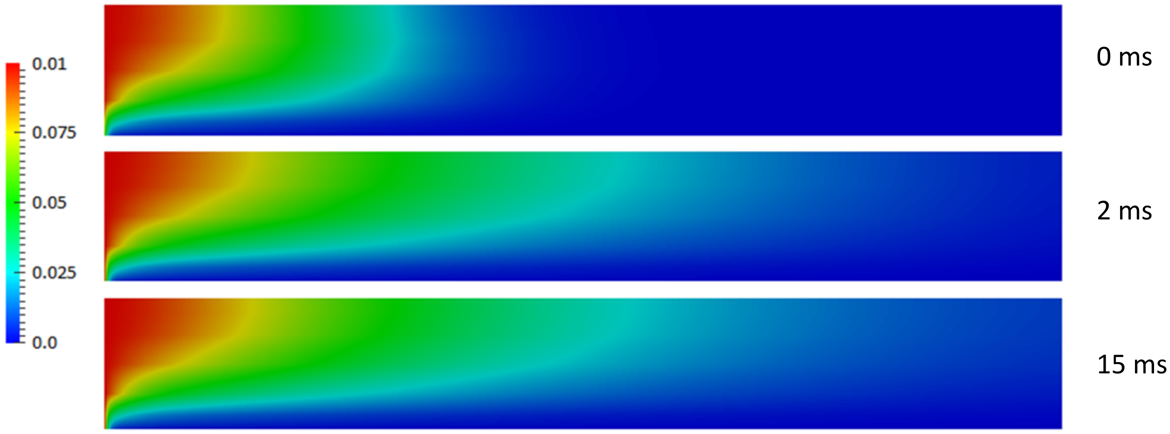

Figure 5.7. O_2 mole fraction profiles at 0, 2 and 15 ms at 773.15 K.

In the very first part of the reactor near the catalyst an abrupt decrease of O_2 concentration is observed. This reveals the presence of strong axial gradients of composition. It is possible to see that the O_2 concentration at the reactor outlet in steady-state conditions is almost zero.

Furthermore, it is possible to notice the formation of a boundary layer in which the O_2 is quickly consumed. The layer is established as soon as the reactants approach the catalyst and causes the creation of axial and radial gradients. In Figure 5.8 the O_2 radial profiles sampled at 10^{-10} m near the reactor inlet are reported. The 5 curves are superimposed because the reaction rate is very high and the temporal evolution of the gradient is too fast to be analyzed from the plot.

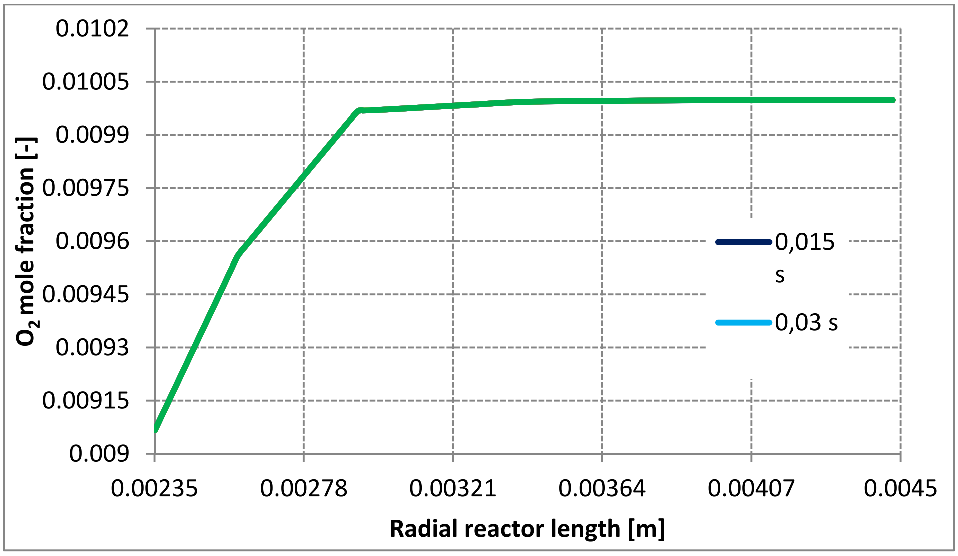

Figure 5.8. O_2 mole fraction profiles vs. radial coordinate at the reactor inlet at 15, 30, 50, 100 and 200 ms at 773.15 K.

The H_2 profiles are presented in Figure 5.9. As for the O_2, the H_2 mole fraction decreases quickly in the first part of the reactor. At 15 ms the second half of the reactor is still filled with nitrogen. At 50 ms the steady-state profile is almost reached: the H_2 concentration becomes uniform in the second part of the reactor. This is caused by the low reaction rates owed to the almost total consumption of O_2 in the first half of the reactor.

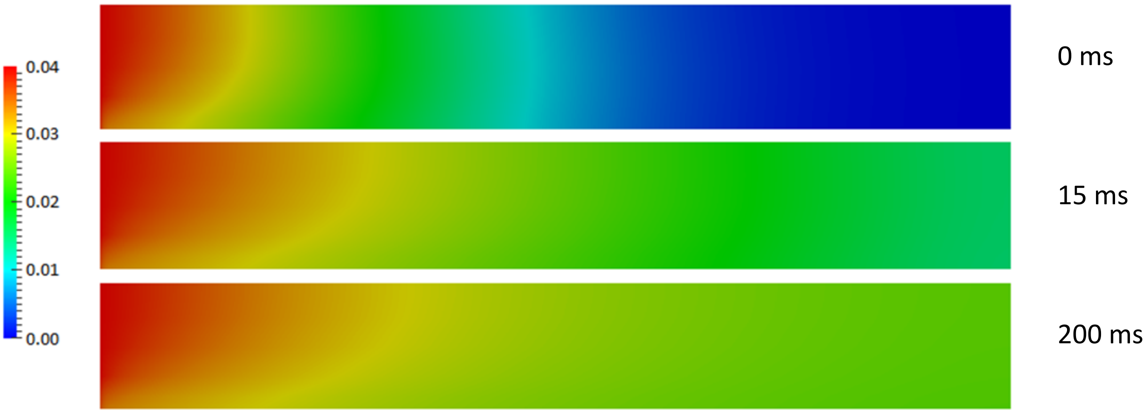

Figure 5.9.H_2 mole fraction profiles at 0, 15 and 200 ms at 773.15 K.

The axial gradients of H_2 are presented in Figure 5.10. These profiles are sampled near the catalytic wall, at 10^{-10} m far from the inlet. In the very first part of the reactor there is a strong decrease of H_2. In this section of the reactor, H_2 and O_2 are quickly absorbed. After few micrometer the gaseous O_2 in the boundary layer is completely consumed. As a consequence, by proceeding along the axial coordinate of reactor, the H_2 concentration decreases more gradually. During the emptying of the reactor, the conversion falls to zero because of the presence of N_2. At steady-state the mole fraction of H_2 reaches the plateau.

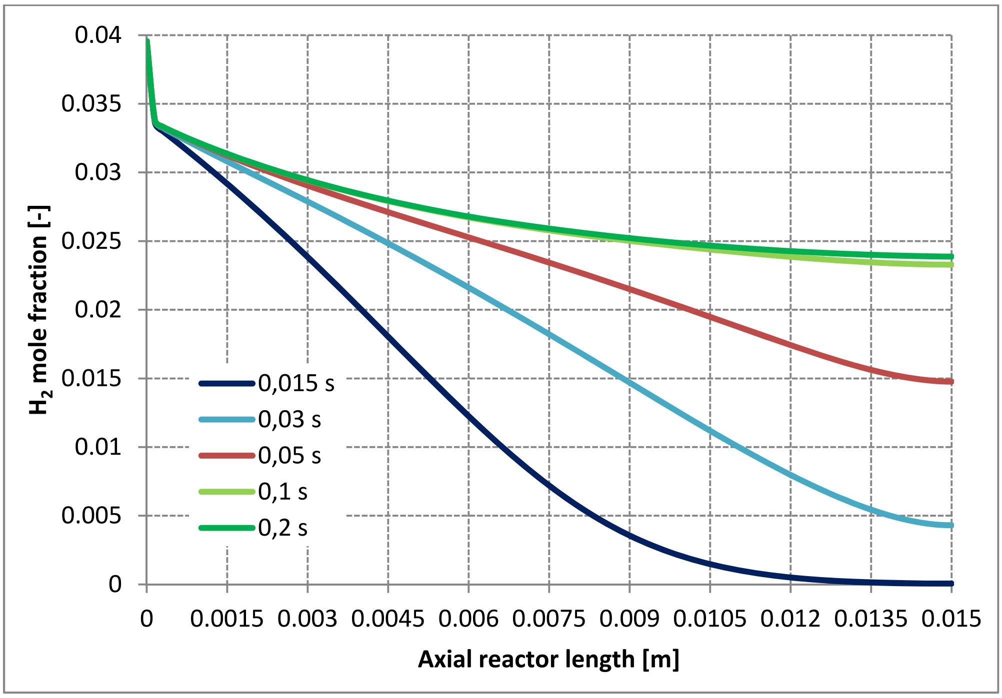

Figure 5.10. H_2 mole fraction profiles vs. axial coordinate near the catalytic wall at 15, 30, 50, 100 and 200 ms at 773.15 K.

The same profiles has been sampled near the outer wall. The resulting trends are shown in Figure 5.11.

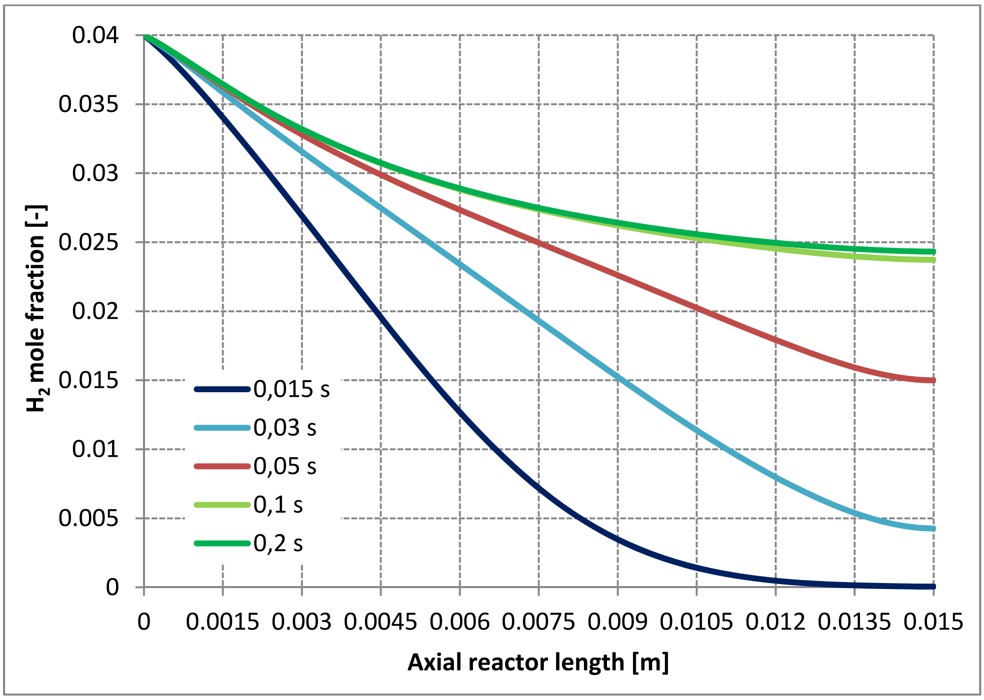

Figure 5.11. H_2 mole fraction profiles vs. axial coordinate near the outer wall at 15, 30, 50, 100 and 200 ms at 773.15 K.

It is possible to notice that the slopes of these gradients are smaller than those sampled near the catalyst. As for the previous curves, the plateau is achieved in the second part of the reactor. This points out the presence of radial gradients mainly in the initial part of the reactor.

In Figure 5.12 the profiles of H_2O are reported. It can be observed that the mole fraction of H_2O has an opposite behaviour with respect to the reactants. After 15ms the formation of the boundary layer can be observed.

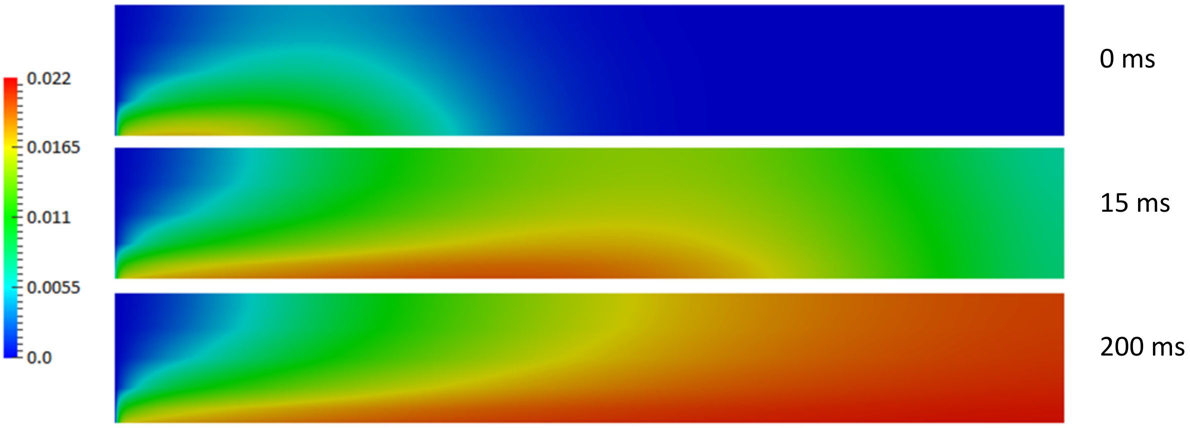

Figure 5.12. H_2O mole fraction profiles at 0, 15 and 200 ms at 773.15 K.

As soon as the reactants enter the reactor, H_2O formation is predicted. This can be observed in Figure 5.13, where the H_2O axial profiles are shown. The maximum formed at the initial time disappears with the achievement of the steady-state trend.

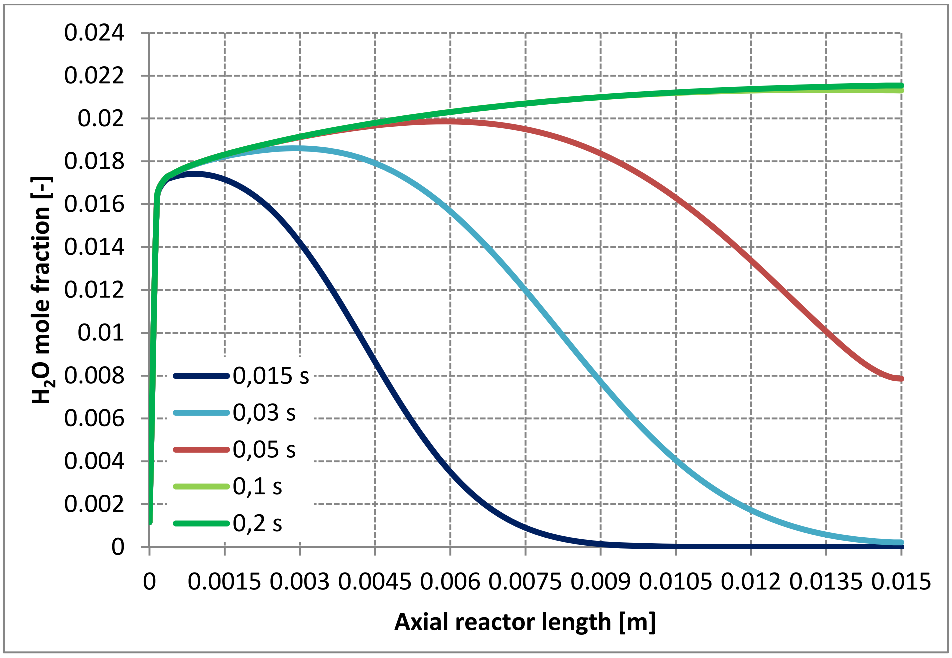

Figure 5.13. H_2O mole fraction profiles vs. axial coordinate near the catalytic wall at 15, 30, 50, 100 and 200 ms at 773.15 K.

The analysis proceed by observing the coverage profiles on the catalyst surface. In Figure 5.14 the profiles of free site fraction along the axial reactor coordinate are reported. A fast adsorption of species on the catalytic surface at the very beginning of the reactor can be noticed. This indicates the existence of a small zone with a high site occupancy level. At the initial time the reactor is filled with N_2 and all the site are free.

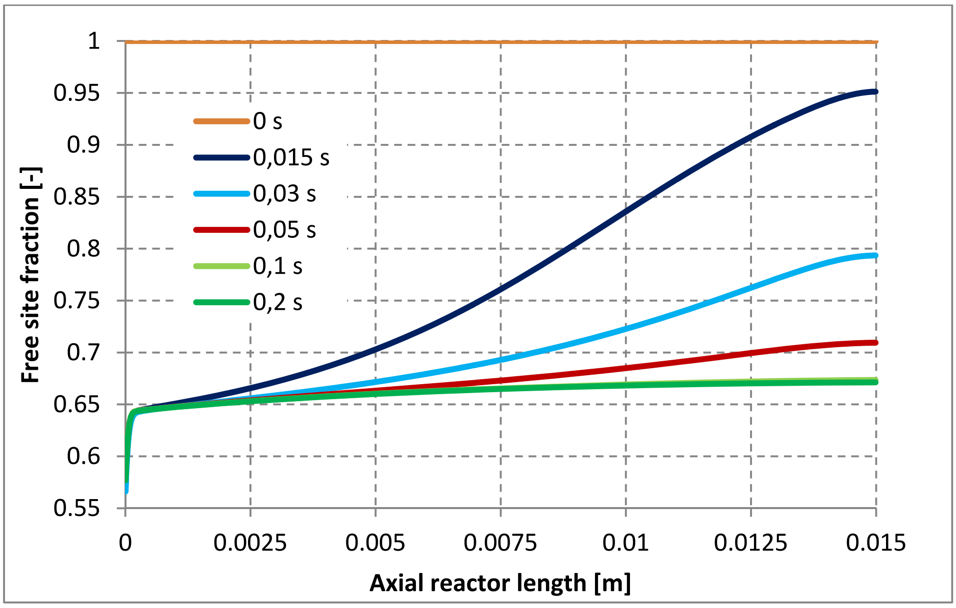

Figure 5.14. Rh site fraction profiles vs. axial coordinate on the catalytic surface at 0, 15, 30, 50, 100, 200 ms at 773.15 K.

The Most Abundant Reaction Intermediate (MARI) is the H*: its dynamic is shown in Figure 5.15. By comparing Figure 5.15 with Figure 5.14, it can be seen that the fraction of sites occupied by H_2 is complementary to that of the free Rh sites. The accumulation of this species on the catalyst indicates the presence of a bottleneck in the reaction mechanism.

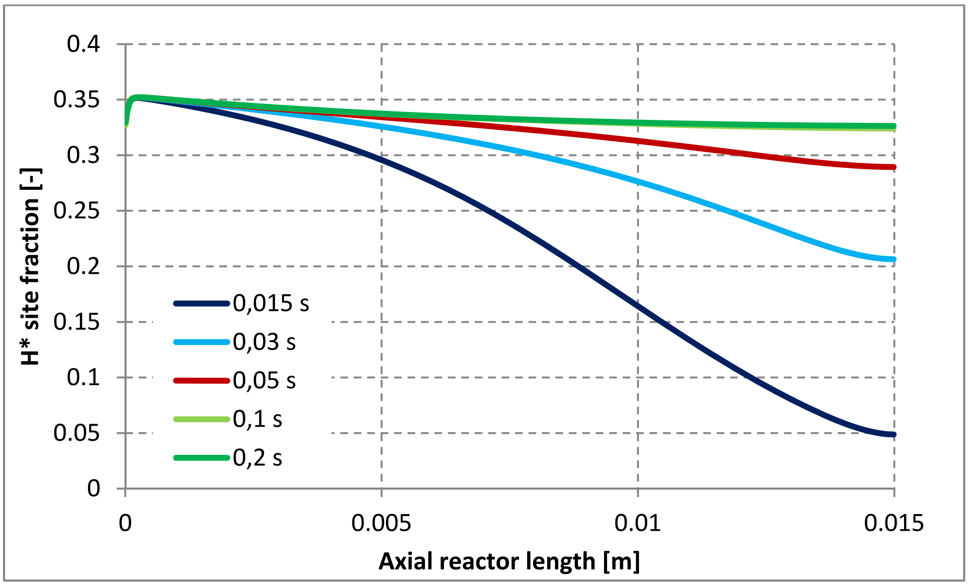

Figure 5.15. H* site fraction profiles vs. axial coordinate on the catalytic surface at 15, 30, 50, 100 and 200 ms at 773.15 K.

Taking into account the relative abundance of the other adsorbed species it can be seen that the amount of O_2 on the catalyst is very low. In Figure 5.16 the profile of O_2 on the catalyst is shown.

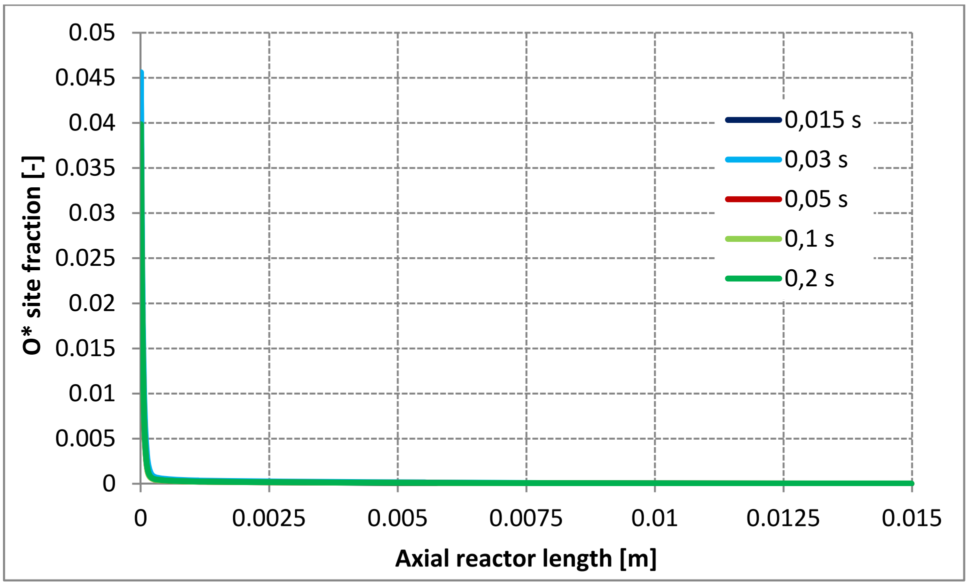

Figure 5.16. O* site fraction profile on the catalytic surface at 15, 30, 50, 100 and 200 ms at 773.15 K.

An abrupt decrease of O_2 on the surface at the very beginning of the catalyst can be noticed. Apart from this thin slice, the amount of O_2 on the catalyst is almost zero. This is due to the absence of gaseous O_2 in the zone close to the catalytic layer. Taking into account the plot of Figure 4.6, one can notice that the O_2 concentration in the boundary layer falls to zero in very first portion of the reactor. Thus, at these operating conditions the reactivity of the system is determined by the diffusion processes in the gas phase.

When the system is under chemical regime, it is possible to verify that the Rate Determining Step (RDS) of this microkinetic mechanism is the adsorption of O_2, as reported in (Maestri, Vlachos et al. 2009). Comparing the profiles of adsorbed and gaseous O_2 at 423.15 K (Figure 4.6 and 4.10) it is possible to see that the O* is the less abundant species on the catalyst and the H* is the MARI of the system. Furthermore, there is a considerable amount of O_2 near the catalytic surface. Taking a look at the reaction mechanism depicted in Figure 5.17 it can be concluded that the system behaviour is coherent with the proposed RDS.

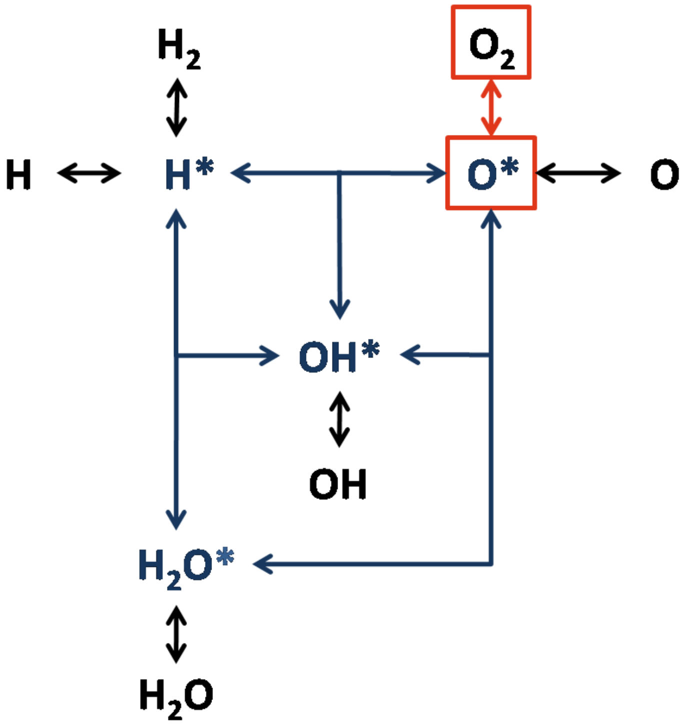

Figure 5.17. Schematization of the reaction mechanism of H_2 on Rh.

5.2.3. Eccentricity

The analysis provided by Maestri and coworkers presented the investigation of an annular reactor with perfect concentric circles. Anyway, an eccentricity of the annulus is possible when dealing with systems of small dimensions such as short contact time reactors. Usually eccentricity is not a desired property of the system and it is a result of manufacturing tolerances or of deformation in service. For the experimental apparatus considered, the eccentricity parameter can rise up to 50% (Beretta A. personal communication). In the rest of this discussion the following definition of eccentricity will be adopted:

$$e^* = \frac{\Delta x}{r_o - r_i} \tag{5.1}$$

where *Δx* is the distance between the centers of the circles and $r_0$and r_i are respectively the outer and the inner radius.

The system studied in the following is the same of section 5.2 but it presents an eccentricity of 50%. The operating conditions are listed in Table 4.1. The simulations are performed in isothermal and isobaric conditions.

The study of eccentric annular ducts is only made possible by adopting a three dimensional model. The system considered is symmetric and thus the final computational mesh represents only one half of the reactor. This results in a great saving of computational effort. The grid employed is composed by 10 cells in the radial direction, 100 cells in the axial coordinate and 20 cells in the azimuthal direction and it is reported in Figure 5.18.

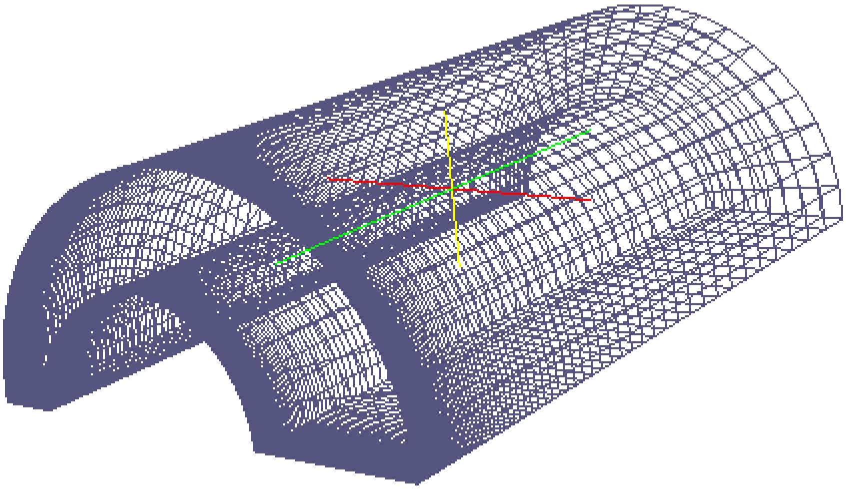

Figure 5.18. Computational 3D grid for the annulus reactor with an eccentricity of 50%.

According to (Shah and London 1978), the effect of eccentricity is to lower the asymptotic value of the Sherwood number. Specifically, for the eccentricity of 50% and with a ratio between the radius of 0.5 the Sherwood number is expected to fall from 5.76, in case of perfect concentric annulus, to 2.18. For this reason, we expect to observe a reduced conversion of O_2 in the eccentric reactor.

The O_2 mole fraction profiles at the reactor outlet are shown in Figure 5.19 for the two different configurations.

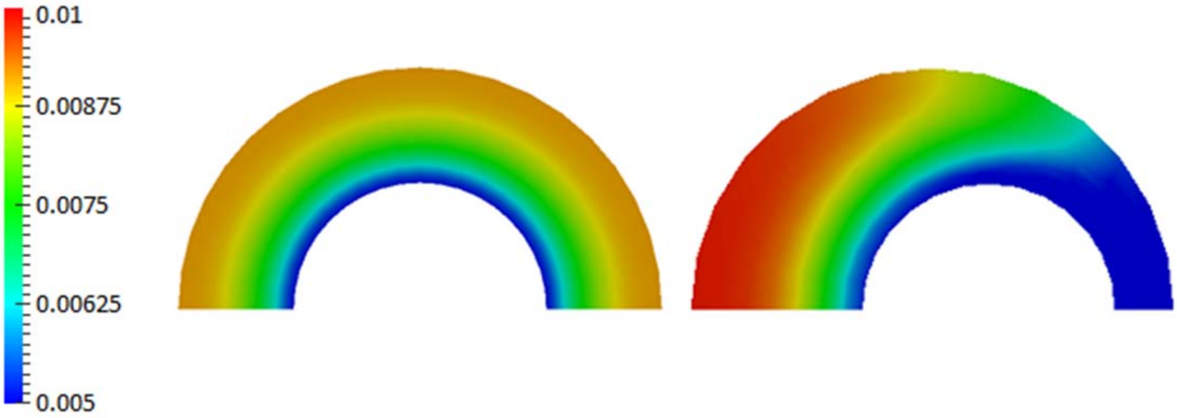

Figure 5.19. O_2 mole fraction profiles at different eccentricities at 423.15 K.

It is possible to see that the O_2 is mostly consumed on the catalytic layer and specifically in the reduced part of the section.

The axial O_2 profiles in the 3D mesh are represented in Figure 5.20.

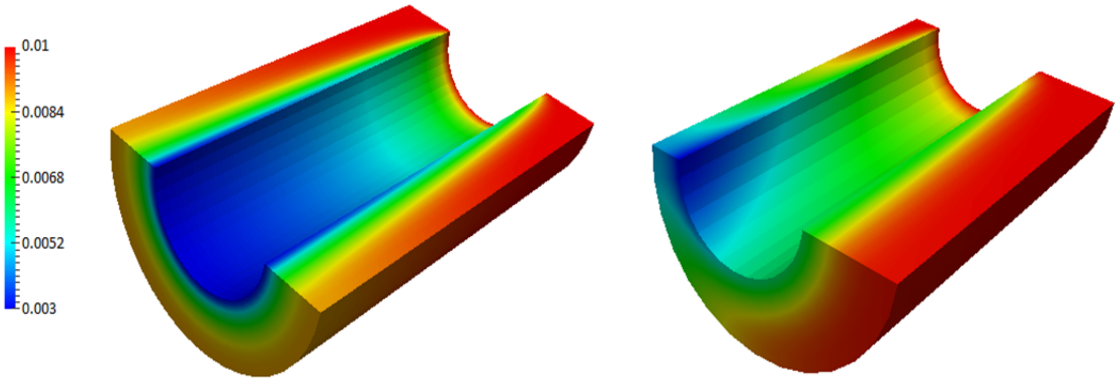

Figure 5.20. O_2 mole fraction profiles in the 3D mesh at the reactor inlet at 423.15 K for the concentric and eccentric configuration.

The profiles of conversion of O_2 at different temperatures are depicted in Figure 5.21. It is possible to notice that with an eccentricity of 50% the O_2 conversion is inferior to that obtained with the concentric configuration. For this reason the predicted results obtained with catalyticFOAM are coherent with the expected behaviour of the system.

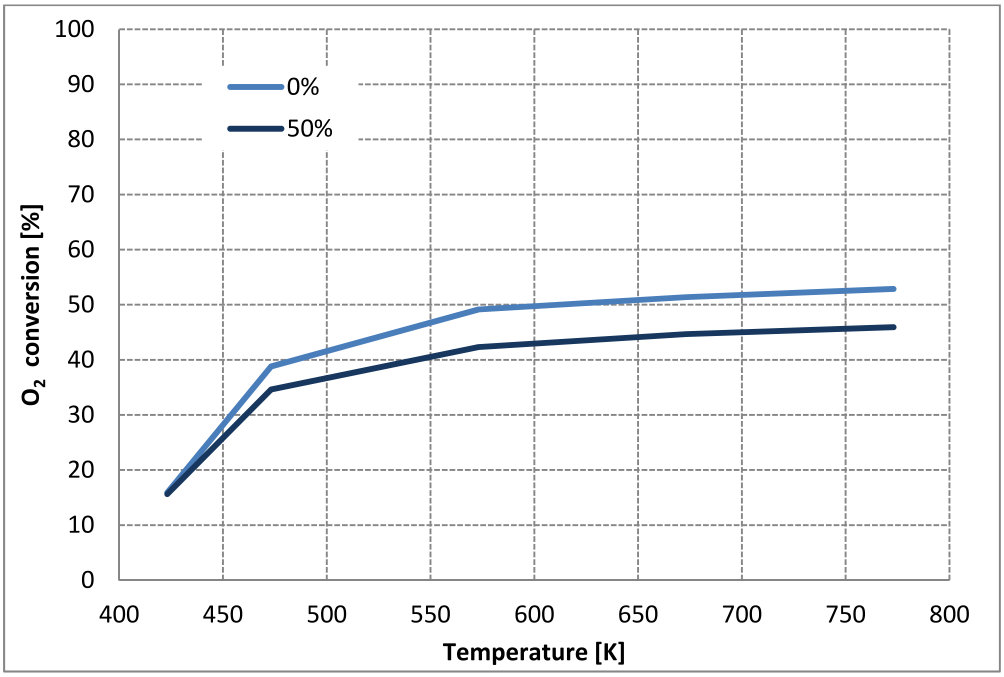

Figure 5.21. O_2 conversion profiles vs. temperature for different eccentricity.

Conclusions

In this work a solver for the detailed simulation of gas-solid catalytic reactors based on microkinetic description of surface chemistry has been developed. A fully first-principles approach i.e. the governing equations are adopted at each scale has been adopted for the description of phenomena:. These systems presents the following numerical issues: elevate number of unknowns, non-linearity and stiffness of the problem. Its efficient solution has been made possible by using an operator splitting technique.

The catalyticFOAM solver allows for the solution of Navier-Stokes equations both in laminar and turbulent regime. Simulations can be performed in isothermal and adiabatic conditions. Moreover, any arbitrary complex geometric domain can be investigated.

A library for the handling of surface kinetic schemes has been developed. Thus, it is possible to implement detailed reaction mechanisms both for the gas and surface phase. In particular UBI-QEP kinetic schemes are supported as well as standard CHEMKIN format.

A series of numerical tests have been made in order to test the performances of the solver. From these emerged that the construction of the computational mesh is of fundamental importance in order to reach convergence. Furthermore, the time discretization is strongly influenced by the time step, derived from the Courant number.

The reliability and predictive capability of catalyticFOAM have been tested by comparing the numerical results with the experimental data. Furthermore, it has been possible to simulate different conditions from the idealized one and to provide an exhaustive discussion on the behaviour of the system. The results highlight the potential great generality and flexibility of catalyticFOAM.

Future developments deal with improving the reliability and applicability of catalyticFOAM. Specifically:

- ✓ Modeling of the solid catalyst: diffusion and reaction.

- ✓ Description of thermal behavior of the solid catalytic structure.
- ✓ Development of a tool for the reaction path analysis based on actual reaction rate (Maestri 2011).
- ✓ Improvement of computational efficiency of the code.
- ✓ Code parallelization.

Appendix A

In this section the derivations of conservation equations of mass and energy for a batch reactor are provided. Moreover the boundary conditions at the catalytic surface expressed for the surface species and temperature are reported.

A1. Total mass conservation

The expression of the total mass balance for a batch reactor can be written as:

$$\frac{dm_{tot}}{dt} = \sum_{i=1}^{NC} \frac{dm_i}{dt}$$

Splitting the source term in the homogeneous and heterogeneous terms:

$$\sum_{i=1}^{NC} \frac{dm_i}{dt} = V_{react} \sum_{i=1}^{NC} \hat{R}_i^{hom} + \sum_{i=1}^{NC} \sum_{k=1}^{NCF} \dot{m}_{ik}^{het}$$

Where NCF indicates the number of catalytic faces of the computational cell.

The mass fluxes from and to the *k*th catalytic face of the cell can be computed as:

$$\dot{m}_{ik}^{het} = A_{cat}^{(k)} \tilde{R}_{ik}^{het} MW_i$$

In order to express the area of the *k*th catalytic face of the cell in terms of geometric area, the parameter $\alpha_{cat}$is introduced. This is an intensive property of the catalyst and is defined as:

$$\alpha_{cat} = \frac{A_{cat}}{A_{react}}$$

Since the sum of production rates in the gas phase is zero, the equation can be written as:

$$\frac{dm_{tot}}{dt} = \sum_{i=1}^{NC}\sum_{k=1}^{NCF} \dot{m}_{ik}^{het} = \sum_{i=1}^{NC}\sum_{k=1}^{NCF}\left(\alpha_{cat}^{(k)} A_{face}^{(k)} \tilde{R}_{ik}^{het} MW_i\right) = \sum_{k=1}^{NCF} \alpha_{cat}^{(k)} A_{face}^{(k)} \sum_{i=1}^{NC} \tilde{R}_{ik}^{het} MW_i$$

Where $\hat{R}_i^{hom}$ and $\tilde{R}_{ik}^{het}$ are the rates of production of the *i*th species.

A2. Species mass conservation

The generic expression for the mass balance of the *i*th species is defined as the accumulation (derivative of mass over time) equal to the net mass flow (inlet minus outlet mass flows) plus the mass generation due to the reactions (R_i). The mathematical formula is:

$$\frac{dm_i}{dt} = m_i^{IN} - m_i^{OUT} + R_i$$

The inlet and outlet mass flows are neglected because we adopt a batch reactor model, i.e. the system is thermodynamically closed. Splitting the reaction term into homogeneous and heterogeneous:

$$\frac{d(m_{tot}\omega_i)}{dt} = \omega_i \frac{dm_{tot}}{dt} + m_{tot}\frac{d\omega_i}{dt} = \tilde{R}_i^{hom} MW_i V + \sum_{k=1}^{NCF}\left(\alpha_{cat}^{(k)} A_{face}^{(k)} \tilde{R}_{ik}^{het} MW_i\right)$$

Recalling the expression for the total mass balance derived in section A.1:

$$\frac{d\omega_i}{dt} = \frac{\tilde{R}_i^{hom} MW_i V}{m_{tot}} + \frac{\sum_{k=1}^{NCF}\left(\alpha_{cat}^{(k)} A_{face}^{(k)} \tilde{R}_{ik}^{het} MW_i\right)}{m_{tot}} - \frac{\omega_i}{m_{tot}} \sum_{k=1}^{NCF} \alpha_{cat}^{(k)} A_{face}^{(k)} \sum_{i=1}^{NC} \tilde{R}_{ik}^{het} MW_i$$

Introducing the density:

$$\frac{d\omega_i}{dt} = \frac{\tilde{R}_i^{hom} MW_i}{\rho} + \frac{\sum_{k=1}^{NCF}\left(\alpha_{cat}^{(k)} A_{face}^{(k)} \tilde{R}_{ik}^{het} MW_i\right)}{\rho V_{react}} - \frac{\omega_i}{\rho V_{react}} \sum_{k=1}^{NCF} \alpha_{cat}^{(k)} A_{face}^{(k)} \sum_{i=1}^{NC} \tilde{R}_{ik}^{het} MW_i$$

Grouping the surface terms:

$$\frac{d\omega_i}{dt} = \frac{\tilde{R}_i^{hom} MW_i}{\rho} + \frac{1}{\rho V_{react}}\left(\sum_{k=1}^{NCF}\left(\alpha_{cat}^{(k)} A_{face}^{(k)} \tilde{R}_{ik}^{het} MW_i\right) - \omega_i \sum_{k=1}^{NCF} \alpha_{cat}^{(k)} A_{face}^{(k)} \sum_{i=1}^{NC} \tilde{R}_{ik}^{het} MW_i\right)$$

The final expression for the mass conservation of the *i*th species is:

$$\frac{d\omega_i}{dt} = \frac{\tilde{R}_i^{hom} MW_i}{\rho} + \frac{1}{\rho V_{react}} \left[\sum_{k=1}^{NCF} \alpha_{cat}^{(k)} A_{face}^{(k)} \left(\tilde{R}_{ik}^{het} MW_i - \omega_i \sum_{i=1}^{NC} \tilde{R}_{ik}^{het} MW_i \right) \right]$$

A3. Energy conservation equation

The equation for the energy conservation in a batch reactor is written as follows

$$\frac{dH_{tot}}{dt} = \sum\nolimits_k \dot{H}_k^{het}$$

The total enthalpy of the system is expanded as follows:

$$H_{tot} = \sum_{i=1}^{NCF} m_i \, \widehat{H}_i^{hom} = m_{tot} \sum_{i=1}^{NCF} \omega_i \widehat{H}_i^{hom}$$

The heterogeneous enthalpy term of the *k*th faces of the cells is

$$\dot{H}_k^{het} = \dot{m}_k^{het} \widehat{H}_k^{het} = \sum_{i=1}^{NCF} \dot{m}_{jk}^{het} \widehat{H}_{jk}^{het} = \sum_{i=1}^{NCF} \tilde{R}_{ik}^{het} MW_i \alpha_{cat}^{(k)} A^{(k)} \widehat{H}_{ik}^{het}$$

The second term the conservation energy becomes:

$$\sum\nolimits_k \dot{H}_k^{het} = \sum_{k=1}^{NCF} \alpha_{cat}^{(k)} A^{(k)} \sum_{i=1}^{NCF} \tilde{R}_{ik}^{het} MW_i \widehat{H}_{ik}^{het}$$

The first term of the conservation energy can be written as

$$\frac{dH_{tot}}{dt} = \frac{d}{dt}\left(m_{tot} \sum_{i=1}^{NCF} \omega_i \widehat{H}_i^{hom} \right) = m_{tot} \frac{d}{dt}\left(\sum_{i=1}^{NCF} \omega_i \widehat{H}_i^{hom} \right) + \omega_i \widehat{H}_i^{hom} \frac{dm_{tot}}{dt} =$$

$$= \widehat{H}_{tot} \frac{dm_{tot}}{dt} + m_{tot} \sum_{i=1}^{NCF} \omega_i \frac{d\widehat{H}_i^{hom}}{dt} + m_{tot} \sum_{i=1}^{NCF} \widehat{H}_i^{hom} \frac{d\omega_i}{dt} =$$

$$\underbrace{= \widehat{H}_{tot} \frac{dm_{tot}}{dt}}_{\text{I° term}} + \underbrace{m_{tot} \widehat{c}_p \frac{dT}{dt}}_{\text{II° term}} + \underbrace{m_{tot} \sum_{i=1}^{NCF} \widehat{H}_i^{hom} \frac{d\omega_i}{dt}}_{\text{III° term}}$$

The III° term can be derived as:

$$m_{tot}\sum_{i=1}^{NCF}\widehat{H}_i^{hom}\frac{d\omega_i}{dt} = m_{tot}\sum_{i=1}^{NCF}\widehat{H}_i^{hom}\frac{R_i^{hom}MW_i}{\rho} +$$

$$+m_{tot}\sum_{i=1}^{NCF}\frac{\widehat{H}_i^{hom}}{\rho V}\left[\sum_{k=1}^{NCF}\alpha_{cat}^{(k)}A^{(k)}\left(\tilde{R}_{ik}^{het}MW_i - \omega_i\sum_{l=1}^{NCF}\tilde{R}_{ik}^{het}MW_l\widehat{H}_{lk}^{het}\right)\right]$$

The II° term can be written as:

$$m_{tot}\sum_{i=1}^{NCF}\widehat{H}_i\frac{d\omega_j}{dt} =$$

$$= V\sum_{i=1}^{NCF}\widehat{H}_i^{hom}\widehat{R}_i + \sum_{i=1}^{NCF}\widehat{H}_j\left[\sum_{k=1}^{NCF}\alpha_{cat}^{(k)}A^{(k)}\left(\tilde{R}_{ik}^{het}MW_i - \omega_i\sum_{l=1}^{NCF}\tilde{R}_{ik}^{het}MW_l\right)\right] =$$

$$= V\sum_{i=1}^{NCF}\widehat{H}_i^{hom}\widehat{R}_i + \sum_{i=1}^{NCF}\widehat{H}_j\sum_{k=1}^{NCF}\alpha_{cat}^{(k)}A^{(k)}\tilde{R}_{ik}^{het}MW_i -$$

$$\sum_{k=1}^{NCF}\alpha_{cat}^{(k)}A^{(k)}\sum_{i=1}^{NCF}\omega_i\widehat{H}_i^{hom}\sum_{l=1}^{NCF}\tilde{R}_{ik}^{het}MW_l =$$

$$= V\sum_{i=1}^{NCF}\widehat{H}_i^{hom}\widehat{R}_j + \sum_{i=1}^{NCF}\widehat{H}_j\sum_{k=1}^{NCF}\alpha_{cat}^{(k)}A^{(k)}\tilde{R}_{ik}^{het}MW_i -$$

$$\underbrace{\sum_{k=1}^{NCF}\alpha_{cat}^{(k)}A^{(k)}\widehat{H}_{tot}\sum_{l=1}^{NCF}\tilde{R}_{ik}^{het}MW_l =}$$

This term is simplified with the I° one

Then, at the first term is obtained

$$\frac{dH_{tot}}{dt} = m_{tot}\widehat{c_p}\frac{dT}{dt} + V\sum_{i=1}^{NCF}\widehat{H}_i^{hom}\widehat{R}_i + \sum_{i=1}^{NCF}\widehat{H}_j\sum_{k=1}^{NCF}\alpha_{cat}^{(k)}A^{(k)}\tilde{R}_{ik}^{het}MW_i$$

The second term becomes

$$\sum_k \dot{H}_k^{het} = \sum_{k=1}^{NCF} \alpha_{cat}^{(k)} A^{(k)} \sum_{i=1}^{NCF} \tilde{R}_{ik}^{het} MW_i \widehat{H}_{ik}^{het}$$

Recomposing the initial energy equation we have

$$m_{tot}\widehat{c_p}\frac{dT}{dt} =$$

$$= -V\sum_{i=1}^{NCF} \widehat{H}_i^{hom}\,\widehat{R}_\iota + \sum_{i=1}^{NCF} \widehat{H}_i^{hom} \sum_{k=1}^{NCF} \alpha_{cat}^{(k)} A^{(k)} \tilde{R}_{ik}^{het} MW_i - \sum_{k=1}^{NCF} \alpha_{cat}^{(k)} A^{(k)} \sum_{i=1}^{NCF} \tilde{R}_{ik}^{het} MW_i \widehat{H}_{ik}^{het} =$$

$$= -V\sum_{i=1}^{NCF} \widehat{H}_i^{hom}\,\widehat{R}_\iota + \sum_{k=1}^{NCF} \alpha_{cat}^{(k)} A^{(k)} \sum_{i=1}^{NCF} \tilde{R}_{ik}^{het} MW_i (\widehat{H}_{ik}^{het} - \widehat{H}_i^{hom})$$

$$\frac{dT}{dt} = -\frac{1}{\rho\widehat{c_p}}\sum_{i=1}^{NCF} \widehat{H}_i^{hom}\,\widehat{R}_\iota + \frac{1}{\rho\widehat{c_p}V}\sum_{k=1}^{NCF} \alpha_{cat}^{(k)} A^{(k)} \sum_{i=1}^{NCF} \tilde{R}_{ik}^{het} MW_i (\widehat{H}_{ik}^{het} - \widehat{H}_i^{hom})$$

A4. Species composition gradient

The species composition gradient is expressed by the Fick's first law. This relates the diffusive flux per unit area to the concentration, by postulating that the flux goes from regions of high concentration to regions of low concentration, with a magnitude that is proportional to the concentration gradient. Since the diffusive flux is owed to the presence of the chemisorption reactions, the expression for the gradient in the direction perpendicular to the catalytic surface is:

$$\mathcal{D}_\mathrm{i}\frac{\partial c_i}{\partial r} = -\sum_{j=1}^{NR} R_j^{het}\nu_{ij}$$

where $\mathcal{D}_\mathrm{i}$ is the diffusive coefficient of the *i*th species in dimension of $[m^2 \cdot s^{-1}]$.

The concentration c_i can be state as the massive fraction multiplied by the density, expressed as the ratio of total mass over volume. Moreover, switching from fluxes per unit area to flows, we obtain:

$$A_{react}\mathcal{D}_{\mathrm{i}}\frac{\partial\left(\frac{m_{tot}\omega_i}{V_{react}MW_i}\right)}{\partial r}=-\sum_{j=1}^{NR}R_j^{het}\nu_{ij}A_{cat}$$

Since only the mass fraction varies over the radius length, all the other terms are excluded from the derivative. This leads to the following expression:

$$\frac{\partial\omega_i}{\partial r}=-\sum_{j=1}^{NR}\frac{R_j^{het}\nu_{ij}MW_iA_{cat}}{\rho\mathcal{D}_{\mathrm{i}}A_{react}}$$

The ratio among the catalytic area and the reactor surface stands for the α_{cat}.The final expression of the gradient of the gas-phase species concentration is:

$$\frac{\partial\omega_i}{\partial r}=-\sum_{j=1}^{NR}\frac{R_j^{het}\nu_{ij}MW_i}{\rho\mathcal{D}_{\mathrm{i}}}\alpha_{cat}$$

A5. Temperature gradient

The law of heat conduction, also known as Fourier's law, states that the heat flux through a material is proportional to the negative gradient of the temperature. Furthermore the heat flux is used in its one-dimensional form, in the direction perpendicular to the catalytic surface. The temperature gradient is imposed equal to the heat flux due to the heterogeneous reactions.

$$\lambda\frac{\partial T}{\partial r}=-\sum_{j=1}^{NR}R_j^{het}\Delta H_j$$

The gas conductivity λ has the dimensions of $[W\cdot m^{-1}\cdot K^{-1}]$. Switching from heat fluxes per unit area to heat flows:

$$A_{react}\,\lambda\frac{\partial T}{\partial r}=-\sum_{j=1}^{NR}R_j^{het}\Delta H_jA_{cat}$$

The entire equation is then divided by A_{react} in order to obtain the α_{cat} parameter. The temperature gradient has in the end the following form:

$$\frac{\partial T}{\partial r} = -\sum_{j=1}^{NR} \frac{R_j^{het} \Delta H_j \alpha_{cat}}{\lambda}$$

Appendix B

In this Appendix an introduction about the UBI-QEP method is provided. Moreover the equations for the computation of the activation energies is given.

B1. The UBI-QEP method

The Unity Bond Index-Quadratic Exponential Potential (UBI-QEP) method is an hybrid theoretical method created with the intention to develop a predictive surface mechanism with physic value. This technique is currently one of the best practically efficient methods to handle complex systems of reaction (Aghalayam, Park et al. 2000) (Mhadeshwar and Vlachos 2005) (Maestri, Vlachos et al. 2009).

In this technique, in order to compute the energetics of the heterogeneous reactions, the interactions among adsorbates species, i.e. the binding energy and the type of adsorption sites, are taken into account (Shustorovich 1998). For complex and practically considerable reacting systems the UBI-QEP method emerges: it has the widest applicability among all methods and it can determine reaction activation barriers with a high accuracy, typically set among 1-3 kcal/mol.

The UBI-QEP method is based on the following key assumptions:

- spherical forces, function of the inter-nuclear distance;
- in a many-body system the two-body interactions are by a quadratic potential of an exponential function of the distance, named bond index;
- the total energy of the main body system can be expressed as a summation of additive two-body bond energies governed by the UBI condition, *i.e.* the total bond index is normalized at unity. This condition is also known as unity bond index conservation(Shustorovich 1998).

Under these conditions the activation energy barriers are estimated by minimizing the energy of a two-body adsorbate configuration, function of the different bond indices.

In the following the mathematical description for an elementary surface reaction is provided.

Let us consider the generic surface reaction, such as:

$$A^* + B^* \leftrightarrow AB^* + *$$

where the * denotes the adsorbed species.

The reaction rate is calculated as the product among the reaction constant and the producer of the mole concentration either of gas species or adsorbed species elevated at the respective stoichiometric coefficient. The main difference stands in the computation of reaction rate constant and specifically of the activation energy. This is not constant but depends on the surface coverage and on temperature. Further details are provided in the next section.

In Figure B.1 the UBI-QEP activation barriers redrawn form the Lennard-Jones energy diagram is reported.

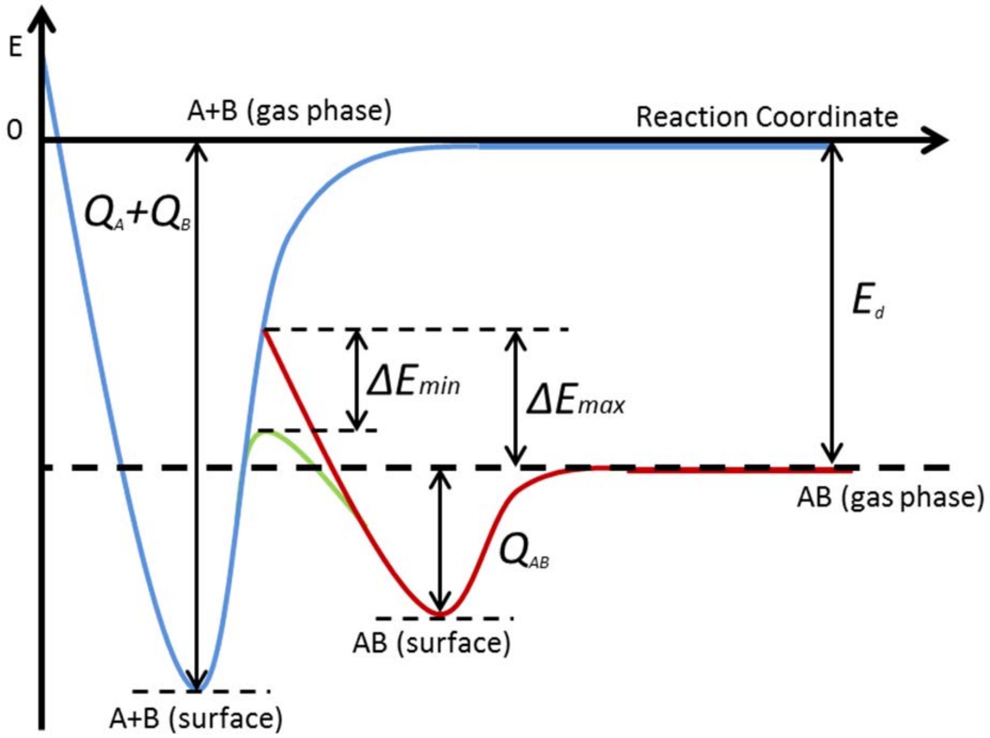

Figure B.1. One-dimensional UBI potential diagram of chemisorption and dissociation of

molecule AB.

The graphic represents the chemisorption and dissociation of a diatomic molecule AB and it is composed of two energy curves. The red line indentifies the interaction energy between adsorbate AB as a function of the distance from the surface. The blue one indicates the sum of interaction energies of atom A and atom B as a function of the distance from the surface. The green line stands for the correction of the position of the transition state. From the diagram it is possible to identify the intersection between reactants and products curves. This corresponds to the maximum of the interaction energy between AB and the catalyst surface. In order to calculate the heat of reaction it is necessary to subtract from this quantity the chemisorption energy minimum E_{min}, expressed as

$$E_{min} = -E_d - Q_{AB}$$

By adding the increment of energy ΔE_{max} above the minimum, the reaction energy turns in

$$E_{AB} = E_{min} + \Delta E_{max} = -E_d - Q_{AB} + \Delta E_{max}$$

The increment of energy ΔE_{max} represents the Lennard-Jones activation barrier relative to adsorbed AB. This energetic barrier ΔE_{AB} for is then computed as

$$\Delta E_{max} = E_d + Q_{AB} - Q_A - Q_B + \frac{Q_A Q_B}{Q_A + Q_B}$$

This quantity is overestimated and to take into account this discrepancy the bond index correction σ is introduced. The effective value of the dissociation energy of AB is expressed as:

$$\Delta E_{AB} = \Delta E_{max} - \Delta E_{min} = \sigma \cdot \Delta E_{max}$$

The UBI-QEP method assumes that the gas-phase species, e.g. A-B are stable in the sense that the enthalpy needed to dissociate the A-B bond is greater than zero, to satisfy the conservation of energy. The dissociation energy in the gas-phase E_d is defined as the enthalpy of the reaction that breaks the A-B bond, i.e. the gas-phase AB bond energy. This dissociation energy is calculated as:

$$E_{d,j} = \sum_{i=1}^{NP} \nu_{ij} H_i - \sum_{j=1}^{NR} \nu_{ij} H_i$$

The ΔH is the reaction enthalpy as it occurs on the surface and is the sum of the enthalpies of the steps of the thermodynamic cycle:

adsorbed reactants → gas-phase reactants $\Delta H_1 = \sum_r Q_r$

gas-phase reactants → gas-phase products $\Delta H_2 = \sum_p H_p - \sum_r H_r$

gas-phase products → adsorbed products $\Delta H_3 = -\sum_p Q_p$

The net of this thermodynamic cycle led to the conclusion that the reaction enthalpy depends on the heats of chemisorption of adsorbed species and the heat of the equivalent gas phase reaction. The resulting formula is

Net: adsorbed reactants→ adsorbed products

$$\Delta H = \Delta H_1 + \Delta H_2 + \Delta H_3 = \sum_r Q_r + \sum_p H_p - \sum_r H_r - \sum_p Q_p$$

The expression for the generic surface reaction considered till now is:

$$\Delta H = Q_A + Q_B - Q_{AB} + Q_j^{gas}$$

where Q_j^{gas} is the heat of gas–phase for the generic *j*th reaction and Q_i stands for the heat of chemisorption of surface species such as A, B, and AB.

B2. Activation energy

The equations for the activation energy calculation using the UBI-QEP method is provided in this section. Depending on the type of reaction, a specific expression for the calculation of enthalpy variation, forward and backward activation energies are pointed out. While deriving the UBI-QEP formulae, the thermodynamic consistency is ensured by the following relationship:

$$\Delta H = E_f - E_b$$

Here we lay down the analytical equations to estimate the activation energies for the 8 types of reactions considered.

1) Non-activated atomic on non-dissociative molecular adsorption, e.g. $A + * \leftrightarrow A^*$.

$$\Delta H = -Q_A$$

$$E_f = 0$$

$$E_b = Q_A$$

2) Non-activated homonuclear dissociative adsorption, e.g. $A_2 + 2 * \leftrightarrow 2A^*$.

$$\Delta H = E_d - 2Q_A$$

$$E_f = 0$$

$$E_b = 2Q_A - E_d$$

3) Activated homonuclear dissociative adsorption, e.g. $A_2 + 2 * \leftrightarrow 2A^*$.

$$\Delta H = E_d - 2Q_A$$

$$E_f = \sigma\left(E_d - Q_{A_2} - 1.5Q_A\right)$$

$$E_b = (\sigma - 1)E_d - \sigma Q_{A_2} + (2 + 1.5\sigma)Q_A$$

4) Activated homonuclear dissociative adsorption, e.g. $AB + 2^* \leftrightarrow A^* + B^*$.

$$\Delta H = E_d - Q_A - Q_B$$

$$E_f = \sigma\left(E_d - Q_{AB} - Q_A - Q_B + \frac{Q_A Q_B}{Q_A + Q_B}\right)$$

$$E_b = (\sigma - 1)E_d - \sigma Q_{AB} + (1 - \sigma)(Q_A - Q_B) + \sigma\frac{Q_A Q_B}{Q_A + Q_B}$$

5) Heteronuclear surface dissociation, e.g. $AB^* + * \leftrightarrow A^* + B^*$.

$$\Delta H = E_d + Q_{AB} - Q_A - Q_B$$

$$E_f = \sigma\left(E_d + Q_{AB} - Q_A - Q_B + \frac{Q_A Q_B}{Q_A + Q_B}\right)$$

$$E_b = (\sigma - 1)(E_d + Q_{AB}) + (1 - \sigma)(Q_A + Q_B) + \sigma\frac{Q_A Q_B}{Q_A + Q_B}$$

6) Surface disproportion, e.g. $A^* + B^* \leftrightarrow C^* + D^*$.

$$\Delta H = E_d + Q_C + Q_D - Q_A - Q_B$$

$$E_f = \sigma\left(E_d + Q_C + Q_D - Q_A - Q_B + \frac{Q_A Q_B}{Q_A + Q_B}\right)$$

$$E_b = (\sigma - 1)(E_d + Q_C + Q_D) + (1 - \sigma)(Q_A + Q_B) + \sigma\frac{Q_A Q_B}{Q_A + Q_B}$$

7) Homonuclear surface disproportion, e.g. $2C^* \leftrightarrow A^* + B^*$.

$$\Delta H = E_d + 2Q_C - Q_A - Q_B$$

$$E_f = \sigma\left(E_d + 2Q_C - Q_A - Q_B + \frac{Q_A Q_B}{Q_A + Q_B}\right)$$

$$E_b = (\sigma - 1)(E_d + 2Q_C) + (1 - \sigma)(Q_A + Q_B) + \sigma\frac{Q_A Q_B}{Q_A + Q_B}$$

8) Surface disproportionation to homonuclear product, e.g. $C^* + D^* \leftrightarrow 2A$.

$$\Delta H = E_d + Q_C + Q_D - 2Q_A$$

$$E_f = \sigma(E_d + Q_C + Q_D - 1.5Q_A)$$

$$E_b = (\sigma - 1)(E_d + Q_C + Q_D) + (2 - 1.5\sigma)(Q_A)$$

Appendix C

In this Appendix the kinetic schemes used for the numerical simulations described in the previous chapters are provided.

H_2 over Rh in UBI-QEP format

The UBI-QEP heterogeneous kinetic scheme of H_2 over rhodium catalyst from (Maestri, Vlachos et al. 2009) is provided in this section. This detailed microkinetic model is able to predict integral data of multiple processes. The parameters of the reaction mechanism been derived according to a multi-scale methodology: activation energies are predicted using the UBI-QEP theory, coverage effects are accounted for using Density Functional Theory(DFT), and pre-exponentials are calculated using transition state theory (TST).

In the input file reported the reactions are written in sequence, followed by the turn over frequency A (unitless and s^{-1}), the exponential beta (-), the bond index (-), the temperature dependence (-), the type of kinetic method (UBI) and the type of reaction. All these parameters are required in order to compute the reaction rates.

```
MATERIAL MAT-1
!*****************************************************************
SITE/RH_SURFACE/    SDEN/2.49E-9/
    Rh(s)   H2O(s)  H(s)    OH(s)   O(s)   OH(s) H2O(s)
END
!*****************************************************************
HEATS_OF_CHEMISORPTION / 300 /
    O(s)   /    1.5   /     100.0  /    O(s)  -26                    //
    H(s)   /    1.5   /     62.3   /    H(s)  -2.5                   //
    OH(s)/      2.0   /     70.0   /    O(s)  -33   /     H2O(s)  25  //
```

```
    H2O(s) /   2.5   /     10.8   /    OH(s) 25    /    H2O(s) -4.5 //
END
!*****************************************************************
REACTIONS
H2      +Rh(s)   +Rh(s)     =>H(s)    +H(s)     7.73E-01   0.9387  0.5
                                          UBI   2   ADS
H(s)    +H(s)   =>H2        +Rh(s)    +Rh(s)    5.56E+11  -0.4347  0.5
                                          UBI   2   DES
O2      +Rh(s)   +Rh(s)     =>O(s)      +O(s)    4.81E-02   1.9965  0.5
                                          UBI   2   ADS
O(s)    +O(s)   =>O2        +Rh(s)    +Rh(s)    4.31E12    1.1995  0.5
                                          UBI   2   DES
OH(s)   +Rh(s)  =>H(s)      +O(s)               5.2E12    -0.2659  0.3
                                          UBI   5   SUP
H(s)    +O(s)   =>OH(s)     +Rh(s)              4.69E12   -0.8196  0.3
                                          UBI   5   SUP
H2O(s)  +Rh(s)  =>H(s)      +OH(s)              5.74E11    0.0281  0.55
                                          UBI   5   SUP
H(s)    +OH(s)  =>H2O(s)    +Rh(s)              1.8E9      1.2972  0.55
                                          UBI   5   SUP
H2O(s)  +O(s)   =>OH(s)     +OH(s)              2.08E13   -2.113   0.3
                                          UBI   8   SUP
OH(s)   +OH(s)  =>H2O(s)    +O(s)               7.22E10   -0.2902  0.3
                                          UBI   8   SUP
OH      +Rh(s)  =>OH(s)                         2.66E-1   -0.2891  0.5
                                          UBI   1   ADS
OH(s)           =>OH        +Rh(s)              1.14E13   -0.95    0.5
                                          UBI   1   DES
H2O     +Rh(s)  =>H2O(s)                        7.72E-2    1.4067  0.5
                                          UBI   1   ADS
H2O(s)          =>H2O       +Rh(s)              2.06E13   -1.8613  0.5
                                          UBI   1   DES
H       +Rh(s)  =>H(s)                          1.93E-1    1.5313  0.5
                                          UBI   1   ADS
H(s)            =>H         +Rh(s)              2.4E12     1.3208  0.5
                                      UBI   1   DES
O       +Rh(s)  =>O(s)                          4.46E-2   -1.9236  0.5
```

```
                                       UBI   1   ADS
O(s)            =>O         +Rh(s)              9.74E12   -1.9701  0.5
                                          UBI   1   DES
```

Nomenclature

A – pre-exponential factor for Arrhenius reaction rate constant

A_{cat} – catalytic area [m^2]

A_{react}– geometric area of the reactor occupied by the catalyst [m^2]

$A_{face,l}$ – geometric area occupied by the catalyst on the generic face of the cell [m^2]

a–pre-exponential factor for sticky reactions, bulk fraction for the coverage reaction rate [-], coefficient of coverage-dependence [-]

a_{cat}– ratio between the real area of the catalyst and the reactor volume [m^{-1}]

b–temperature exponent for the computation of the sticky coefficient [-]

c –activation energy for the computation of the sticky coefficient [J mol^{-1}], concentration in the gas-phase [mol m^{-3}]

Co– Courant number [-]

c_p–specific heat of the gas mixture[J mol^{-1} K^{-1}]

$\mathbf{d}$– vector distance through the centroid of adjacent cells [m]

$\mathscr{D}$ – diffusivity [m^2 s^{-1}]

e – eccentricity [-]

E_{att} – activation energy [J mol^{-1}]

E_b–backward activation energies [J mol^{-1}]

E_d – dissociation energy [J mol^{-1}]

E_f – forward activation energies [J mol^{-1}]

E_{max} – Lennard-Jones activation barrier for adsorbed species [J mol^{-1}]

E_{min} - chemisorption energy minimum [J mol^{-1}]

f – face of the generic cell [-]

$\mathbf{g}$ – gravity acceleration [m s^{-1}]

H – enthalpy [J]

H_{tot} – total enthalpy [J]

k – kinetic constant, temperature dependence [-]

k_b – backward reaction constant

k_f–forward reaction constant

M– transport term

m_{tot}– total mass [kg]

m – reaction order [-], mass [kg]

MW–molecular weight [kg mol^{-1}]

n – index for the generic material [-], mole [mol]

N–point in the centre of the neighbouring control volume

NB –number of bulk species [-]

N_C – number of computational cells [-]

NCF– Number of Catalytic Faces of the cell [-]

NAS – Number of Adsorbed Species [-]

NR – number of reactions [-]

N_S- number of chemical species [-]

NS – number of surface species [-]

NU - number of unknowns [-]

P – pressure [N m^{-2}], centroid of the cell [-]

Q^{het}– net heat of production of the adsorbed species [J]

Q^{hom}– net heat of production of the gaseous species [J]

Q – heat of chemisorption [J mol^{-1}]

r – coordinate normal to the catalytic surface [m]

r_0 – outer radius [m]

r_i - inner radius [m]

R –constant of perfect gas [J mol^{-1} K^{-1}], molar production rate [mol s^{-1}]

R^{het} – heterogeneous reaction rate

R^{hom} – homogeneous reaction rate

R_{sur}– surface reaction rate

S– source term [-], surface [m^2]

S_f– surface vector

s – turnover frequency [s^{-1}]

T – temperature [K]

T_0 – reference temperature [K]

t– time [s]

$\boldsymbol{U}$– velocity vector [m s^{-1}]

$\boldsymbol{u}$– secondary variables vector

V – volume [m^3]

V_{cell}– volume of the cell [m^3]

V_{react}–total volume of the reactor [m^3]

$\boldsymbol{x}$ – position vector [m]

x_g – mole fraction of the gaseous species [-],

$\boldsymbol{x_p}$– coordinate of the centroid [m]

Greek letters

α_{cat}–ratio between geometric and effective catalytic area [-]

β –exponential coefficient of temperature in modified Arrhenius formula [-]

γ– sticking coefficient

Γ_{site} – catalyst site fraction [mol m^{-2}]

Γ– generic transport property

δt– time step [s]

δx– cell size [m]

ΔH – heat of reaction [J mol^{-1}]

Δx - distance between the centers of the circles [m]

ε– experimental parameter for the coverage dependence of the kinetic constant [-]

λ– thermal conductivity of the gas-phase [W m^{-1}K^{-1}]

η– experimental parameters for the coverage dependence of the kinetic constant [-]

μ– dynamic viscosity [kg s^{-1} m^{-1}], experimental parameter for the coverage dependence of the kinetic constant [-]

ν– stoichiometric coefficient [-]

ρ– density of the mixture [kg m^{-3}]

σ– number of sites occupied by the adsorbed species [-], bond index [-]

$\boldsymbol{\varphi}$– primary variables vector

ϕ – generic scalar field

Ψ– generic nonlinear function

ω– massive fraction [-]

ϑ_i– site fraction of the *i*th component [-]

Superscript

| | – vector magnitude

* – adsorbed species

~ – average property

$\hat{}$ – massive property

^{0} – initial value

^{gas} – gas-phase

Subscript

$_l$ – index of the generic species

$_j$ – index of the generic species

$_k$ – index of the generic face

$_l$ – index of the generic species

$_D$ – discretized form of the generic quantity

References

Aghalayam, P., Y. K. Park, et al. (2000). "Construction and optimization of complex surface-reaction mechanisms." Aiche Journal **46**(10): 2017-2029

Bird, R. B., W.E. Stewart and E.N. Lightfoot (2002). "Transport Phenomena. 2 ed." New York: J. Wiley.

Buzzi-Ferraris, G. (1998). "Metodi numerici e software in C++." Wiley Longmann Italia.

Buzzi-Ferraris, G. (2011). "BzzMath 6.0 from (www.chem.polimi.it/homes/gbuzzi)."

Deutschmann, O., C. Correa, et al. (2003). "Experimental and numerical study on teh transiebt behaviour of partial oxydation of methane in a catalytic monolith." Chemical Engineering Science **58**: 633-642.

Deutschmann, O., S. Tischer, et al. (2008). "DETCHEM™ Software Package, http://www.detchem.com." Karlsruhe 2.2 ed.

Deutschmann, O., S. Tischer, et al. (2011). "DETCHEM™ User Manual - Version 2.3.".

Dumesic, J. A., G. W. Huber, et al. (2008). "Microkinetics: Rates of Catalytic Reactions." Handbook of Heterogeneous Catalysis. Ertl, et al., Editors.

Faravelli, T., A. Cuoci, et al. (2008). "Kinetic modeling of soot formation in turbulent non premixed flames." Environmental Engineering Science **25**(10): 1407-1422.

Faravelli, T., A. Cuoci, et al. (2009). "Formation of soot and nitrogen oxides in unsteady counter flow diffusion flames." Combustion and Flame **156**(10): 2010-2022.

Faravelli, T., A. Cuoci, et al. "http://creckmodeling.chem.polimi.it/."

Ferziger, J. H. and M. Peric (1999). "computational Methods for Fluid Dynamics." 2nd Edition. Springer.

Fluent, I. (2004). "GAMBIT 2.2 - Tutorial Guide " www.fluent.com.

Gear, C. W. (1971). "Numerical Initial-Value Problems in Ordinary Differential Equations." Prentice-Hall, Englewood Cliffs, NJ.

Gokhale, A. A., S. Kandoi, et al. (2004). "Molecular-level descriptions of surface chemistry in kinetic models using density functional theory." Chemical Engineering Science **59**(22-23): 4679-4691.

Hartmann, M., L. Maier, et al. (2010). "Catalytic partial oxidation of iso-octane over rhodium catalysts: An experimental, modeling, and simulation study." Combustion and Flame **157**: 1771-1782.

Issa, R. I. (1986). "Solution of the implicitly discretized fluid flow equations by operator-splitting." J. Comp. Physics **62**: 40-65.

Jasak, H. (1996). "Error Analysis and Estimation for the Finite Volume Method with Applications to Fluid Flows." PhD Thesys; Imperial College; London.

Koop, J. and O. Deutschmann (2009). "Detailed surface reaction mechanism for Pt-catalyzed abatement of automotive exhaust gases." Applied Catalysis B: Environmental **91**: 47–58.

Maestri, M. (2011). "Microkinetic Analysis of complex chemical processes at surfaces." [in press] Wiley VCH

Maestri, M., A. Beretta, et al. (2008). "Two-dimensional detailed modeling of fuel-rich H2 combustion over Rh/Al2O3 catalyst." Chemical Engineering Science **63**: 2657-2669.

Maestri, M. and K. Reuter (2011). "Semiempirical Rate Constants for Complex Chemical Kinetics: First-Principles Assessment and Rational Refinement." Angewandte Chemie-International Edition **50**(5): 1194-1197.

Maestri, M., D. G. Vlachos, et al. (2009). "A C(1) Microkinetic Model for Methane Conversion to Syngas on Rh/Al(2)O(3)." Aiche Journal **55**(4): 993-1008.

Manca, D., G. Buzzi-Ferraris, et al. (2009). "The solution of very large non-linear algebraic systems." Computers and Chemical Engineering **33**: 1727-1734.

Mangani, L. (2008). "Development and Validation of an Object Oriented CFD Solver for Heat Transfer and Combustion Modeling in Turbomachinery Applications." PhD Thesis, University of Florence.

Mhadeshwar, A. B. and D. G. Vlachos (2005). "A thermodynamically consistent surface reaction mechanism for CO oxidation on Pt." Combustion and Flame **142**(3): 289-298.

Mladenov, N., J. Koop, S. Tischer and O. Deutschmann (2010). "Modeling of transport and chemistry in channel flows of automotive catalytic converters." Chemical Engineering Science **65**(2): 812-826.

OpenFOAM® (2011). "The Open Source CFD Toolboox - User Guide."

OpenFOAM® (2011). "www.openfoam.com - OpenFOAM®: open source CFD."

Oran, E. S. and J. P. Boris (2001). "Numerical simulation of reactive flow." Cambridge University Press.

Patankar, S. V. and D. B. Spalding (1972). "A calculation procedure for heat, mass and momentum transfer in three-dimensional parabolic flows." Int. J. Heat Mass Transfer **15**: 1787.

Pope, S. B. and R. Zhuyin (2008). "Second-order splitting schemes for a class of reactive systems." Journal of Computational Physics **227**(8165-8176).

Quarteroni, A. and A. Valli (1999). "Domain decomposition methods for partial differential equations (Numerical mathematics and scientific computation)." Oxford University Press.

ReactionsDesign (2008). "CHEMKIN-PRO® Software - Input Manual." http://www.cadfamily.com/download/CAE/Chemkin-Tutorial/Input.pdf.

Ren, Z. and S. B. Pope (2008). "Second-order splitting schemes for a class of reactive systems." Journal of Chemical Physics **227**: 8165.

Reuter, K. (2009). "First-Principles Kinetic Monte Carlo Simulations for Heterogeneous Catalysis: Concepts, Status and Frontiers." Wiley-VCH, Weinberg.

Schlögl, R. (2001). "Theory in heterogeneous catalysis - An experimentalist's view." Cattech **5**(3): 146-170.

Shah, R. K. and A. L. London (1978). "Laminar flow forced convection in ducts." Academic Press.

Shustorovich, E. a. H. S. (1998). "The UBI-QEP method: a practical theoretical approach to understanding chemistry on transition metal surfaces." Surface Science Reports **31**(1-3): 5-119.

Strang, G. (1968). "On the construction and comparison of difference schemes." SIAM Journal of Numerical Analysis **5**: 506.

Van Doormaal, J. P. and G. D. Raithby (1985). "An evaluation of the segregated approach for predicting incompressible fluid flows." National Heat Transfer Conference, Denver, Colorado.

Versteeg, H. K. and W. Malalalsekera (1995). "An introduction to Computational Fluid Dynamics." Longman Scientific & Technical.

Vlachos, D. G., S. Kaisare, et al. (2008). "Stability and performance of catalytic microreactors: simulations of propane catalytic combustion on Pt." Chemical Engineering Science **63**: 1098-1116.

Vlachos, D. G., M. Stamatakis, et al. (2011). "A review of multiscale modeling of metal-catalyzed reactions: Mechanism development for complexity and emergent behavior." Chemical Engineering Science **66**(19): 4319-4355.

Aghalayam, P., Y.K. Park and D.G. Vlachos. (2000). "Construction and optimization of complex surface-reaction mechanisms." Aiche Journal**46**(10): 2017-2029